KAUNAS UNIVERSITY OF TECHNOLOGY

KUMAR ANUBHAV TIWARI

DEVELOPMENT OF MEASUREMENT TECHNIQUES FOR THE DETECTION AND ESTIMATION OF DEFECTS IN COMPOSITE STRUCTURES BY USING ULTRASONIC GUIDED WAVES

Doctoral dissertation
Technological sciences, Measurement Engineering (T 010)

2019, Kaunas

The entire research work was accomplished during the period of 2014–2018 at Prof. Kazimieras Baršauskas Ultrasound Research Institute of Kaunas University of Technology. The research was granted by Research Council of Lithuania.

Scientific supervisor
Prof. Dr Renaldas Raišutis (Kaunas University of Technology, Technological Sciences, Measurement Engineering – T 010)

English Language Editor
Dovilė Blaudžiūnienė (Publishing House "Technologija")

The dissertation is available on the Internet:
http://ktu.edu

ISBN 978-609-02-1632-3

The bibliographic information about the publication is available in the National Bibliographic Data Bank (NBDB) of the Martynas Mažvydas National Library of Lithuania.

KAUNO TECHNOLOGIJOS UNIVERSITETAS

KUMAR ANUBHAV TIWARI

MATAVIMO METODŲ KOMPOZICINIŲ MEDŽIAGŲ STRUKTŪRŲ DEFEKTAMS APTIKTI IR ĮVERTINTI NUKREIPTOSIOMIS ULTRAGARSO BANGOMIS SUKŪRIMAS

Daktaro disertacija
Technologijos mokslai, matavimų inžinerija (T 010)

2019, Kaunas

Disertacija rengta 2014–2018 metais Kauno technologijos universiteto Prof. K. Baršausko ultragarso mokslo institute. Mokslinius tyrimus rėmė Lietuvos mokslo taryba.

Mokslinis vadovas:
Prof. dr. Renaldas RAIŠUTIS (Kauno technologijos universitetas, technologijos mokslai, matavimų inžinerija, T 010)

Redagavo: Dovilė Blaudžiūnienė (leidykla „Technologija“)

Interneto svetainės, kurioje skelbiama disertacija, adresas:
http://ktu.edu

ISBN (įrašyti gautą ISBN kodą)

Leidinio bibliografinė informacija pateikiama Lietuvos nacionalinės Martyno Mažvydo bibliotekos Nacionalinės bibliografijos duomenų banke (NBDB).

TABLE OF CONTENTS

ABBREVIATIONS

GFRP	Glass fiber reinforced plastic
CFRP	Carbon fiber reinforced plastic
SHM	Structural health monitoring
NDT	Non-destructive testing
GW	Guided wave
MFC	Macro-fiber composite
EMAT	Electromagnetic acoustic transducers
WTB	Wind turbine blade
WT	Wavelet transform
DWT	Discrete wavelet transform
HT	Hilbert transform
SSP	Split-spectrum processing
STFT	Short-time Fourier transform
EMD	Empirical mode decomposition
EEMD	Ensemble empirical mode decomposition
VMD	Variational mode decomposition
HHT	Hilbert Huang transform
LF	Low-frequency
HF	High frequency
LPF	Low-pass filter
HPF	High-pass filter
IMF	Intrinsic mode function
db	Daubechies
dB	Decibel
Al	Aluminum alloy
ADC	Analog to digital converter
SAFE	Semi-analytical finite element
2D-FFT	Two-dimensional fast Fourier transform

INTRODUCTION

Motivation and relevance of work

Structural integrity assessment is an evaluation of the integrity and conformity of a structure for its reliable performance operation over a set duration under varying loading conditions providing the fact that defects/damages or flaws are detected correctly. In most industrial and household applications, such as nuclear and green energy applications, renewable energy applications (wind and tidal power plants), pipelines and storage tanks, construction industry, structures in the ground, water and aerospace applications are constructed from composite materials. Composite materials are used rather intensively due to their lightweight, high compressive and tensile strengths, high stiffness and low density, flexibility, lower maintenance and non-corrosive nature (1). Generally, the composite materials are classified based on their matrix materials (2). Out of the various composite materials, the fiber-reinforced plastics (FRP) are widely used for providing the lower weight and height strength to the structures (3). The carbon fiber-reinforced plastic (CFRP) and glass fiber-reinforced plastic (GFRP) are the most common FRPs to manufacture the components of the structures operating under cyclic loads including aircraft wings and wind turbine blades (4, 5). In spite of all favorable features and a wide range of applications the composites contain, the failure in the components of composite structures may occur either *in-service* or during the manufacturing procedure (6, 7) which can be described as follows:

- Manufacturing defects: Bonding defects, flaws due to porosity, incorrect fiber volume due to extra/insufficient resins, misaligned fibers, cracks in ply and delamination.
- In-service defects: Cracks, fractures, buckling of fibers, delamination due to bond failures, failure at the interface between fiber and matrix or moisture damage.

In order to keep the infrastructures properly functioning and avoid their failures, regular maintenance and inspection are necessary. Researchers have already found that the cost involving maintenance and inspection of aircraft corresponds to 25% of its entire life-cycle cost (8, 9). Thus, structural health monitoring (SHM) systems are implemented on the composite structures to reduce the maintenance cost and prevent system failures (10). Previous works suggest that an optimal SHM system can effectively reduce the maintenance and inspection cost by 30% to 40 % (11, 12). The transducers/sensors in SHM systems are used for recording the data and extracting the features of defects/damages from the recorded signals (13). Many non-destructive testing (NDT) methods have been developed for the identification, location and estimation of defects in SHM of structures such as ultrasonic testing, radiographic testing, electromagnetic testing, etc.

Among all the available NDT techniques, ultrasonic guided wave (GW) testing has been the most promising due to its high sensitivity to the defects and wide

coverage region (14, 15). Moreover, GW testing is fast, can cover up the defective regions to reasonable distances and have the ability to detect defects under ground, water or a layer of insulation (16, 17, 18). In comparison to guided wave testing, bulk wave testing is tedious and time-consuming, requires high-level training, uses the point-by-point scanning method and needs a visible area and accessibility of the defective region (19, 20). Due to the high sensitivity of GWs to the variation in modulus of elasticity (E) of the material under testing and minimal amplitude damping of propagating wave modes, only a few measurements are required for the inspection of large infrastructures to detect internal and surface defects (20, 21, 22). Researchers have successfully utilized the GWs for inspecting defects/damages in metallic structures (23), concrete structures (24, 25), pipes (26, 27, 28) and composite structures (29, 30, 31, 32, 33, 34, 35).

The ultrasonic GW testing is an effective inspection technique for estimating the location (a distance of the edge of defect from the initial/first scanned point) and the size of defects/damages in various composite structures. However, high attenuation of guided wave modes may occur due to the multi-layered and non-homogeneous structures associated with the composites (36). The interaction of ultrasonic guided waves with the composite structures depends on many factors which include the excitation frequency, material properties, the geometry of the structure and the direction of propagating waves (37, 38, 39). The possible mechanisms that may occur during the interaction of ultrasonic GW with the layered structure of composites are reflection or refraction of wave modes, scattering and mode conversions. It increases the complexity in the received ultrasonic signals so that the extraction of defects-related information becomes very complicated which can be overcome by applying an appropriate signal processing technique.

The conventional C-scan process is practically not suitable for large-sized composite structures with complex geometries. If the transducers are able to be scanned over defects, the acquired B-scan or few A-scans are the fast and economical approaches in the GW testing for large structures. In this work, only a B-scan or A-scans are utilized for further processing in order to detect and estimate the defects in the composite structure and compare the GW characteristics in the defect-free and defective regions. However, the accuracy of estimation of size and location of defects depends on various factors such as GW properties, the type of transducers and material or excitation frequency, etc. Generally, a comparison of the reference and current states of the system has a major role in a successful SHM system (40, 41). In the case of contact transducers attached to the structure, the reference data in the damage-free region is calculated by estimating the initial time-signals between all possible combinations of transducer-pairs. The algebraic difference between the reference and current time signals provides information about the damage by eliminating the boundary reflections (42, 43). This technique has some serious limitations, such as complexities associated with the calibration and verification of SHM system and provides no information about the size, location and type of defects other than the little information about the presence of defects. Therefore, more efforts are required to develop effective measurement techniques including the adaptation of post-

processing of GW signals to increase the efficiency of an NDT and SHM system for real-time applications. The correct combination of experimental analysis and signal processing approaches to process the GW signals leads to obtaining significant results.

During the investigation of a sample, GW transducers can be utilized in different ways. The measurement set-up irrespective of other concerned parameters also depends on the size or length of the structure and in accordance, the combination of transducers can be selected. In this thesis, the segment of WTB constructed from GFRP has been considered as an object (see Chapter 2 and Chapter 4 for details). Most of the scientific research work and commercial testing of WTB based on contact ultrasound has been performed by utilizing the ultrasonic phased array methods and ultrasonic pulse-echo techniques (44, 45, 46, 47). The inspection time and complexity in the testing of WTB is associated with the layered structure, type of defects and the length of the blade. In comparison to the pulse-echo, the pitch-catch technique is more flexible in terms of transducer placement. Moreover, it reduces the complexity and cost associated with the phased-array technique due to the usage of a lesser number of devices. Additionally, the measurement techniques can be developed depending on the length of the structure by using a suitable configuration of transducers operating in the pitch-catch mode.

Keeping this motivation in mind, two different measurement techniques (*e.g.* for small and large structures) with less complexity and more flexibility can be developed by using only two contact-type transducers operating in a pitch-catch mode. Two transducers separated by a shorter distance (few wavelengths of propagating wave modes or few tens of millimeter) and operating in a pitch-catch mode could be used for testing the structure containing defects at shorter distances from the GW transmitter/receiver. Keeping the shorter distance between both transducers fixed also reduces the attenuation and dispersion losses due to the distance between transducers.

However, low-frequency (LF) GWs can travel long distances and this feature is very useful for NDT and SHM of larger structures. Therefore, in the second case, an ultrasonic GW transducer (transmitter) can be glued/embedded within a structure at a certain position and a distant receiver can be scanned over the defective regions at longer distances from the ultrasonic transmitter. However, this long-distance measurement set-up using ultrasonic GWs highly depends on the location, displacement characteristics and region and direction of coverage (directivity pattern) of the embedded/glued transmitting transducers. Therefore, in order to improve the accuracy of measurement, prior information of the displacement characteristics and directivity pattern of a transmitter is of as much importance as the investigation of defects with a fixed transmitter and a scanning receiver especially in the case of glued/embedded transmitter. In both GW measurement techniques (short-distance and long-distance), the appropriate signal-processing methods depending on the parametric characteristics of the receiver signal should be developed for the estimation of defect parameters (size and location) and GW characteristics (time of arrival, instantaneous amplitude/frequency characteristics, phase velocity of propagating wave modes, etc.).

Therefore, the detection and estimation of the presented defects or damages on the composite structures and the characteristics of GWs in defective regions can be performed in an effective manner by using the following procedures:

1. The contact-type measurement technique for short-distance (between transmitter and receiver) GW testing of the composite structure can be developed by using a pair of point-type contact ultrasonic transducers.
2. The contact-type measurement technique for longer distance (between transmitter and receiver) GW testing or for the inspection of large composite structures, can be developed by a thin and compact-sized embedded/glued transmitter and a scanning receiver/transducers. For a glued/embedded transmitter to be used for long-range GW testing, the characteristics of a transmitter such as directivity and three-dimensional (3D) displacements profile could be analyzed to assure the correct placement of the transducer and effective generation of GWs on the structure under investigation.
    - The three-dimensional (3D) characteristics of a transducer can provide the behavior of transducer *in-plane* (displacements along the direction of wave propagation and perpendicular direction of wave propagation) and *out-of-plane* directions. Moreover, the obtained characteristics can be compared with the manufacturer data-sheet in order to validate if the transducer itself is a defect-free before embedding/gluing it on the structure (48).
    - The directivity of the sensors/transducers can be calculated of the transducer to be embedded or glued for effective coverage of the damaged region of the structure under test. Moreover, prior knowledge of directivity patterns of the transducers facilitates in choice of an appropriate excitation frequency, the propagating wave modes of interest and the suitable configuration of transducers (49, 50).
3. The experimental unprocessed GW signals are not enough to locate, size or characterize internal defects. Appropriate signal processing techniques should be applied for the post-processing of received ultrasonic GW signals to improve the estimation and characterization of defects by analyzing the variations in signal parameters such as amplitude, time of flight, frequency, etc. in the defect-free and defective regions. The signal processing of ultrasonic GW signals enhances the reliability of the SHM system (15, 51, 52, 53, 54, 55).

It leads to the scientific hypothesis that the flexible and cost-effective pitch-catch technique can be utilized in an effective manner to develop contact-type measurement techniques for the inspection of smaller and larger multi-layered composite structures by ultrasonic guided waves. These techniques can be combined with the signal processing approaches for the estimation and characterization of defects by dealing with the complexity associated with the GWs (reflection, refraction, mode conversion and scattering of propagating wave modes) during its interaction with multi-layered composite structures.

Objective and tasks

The **primary objective of the thesis** is to propose two flexible and cost-effective contact-type measurement techniques in pitch-catch mode and based on short-distance and long-distance GWs for the detection and estimation of the disbond-type defects in smaller and larger multi-layered composite structures. The sub-objectives are the utilization of various signal-processing techniques to de-noise and process the experimental signals in order to improve the accuracy of defect estimation and analysis of instantaneous characteristics of GWs.

The following **tasks** were formulated in a sequential order to achieve the objective.

1. To review literature regarding GW generation, NDT of composites using ultrasonic GWs, contact and non-contact ultrasonic NDT methods, signal-processing techniques to process ultrasonic signals.
2. To investigate the composite structures for the identification of disbond-type defects by developing a measurement technique based on a pair of point-type contact GW transducers (if the receiver is at a short distance from the transmitter) and appropriate signal processing techniques to locate and size the defect, and analyze the GW characteristics in the defective regions.
3. To explore the feasibility of P1-type macro-fiber composite (MFC) transducer for long-range GW testing for defect estimation by investigating its 3D displacement characteristics.
4. To develop and validate a simplified two-dimensional (2D) analytical model to predict the directivity patterns of contact-type GW transducers which can be glued on/embedded into the surface of the structure (*e.g.*, an MFC transducer).
5. To investigate the composite structures for the identification of disbond-type defects by gluing a P1-MFC transducer (transmitter) and a point-type contact ultrasonic receiver (if the receiver is far away from the transmitter) with the application of appropriate signal processing techniques to locate and size the defects, and analyze the GW characteristics.

Scientific novelty of the work

1. Two cost-effective contact-type measurement techniques with more flexibility and less complexity for the inspection of smaller and larger composite structures using GWs are proposed based on the pitch-catch operation.
    - The utilization of two point-type transducers fixed on a moving panel in the case of short-distance GW testing reduces the attenuation and dispersion losses due to the change in distance between the transmitter and receiver. Moreover, the usage of point-type transducers operating in thickness mode (*i.e.* high sensitivity to *out-of-plane* radiations or amplitude variations) leads to apply the

simple amplitude detection techniques for the identification of defects in linear scanning. It is also proposed that reducing the fixed distance between the two transducers could increase the accuracy of defect estimation which in turn provides the motivation to develop a new configuration of pair of transducers to locate and size the smaller defects.

- It is proposed that the frequency-dependent glued (MFC) transducer and a contact-type transducer can be used to inspect larger structures. The P1-type MFC transducer has a dominant d33 or elongation mode. However, the high directivity of *out-of-plane* radiations of the MFC transducer at resonant frequency facilitates to create a simple configuration of MFC and contact-type transducer to acquire the dominant A_0 mode for the analysis of defects on the structure.

2. It is proposed that 3D spatial characteristics of unloaded and vibrating MFC transducer can ensure that the transducer itself is defect-free to be used in the ultrasonic NDT of structures. It is also demonstrated that accurate 3D characteristics can ensure the suitability of typical GW modes to be used in SHM and NDT applications.
3. A novel 2D analytical model is proposed which could predict the directivity or coverage region of any contact-type transducer for different propagating wave modes at any frequency and propagating medium. Knowing the location for of transducers placement could increase the accuracy of the measurement process. Moreover, it takes a significantly shorter time to estimate the directivity as compared to the numerical modelling and experimental process.
4. In order to select the appropriate mother wavelet in DWT, the correlation of original signal to the detailed signal at the highest level is proposed. Instead of correlating the original signal from the transformed and de-noised signal, considering only detailed signal at the highest level (contains most of the signal information) reduces a considerable amount of computation time in processing.
5. In order to estimate the instantaneous characteristics of a signal by Hilbert transform the signal must be mono-component or close to the mono-component. That is why we use the mode decomposition technique. However, in multi-layered structures, the reflected signals from opposite edges produce complexity in the mode decomposition process. It is proposed to apply 2D-FFT in order to remove the reflected signals which in turn could facilitate the mode decomposition technique in achieving mono-component signals.

Practical importance of the work

1. The 3D characteristics of any GW transducer can provide the conformity that a transducer is free from any manufacturing or in-service defects before its application in the field of ultrasonic NDT and SHM. Therefore, it can significantly contribute to the development of a reliable SHM system.
2. The fast-processing 2D analytical model can be used to predict the directivity patterns of contact-type ultrasonic transducers at any distance and excitation frequency by knowing the behavior of the transducer and the dispersive characteristics of the propagating medium. Moreover, the correct position, the number of transducers, specific transducer and wave modes for the inspection of a particular type of defects using ultrasonic NDT can be selected if the directivity pattern of a transducer is known.
3. The proposed measurement techniques and signal processing approaches could play a vital role in detecting and locating defects and estimating the GW characteristics, especially in structures with a complex geometry where only one-side access is possible.

Presented results for the defense of the dissertation

1. The estimated three-dimensional characteristics of unloaded and vibrating macro-fiber composite (MFC) transducer and its applicability in order to predict the spatial displacements of GW modes.
2. The developed 2D analytical model based on Huygens's principle and validated by finite element (FE) analysis and experimental investigation, which can calculate directivity patterns of contact-type GW transducers in any propagation medium with known dispersive characteristics.
3. The development of measurement techniques based on short-distance and long-distance GWs for the detection and estimation of the dis-bond type defects located on small and large multi-layered composite structures.
4. Novel signal processing techniques applied on experimental signals for the extraction of defect features (size and location) and GW characteristics in the defect-free and defective region.

Approbation

The critical evaluation of the research work was presented during the period of dissertation by the scientific community have been certified by 11 publications: 7 articles are published in international journals referred in Thomson Reuters ISI Web of Science (with impact factor), while other 4 publications are published in the reviewed proceedings of international conferences indexed in Thomson Reuters ISI Web of Science (without impact factor). The results were also presented in 7 scientific conferences held in Vilnius, Prague, Funchal, and Belgrade. The doctoral scholarship was provided by the Research Council of Lithuania for the entire duration (2014–2018) of study. In 2016, a part of the research was granted a research scholarship by

the INFOBALT Company. In 2017, a one-time scholarship provided by the Kaunas University of Technology, Lithuania for the most active Ph.D. student was received. In 2018, the academic-achievement scholarship provided by the research council of Lithuania was received. In 2018, the European Structural Integrity Society (ESIS) support for researchers was received.

Organization of the dissertation

The dissertation consists of an introduction, 5 chapters, overall conclusions of the presented work, a list of references and scientific publications of the author. The organization of the dissertation is as follows:

1. In **Chapter 1**, the literature review of ultrasonic non-destructive testing methods is presented, which reveals the basic features and limitations associated with ultrasonic guided waves, the applicability of ultrasonic guided waves in various composite structures, contact and non-contact ultrasonic testing methods and presentation of ultrasonic data, the overview of the significance of directivity and 3D displacement characteristics of the transducer and various signal processing techniques for the post-processing of ultrasonic GW signals are presented.
2. In **Chapter 2**, the measurement technique using contact-type transducers with appropriate signal processing techniques in the case of short-distance GW testing for the detection and estimation of the different-sized dis-bond type defects located on the composite sample possessing the aerodynamic profile has been presented. The characteristics of GWs in the defective regions are also analyzed in comparison to the defect-free region.
3. In **Chapter 3**, the 3D spatial displacements and directivity characteristics of an MFC transducer and its impact on SHM and long-distance GW testing have been presented. It is also discussed how the 3D displacements and accurate directivity pattern of a transducer can contribute to increasing the reliability of the SHM system by knowing the directions/plane along which the ultrasonic guide waves would be generated most effectively. A novel 2D analytical model is also developed for the prediction of directivity patterns of contact type ultrasonic transducers in the generation of GWs.
4. In **Chapter 4**, the measurement technique of gluing an MFC transducer and contact-type receiver along with appropriate signal processing techniques in the case of long-distance GW testing to extract the information of disbond-type defects in the same sample as of Chapter 3 has been presented. This technique is more useful for structural health monitoring as a transmitter is permanently fixed/glued on the structure.
5. In **Chapter 5**, the overall uncertainty of the proposed measurement techniques has been calculated.

1. ULTRASONIC NON-DESTRUCTIVE TESTING OF COMPOSITES USING GUIDED WAVES

1.1 Fundamentals of guided waves and scanning methods

Sound waves which propagate beyond the range of human hearing capability (above 20 kHz) are called ultrasound (56). In general, sound waves are a form of mechanical vibrations which can propagate through different mediums *i.e.* liquids, solids, or gases. The frequency of such vibrations can be expressed as (57):

$$f = \frac{c}{\lambda} \tag{1.1}$$

where f is the frequency, λ is the wavelength of a wave and c is the velocity of the wave in the medium.

As the wave passes through the boundary of the interface between two materials, a part of acoustic energy may be transmitted, reflected, or refracted and it can be characterized by acoustic impedance (10, 57)

$$Z = \rho \cdot c \tag{1.2}$$

where Z is the acoustic impedance and ρ is the density of the material.

The ultrasonic waves are categorized into two types: ultrasonic bulk waves and ultrasonic guided waves. In general, bulk waves travel away from the boundary of the testing structure. However, there may be the involvement of some boundary interactions mechanism such as reflection, refraction and diffraction. In contrast, ultrasonic guided waves propagate in the structure guided by its boundaries providing that the thickness of the structure is lesser than the operating wavelength (λ_o). Typical GW results from the interference of longitudinal and shear waves (58). There may be an infinite number of guided wave modes due to the involvement of boundary conditions. Many types of guided waves such as Lamb waves, Rayleigh waves, and Stonely waves are available (59). Although different guided wave modes typically cause dispersion, mode conversion or other complexities and therefore limit their usage in SHM of structures. But at the same time, the diversity and sensitivities associated with different modes can contribute to other options for different SHM applications. Guide Lamb waves discovered by Horace Lamb are fast and more sensitive to the internal and surface defects, have the ability to travel a long distance as compared to other available GW testing techniques for the plate-type structures (60, 61, 62) and composite structures (63). Therefore, in this dissertation objects (Al plate, GFRP etc.) are investigated by the fundamental guided Lamb waves. Hence, in the context of the dissertation, ultrasonic GWs or simply GWs can be referred as guided Lamb waves.

The three most common techniques used for scanning in the process of ultrasonic GW testing are: Pitch-catch (64, 65, 66, 67, 68), pulse-echo (69, 70, 71) and phased-array method (72, 73, 74). The pulse-echo technique requires a single transducer to be used as a transmitter and a receiver. The echoes are reflected back

after interaction with the boundaries of the structure and based on the parameters (arrival time, amplitude etc.), the defects and damages are estimated. The pitch-catch technique uses two transducers for operating as a transmitter and a receiver. In the phased-array technique, many transducers forming an array are placed with fixed patterns. The high resolution and focused ultrasonic beam can be generated by managing the relative phase of transducers. In comparison to conventional ultrasonic inspection techniques, the phased-array method has an upper hand in terms of speed, high resolution, electronic steering and flexibility in data processing. However, it requires additional electronic devices which in turn increase the overall cost and complexity of the system (75). Hence pitch-catch technique is the most suitable for the SHM of composite structures and for the inspection of structures with one-side access. Moreover, the pitch-catch technique is flexible in nature as the location of the transmitter and receiver on the surface can be altered as per requirement. That is why ultrasonic GW testing is the most effective scanning technique to investigate defects located too far from the transmitter in the large composite structures. In this case, a transmitter (e.g. MFC transducer) can be glued/fixed at one location and a distant receiver is scanned away to cover the region of interest. In this dissertation, pitch-catch scanning is utilized in all experiments.

1.2 Guided waves in plate-type structures

The generalized Navier equation of motion (59, 76) is used to formulate guided Lamb waves in homogeneous and isotropic plate-type structures and given as

$$\mu . u_{i,jj} + (\mu + \lambda) \cdot u_{i,jj} + \rho \cdot f_i = \rho \cdot \ddot{u}_i , (i, j = 1,2,3,4 \dots \dots) \tag{1.3}$$

where u_i is displacement and f_i is the body force in x_i direction; ρ is density; λ is the Lame constant $[\lambda = (2\mu \cdot \upsilon)/(1 - 2\upsilon)]$, where υ is the Poisson's ratio and μ is the shear modulus)

Eq. 1.1 is decomposed into two equations characterizing the longitudinal and shear waves independently (12, 16, 59) by applying the Helmholtz decomposition method:

$$\frac{\partial^2 \varphi}{\partial {x_1}^2} + \frac{\partial^2 \varphi}{\partial {x_3}^2} = \frac{1}{{c_L}^2} \cdot \frac{\partial^2 \varphi}{\partial t^2} \tag{1.4}$$

$$\frac{\partial^2 \psi}{\partial {x_1}^2} + \frac{\partial^2 \psi}{\partial {x_3}^2} = \frac{1}{{c_T}^2} \cdot \frac{\partial^2 \psi}{\partial t^2} \tag{1.5}$$

where Φ and Ψ are expressed as:

$$\varphi = \varphi(x_3) \cdot \exp[i(kx_1 - \omega t)] = [A_1 \sin(px_3) + A_2 \cos(px_3)] \cdot \exp[i(kx_1 - \omega t)] \tag{1.6}$$

$$\psi = \psi(x_3) \cdot \exp[i(kx_1 - \omega t)] = [B_1 \sin(px_3) + B_2 \cos(px_3)] \cdot \exp[i(kx_1 - \omega t)] \quad (1.7)$$

and p, q and k can be given by eq. 1.8:

$$p^2 = \frac{\omega^2}{{c_L}^2} - k^2; q^2 = \frac{\omega^2}{{c_T}^2} - k^2; k = \frac{2\pi}{\lambda_\omega} \quad (1.8)$$

where k is the wavenumber; ω is the circular frequency; constants A_1, A_2, B_1, B_2 characterize the boundary conditions; c_L and c_T denotes the velocities of longitudinal and shear waves, respectively (where $c_L = \sqrt{\frac{2\mu(1-\upsilon)}{\rho(1-2\upsilon)}}; c_L = \sqrt{\frac{\mu}{\rho}}$; x_1 and x_3 are the coordinates along the length and width of the plate, respectively.

It should be noted that x_1 also signifies the direction of wave propagation. After omitting the exponential term from the eq. 1.9 and eq. 1.10, the displacements (u) and stress (σ) can be calculated (16, 59). Thereafter, the solution can be expressed separately as two sets of equations for the symmetric (eq. 1.9) and asymmetric mode (eq. 1.10), respectively (59, 77).

$$\begin{gathered} \varphi = A_2 \cos(px_3), \psi = B_1 \sin(qx_3), \\ u_1 = ikA_2 \cos(px_3) + qB_1 \cos(qx_3), u_2 = 0, \\ u_3 = -pA_2 \sin(px_3) + ikB_1 \sin(qx_3), \\ \sigma_{31} = \mu[-2ikpA_2 \sin(px_3) + (k^2 - q^2) \cdot B_1 \sin(qx_3)], \\ \sigma_{33} = -\lambda(k^2 + q^2)A_2 \cos(px_3) - 2\,\mu[p^2 A_2 \cos(px_3) + ikqB_1 \cos(qx_3)] \end{gathered} \quad (1.9)$$

$$\begin{gathered} \varphi = A_1 \sin(px_3), \psi = B_2 \cos(qx_3), \\ u_1 = ikA_1 \sin(px_3) + qB_2 \sin(qx_3), u_2 = 0, \\ u_3 = -pA_1 \cos(px_3) + ikB_2 \cos(qx_3), \\ \sigma_{31} = \mu[-2ikpA_1 \cos(px_3) + (k^2 - q^2) \cdot B_2 \cos(qx_3)], \\ \sigma_{33} = -\lambda(k^2 + q^2)A_1 \sin(px_3) - 2\,\mu[p^2 A_1 \sin(px_3) + ikqB_2 \sin(qx_3)] \end{gathered} \quad (1.10)$$

where, u_1 and u_3 signify the movement in x_1 direction (along with the direction of wave propagation) and x_3 direction (across the plate thickness), respectively.

If h is half-thickness of the plate, the boundary conditions at the surface for finite-domain GW propagation can be applied as (12, 16):

$$\sigma_{31} = \sigma_{33} = 0 \; for \; x_3 = \pm h = \pm\frac{d}{2} \quad (1.11)$$

The Lamb waves propagating through an isotropic medium, therefore, can be characterized as (59, 78, 79):

$$\frac{(k^2 - q) \cdot \sin(qh)}{2ikp \cdot \sin(ph)} = \frac{-2\mu ikp \cdot \cos(qh)}{[\lambda k^2 + \lambda p^2 + 2\mu p^2] \cdot \cos(ph)} \quad (1.12)$$

After considering the p, q, λ, c_L and c_T, the symmetric and asymmetric modes can be described by the Rayleigh-Lamb wave eq. (1.13) and eq. (1.14), respectively (59, 78, 79):

$$\frac{\tan(qh)}{\tan(ph)} = \frac{4k^2qp}{[q^2-k^2]^2} \tag{1.13}$$

$$\frac{\tan(qh)}{\tan(ph)} = \frac{[q^2-k^2]^2}{4k^2qp} \tag{1.14}$$

The phase velocity (v_{ph}) of the GW modes can be calculated for a specific frequency-thickness product ($f \cdot d$) by using the eq. 1.13 and eq. 1.14. The group velocity (v_{gr}) can be calculated from phase velocity and specific frequency-thickness product (59, 75):

$$v_{gr} = {c_p}^2 \left[c_p - fd\left(\frac{dc_p}{d \cdot fd}\right)\right]^{-1} \tag{1.15}$$

There may be an infinite number of Lamb wave modes that can be propagated in the object but the most common guided Lamb modes are symmetric (S_n), asymmetric (A_n) and shear horizontal (SH_n) modes, where n (n = 0,1,2……∞) is the order of a specific mode (76, 80). The S_n and A_n modes possess in-plane as well as out-of-plane displacements. In-plane displacements are dominant in the S_n mode whereas A_n mode possesses more dominant out-of-plane displacements.

The SH_n modes possess the particle displacements normal to the direction of propagating wave and can be symmetrical or asymmetrical which are also called as shear-horizontal and shear-vertical respectively. The SH_n mode can be expressed by the following equation after considering ($u_1 = u_3 = 0$) (59):

$$\frac{\partial^2 u_2}{\partial {x_1}^2} + \frac{\partial^2 u_2}{\partial {x_3}^2} = \frac{1}{{c_T}^2} \cdot \frac{\partial^2 u}{\partial t^2} \tag{1.16}$$

The solution to eq. (1.16) can be achieved by applying suitable boundary conditions $\left(x_3 = 0, \frac{\partial u_2}{\partial x_3} = 0\right)$ and can be expressed as (59):

$$u_2(x_1, x_3, t) = A \cdot e^{-bx_3} \cdot \exp[i(kx_1 - \omega t)] \tag{1.17}$$

where b is equal to $k\left[1 - \left(\frac{w}{k \cdot c_T}\right)^2\right]$ and A is the constant.

Dispersion is one of the most important mechanisms in the field of ultrasonic NDT using GWs which describes the variation of group velocity and phase velocity with respect to the frequency (f) of excitation and thickness (d) of material (81). Dispersion can be expressed by phase velocity dispersion curves and group velocity dispersion curves. The dispersion curve represents variation in phase velocity or group

velocity of propagating GWs with respect to the *f.d* product. Theoretical dispersion curves for 2 mm thick aluminum alloy plate with parameters (Young's modulus (E) equals 71 GPa, density (ρ) equals to 2780 kg/m^3 and Poisson's ratio (υ) equals to 0.33) are calculated with the "Disperse" computational package (82) and shown in Fig. 1.1. In LF ultrasonic (frequency less than 1 MHz) only the fundamental GW modes (the S_0, A_0 and SH_0) are dominant. The velocities of waves at higher frequencies are different as compared to the lower frequencies. Thus, a dispersive wave can be further decomposed into different parts. Each part of the dispersive wave travels with different velocity in comparison to the dispersive wave. The movement of individual crests of the GW is characterized by phase velocity and the progression of wave energy or the movement of GW packets is characterized by group velocity (83, 84).

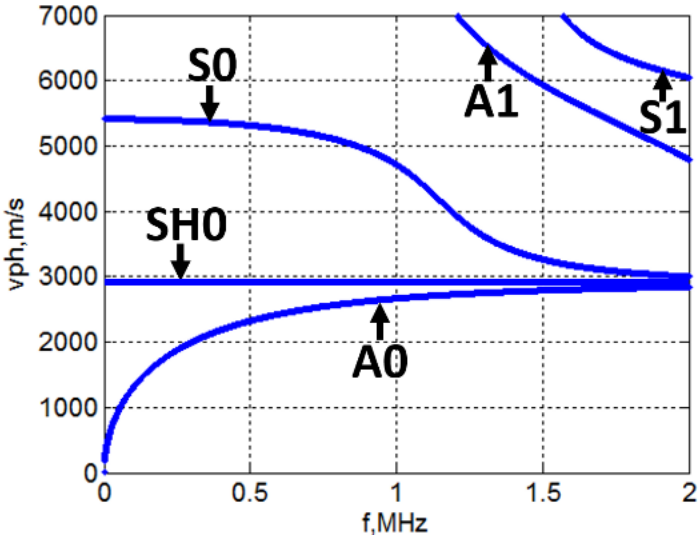

(a)

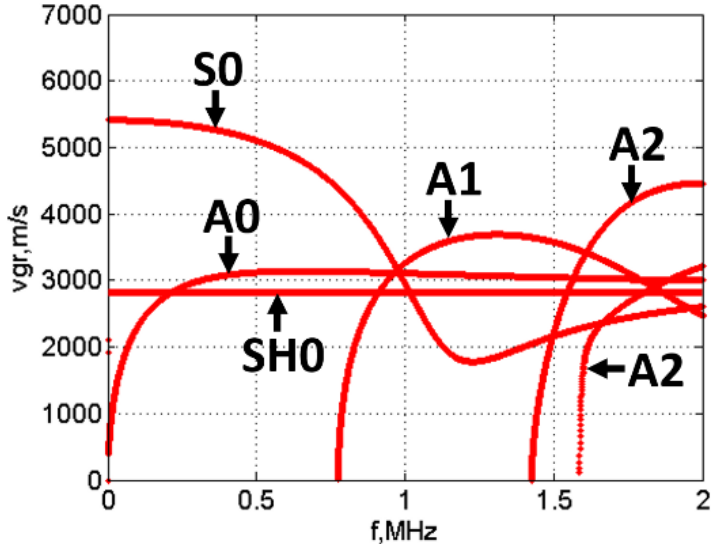

(b)

Fig. 1.1. Phase velocity (a) and group velocity (b) dispersive characteristics of 2 mm aluminum plate generated by *Disperse* (75)

1.3 Guided lamb waves in composite materials

When GW propagate in a layered or composite material, the interaction of waves with defects or the boundary of materials may lead to forming reflection, scattering, refraction or mode conversion of GWs. Due to the differences between acoustic impedances of different layers of composites, a part of direct waves is

reflected. Refraction occurs at oblique incidence and the rest of wave energy is reflected. In this process, mode conversion also occurs. The porosity of the material and curved shape of the defects causes wave scattering which results in the leakage or loss of energy. Therefore, the complexity associated with these mechanisms and the layered structure of composites itself creates more problems in the estimation of defects and damages (85, 86). In this thesis, all analysis and NDT of composite material has been performed by using guided Lamb waves. Hence, the focus is on the characteristics of Lamb waves in multi-layered composite (*e.g.* GFRP) materials.

The relation between stress and strain for an anisotropic material is given as (87):

$$\begin{bmatrix}\sigma_{11}\\ \sigma_{22}\\ \sigma_{33}\\ \sigma_{23}\\ \sigma_{13}\\ \sigma_{12}\end{bmatrix} = \begin{bmatrix}C_{11} & C_{12} & C_{13} & 0 & 0 & 0\\ C_{12} & C_{22} & C_{23} & 0 & 0 & 0\\ C_{13} & C_{23} & C_{33} & 0 & 0 & 0\\ 0 & 0 & 0 & C_{44} & 0 & 0\\ 0 & 0 & 0 & 0 & C_{55} & 0\\ 0 & 0 & 0 & 0 & 0 & C_{66}\end{bmatrix} \begin{bmatrix}\varepsilon_{11}\\ \varepsilon_{22}\\ \varepsilon_{33}\\ 2\varepsilon_{23}\\ 2\varepsilon_{13}\\ 2\varepsilon_{12}\end{bmatrix} \tag{1.18}$$

where, C is the stiffness matrix, ε is strain tensor and σ is stress.

The symmetric mode and antisymmetric mode dispersion equations can be given by eq. (1.19) and eq. (1.20), respectively (87):

$$(C_{33}R_{-}k_{z-} + C_{13}k_x)\cdot(R_{+}k_x + k_{z+}).\sin(k_{z+}h)\cos(k_{z-}h) - (C_{33}R_{+}k_{z+} + C_{13}k_x)\cdot(R_{-}k_x + k_{z-}).\sin(k_{z-}h)\cos(k_{z+}h) \tag{1.19}$$

$$(C_{33}R_{+}k_{z+} + C_{13}k_x)\cdot(R_{-}k_{zx} + k_{z-}).\sin(k_{z+}h)\cos(k_{z-}h) - (C_{33}R_{-}k_{z-} + C_{13}k_x)\cdot(R_{+}k_x + k_{z+}).\sin(k_{z-}h)\cos(k_{z+}h) \tag{1.20}$$

where $R_{\pm}$ is equal to $\frac{(\rho\omega^2 - C_{11}k_x{}^2 - C_{55}k_{z\pm})^2}{(C_{55}+C_{13})k_x k_{z\pm}}$, ($R_{-}$ and R_{+} corresponds to k_{z-} and k_{z+}); k_x and k_z are the wavenumbers in the direction of wave propagation (x) and along direction of plate thickness (z).

It should be noted that the resulting stiffness matrix can be calculated as the average of matrixes of particular layers if thicknesses of the layers are equal. The example of the layered structure of composite is shown in Fig. 1.2.

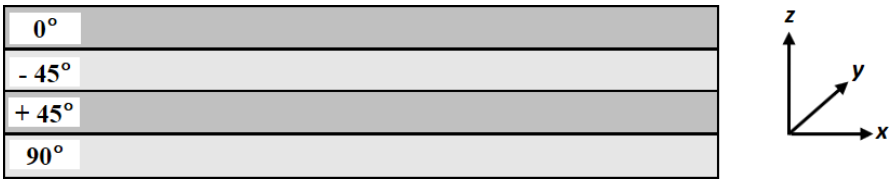

Fig. 1.2. Example of a layered composite sample: 0°/+45°/-45°/90°

1.4 Contact and non-contact ultrasonic testing

The ultrasonic inspection technique can be categorized as a contact-type and non-contact-type (7). The non-contact ultrasonic techniques are widely used to inspect large structures without having any physical contact or coupling between the transducer and surface of an object. These methods can be used in different environments, for the inspection of different materials, at variable temperatures and for structures which are not accessible easily from the test-site. The non-contact GW inspection techniques, such as air-coupled method, laser ultrasonic, electromagnetic acoustic transducers (EMATs) are widely used for testing composite structures using guided Lamb waves (88).

A comparative analysis of such non-contact methods is presented in Tab. 1.1 (7). Although these techniques are able to inspect large structures in a shorter time, each of them has certain limitations.

- In both the generation and reception of ultrasonic waves, laser ultrasonic can be significantly used (89, 90). However, low receiver sensitivity is one of the major limitations of this technique. Moreover, the reliability of this technique depends on stable positioning of the laser. Hence, this method is still a laboratory-based method.
- Electromagnetic methods (EMAT) is more applicable on sites but they have the limitations of lift-off distance (91). Hence the probe of EMT transducer should be closer to the test surface. These methods are applicable only to conducting materials.
- One of the most promising and widely used non-contact ultrasonic techniques for the inspection of a larger region of composite structures is the air-coupled method (92, 93, 94). The key limitations in this technique include impedance mismatch between air and test materials, limited frequency and attenuation of ultrasound in the air. They are better receivers of ultrasound than transmitters.

Table 1.1 A comparative analysis of non-contact ultrasonic methods (7)

Method	Principle	Merits	Demerits
EMAT	Electromagnetic principle	Automatic inspection	Problem of lift-off distance, poor transmitters, only for conducting materials
Air-Coupled Generation and Detection	Acoustic impedance of the two materials	Widely used, good for long-distance inspection	Problem of acoustic impedance mismatch, high attenuation of ultrasound, etc.
Laser Generation/ Interferometric Detection	Principle of radiation pressure/Ablation/Thermo-elasticity	Good at high temperature and remote environment	Laser needs to be in a stable position, almost a laboratory method, low sensitivity of laser interferometer receiver
Laser generation and EMAT detection	LASER as a Transmitter and EMAT as a receiver	Economical and moderate SNR	Bad for remote applications, EMAT lift-off distance problem
Hybrid Laser Generation and Air-coupled detection	Both Laser and Air-coupled mechanism. Utilize broadband LASER sources and narrowband air-coupled receivers	Best for testing of composites in a remote area, can generate ultrasonic waves from tens of kHz up to MHz	Low SNR (spatial modulation technique or constrained source can be used)

There are some hybrid non-contact techniques which combine the strength of two techniques. Oursler and Wagner (95) developed a hybrid system by combining the laser and EMAT systems. The hybrid laser generation/EMAT detection system, utilized the performance of laser for the highly efficient generation of angled shear waves and the tuned EMAT transducer for the detection of ultrasound (96). This system yielded the good SNR of received signals and it is much cheaper than the full-laser system. However, the problem of lift-off distance associated with the EMAT makes it impractical for the inspection at remote locations.

Hutchins et. al. (97) proposed the hybrid system based on laser generation/air-coupled piezoelectric detection. The system was successfully verified in the case of generating and receiving the plate waves or surface waves in metallic and composite structures (98, 99). The basic principle of this system is based on wideband sources and air-coupled receivers. The limitation of this system is poor bandwidth matching between the source and receiver which results in poor SNR.

In comparison to the non-contact ultrasonic, contact-type ultrasonic transducers utilize a direct contact or coupling medium with the object for the transmission and reception of ultrasonic waves. The key limitation with contact

ultrasonic systems are their lower scanning speed and inability to cover a larger region of the object as compared to non-contact techniques. However, the uncomplicated handling of transducers and the high acoustic impedance between the transmitter and receiver makes them popular for ultrasonic NDT of structures. They can be easily designed and configured as per specific requirement. Therefore, they are still applicable for the inspection of delamination, flaws, disbonds, etc. in various structures and thickness gauging (53, 100, 101, 102). That is why measurement techniques based on contact-type ultrasonic transducers are used in this dissertation.

The MFC transducers (103) can also be considered as contact-type because they can be glued/embedded with the structures under inspection. After its invention by NASA in 1996, MFCs have been widely used for the inspection of various kind of defects in the structure. The key advantages they have include small size, lightweight and high flexibility. They can be operated in d33 or elongation mode or in d31 or contraction mode (103). MFCs can effectively generate and receive guided Lamb waves (50, 104, 105).

1.5 Ultrasonic data visualization and the displacement and directivity characteristics of the GW transducer

Modern ultrasonic scanning systems can display the results in three common formats: as an A-scan (single point scanning), a B-scan (one-dimensional scanning) or a C-scan (two-dimensional scanning) (106, 107). The variations in ultrasonic energy or amplitude with time can be displayed by the A-scan. The B-scan is a series of A-scans along the scanned distance. In the B-scan presentation, the arrival times of all A-scans with respect to the scanned distance are presented. C-scans is the two-dimensional scanning which shows the top view of the object. It is also called a series of B-scans (108). It should be noted that a C-scan can display high-resolution images of the structure. Hence it facilitates the efficient detection, sizing and characterization of defects using ultrasonic GWs. Moreover, it requires less signal processing of the experimental signals. However, large structures are limited to only one-side access, B-scan or series of A-scans are more efficient using ultrasonic NDT with a pitch-catch configuration. Achieving C-scans in large and complex geometrical structures can be very expensive and time-consuming (109). In this thesis, only a single B-scan or a few A-scans acquired by contact-type ultrasonic methods are used for the analysis and estimation of defects in GFRP material. However, there are several limitations associated with the analysis of defects using a single B-scan. Firstly, the receiving transducer must scan the defective region before further processing. Secondly, appropriate signal processing techniques are required for effective estimation of the size and location of defects.

All transducers have a specific directivity pattern in the propagating medium. The beam width of any transducer depends on its diameter and wavelength. In comparison to the smaller transducers, the larger sized transducers radiate a relatively narrower beam pattern (49, 50, 110). The main lobe of the transducer contains most

of the energy. However, the side lobes, besides having inappropriate radiations, may contain some useful information.

In order to understand the effect of directivity pattern on the accuracy of defect estimation, a contact-type transducer glued on the surface of an object under investigation is presented in Fig. 1.3 (50).

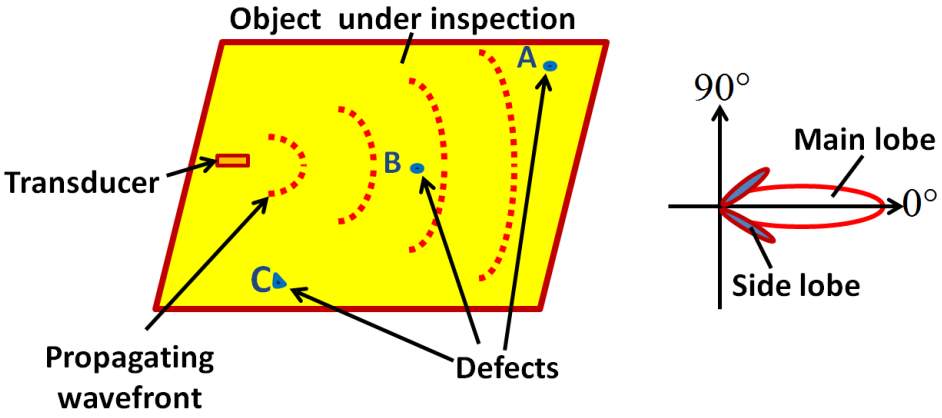

Fig. 1.3. The directivity pattern of a contact-type directional transducer glued on the structure under investigation (50).

The variations (main lobe and side lobes) in the directivity pattern with respect to the polar angle are also displayed. It clearly shows the main lobe containing maximum radiations and the minor lobes containing the lower undesired radiations. Figure 1.3 shows that defect-B has been accurately investigated whereas, the defect-A and defect-C are not in the range of transducer's directivity (coverage region). Hence, defect-A and defect-C cannot be investigated from the position of the transducer. The defect-A and defect-C could be tested if they were placed in the range of transducer's directivity either by changing the location or excitation frequency of the transducer (50). The key advantages in the field of NDT and SHM of structures by knowing the directivity patterns of transducers are as follows (49, 50):

- An accurate value of excitation frequency can be decided.
- The configuration of transducers can be designed for the inspection of large structures.
- Specific wave modes, such as S_0, A_0 or SH_0 can be selected depending on the applications.
- Overall, it contributes to the cost reduction of the SHM system.

There are many techniques developed by scientists for the analysis of directivity patterns (111, 112, 113, 114, 115). All of these methods are either experiment-based or based on finite element (FE) modelling which are time-consuming. Moreover, they

are limited to specific transducers and a propagating medium. Hence, versatile analytical modelling is required to predict the directivity patterns of transducers with any shape, attached to any propagating medium and excited at any frequency.

The 3D spatial displacement characteristics of an unloaded transducer can also provide information about the transducer's behavior and 3D spatial displacements before its application in SHM. Transducers with different characteristics compared to the manufacturer's data sheet could generate inappropriate *in-plane* (the S_0 and SH_0 in low frequency (LF) ultrasonic) and *out-of-plane* (the A_0 in LF ultrasonic) wave components during their application (48, 116). Therefore, 3D characteristics of the transducer can eliminate the defective transducers and design an array of transducers with the required characteristics. Moreover, it can also contribute to the modelling of a transducer, transducer-arrays or configuration of transducers (48).

1.6 Ultrasonic signal processing methods

In this dissertation, signal processing techniques are applied to the experimental B-scan signals to estimate and characterize defect parameters. In comparison to the conventional ultrasonic C-scan, a linear B-scan contains limited information about the damage in the structure. In order to extract the defective region and estimate its size and location, the B-scan requires post-processing. However, an efficient signal processing approach to extract the information from the superimposed, noisy, scattered GWs is still unavailable (117). The development of appropriate signal processing techniques triggers two positive outcomes. Firstly, defect estimation is possible and secondly, the developed technique can be automated for long-term applications in non-destructive testing and evaluation (NDT&E) (51, 52).

The flow chart of basic steps involved in ultrasonic testing is shown in Fig. 1.4, which can provide more information about the need for signal processing in ultrasonic NDT(53). It is clearly observed from Fig.1.4 that during the interaction of ultrasonic waves with the object, signals can be distorted due to one or many of the possible wave phenomena (reflection, refraction, mode conversion, scattering, etc.). Therefore, it might not be possible to extract signal parameters, such as amplitude, time of arrival or velocity, etc. That is why post-processing of ultrasonic signals is required to extract the parameters of the received GW signals which, in turn, could increase the accuracy of the estimation of size and location of damage in the inspected structure.

The signal processing of GW signals is a two-step process which involves signal de-noising and parametric estimation. The ultrasonic signal processing is performed in two subtasks: de-noising the received ultrasonic signal and detecting the faults/defects using parameter estimation (15). There have been many signal processing methods used by researchers for the noise removal and extraction of the information about defects in ultrasonic NDT which includes wavelet transform (WT) (53, 54, 118, 119, 120, 121), cross-correlation (53, 119, 122), Hilbert transform (HT) (53, 54, 122, 123, 124, 125), Hilbert Huang transform (HHT) (53, 122, 125, 126, 127), split-spectrum processing (SSP) (128, 129), short-time Fourier

transform (STFT) (130, 131), two-dimensional fast Fourier transform (2D-FFT) (63, 132, 133), Wigner Ville distribution (WVD) (134, 135) and mode decomposition techniques (empirical mode decomposition (EMD), ensemble empirical mode decomposition (EEMD), variational mode decomposition (VMD) (54, 124, 125, 126, 136), etc.

The promising features of one or more of these signal processing techniques can be combined to develop an effective signal processing algorithm. Hence, the selection of the proper signal processing method is also a challenging task. Discrete wavelet transform (DWT), HT, HHT, cross-correlation, 2D-FFT and mode decomposition techniques have been used in this research to develop the desired signal processing technique for the extraction of defect-features(53, 54, 55) from a single B-scan. The short overview of these methods is described in the following sub-Chapters.

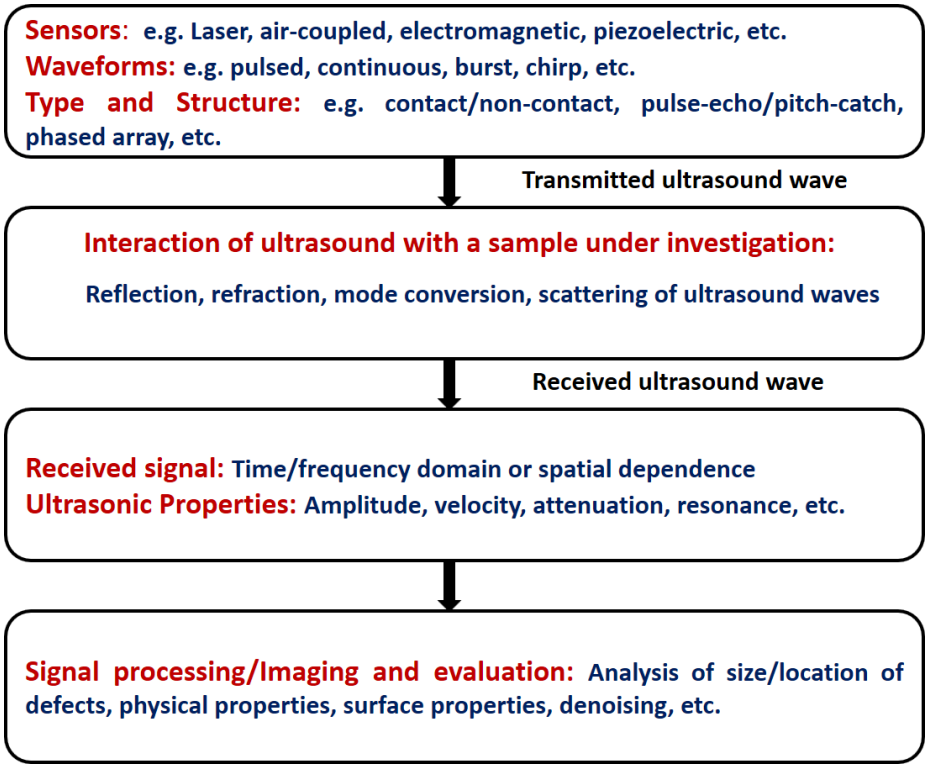

Fig. 1.4. Basic steps of ultrasonic NDT (53).

Discrete wavelet transform

One of the most widely used refining techniques for GW signals is wavelet processing. The DWT can efficiently remove the grainy and structural noise in

ultrasonic NDT of the composite structures (55, 118, 137, 138). The signal-to-noise ratio can be increased in a significant manner in order to improve the capabilities for locating and sizing defects. The non-stationary signals are processed both in time-domain and frequency-domain quite effectively by using DWT (118). The elementary signals after decomposing the time-domain signal are called wavelets. Generally, the WT can be called a correlation between the original signal and elementary wavelets. The special wavelet functions (mother wavelets) use the shifting and dilation methods for the generation of daughter wavelets. There are many wavelet families available for DWT. However, in the case of GW signals, no significant differences between these wavelet families are observed. However, the simplicity, orthogonality and energy preserving capabilities of Daubechies (db) wavelets facilitate to use them for decomposing the signals (139, 140)

The de-noising of GW signals using DWT is performed by modifying and manipulating wavelet coefficients (120, 141). Irrespective of the frequencies, the wavelet noising process reduces the signal components having smaller amplitudes and preserves the signal information. As DWT is based on the correlation between the wavelet function and signal, higher correlation results in a higher amplitude of decomposed signals. In this manner, the amplitudes of distorted and noisy signal components are reduced (53, 54, 55).

The soft or hard threshold method is widely used for discarding and selecting and the appropriate wavelet coefficients (142, 143). This process removes all coefficients which have the amplitudes lower than the used threshold. The signal is reconstructed from the remaining coefficients. However, GW signals passing through composite materials such as GFRP and CFRP may contain the correlated noise; therefore, this approach is not effective in that case (53). The soft-threshold method with a universal threshold can be the best alternative to deal with correlated noise for the alteration of wavelet coefficients (144). The amplitude detection technique with an appropriate threshold can be applied on de-noised wavelet signals for comparing the variations in amplitudes of signals in defect-free and defective regions to estimate the size and location of defects present on the structure (122).

The mathematical expressions and basic steps of the DWT de-noising process are described below:

- DWT utilizes high pass filters (HPF) and low pass filters (LPF) for analyzing the high and low frequencies, respectively, after selecting the appropriate wavelet function. The LPF is used for scaling and HPF is used for wavelet function. Consider that signal $x[n]$ has to be processed by DWT. The $h_{hp}[n]$ and $h_{lp}[n]$ are the filter functions for half-band high-pass filter and a low-pass filter, respectively. Level-1 decomposition is performed by eliminating a half of samples according to the Nyquist criterion. The response of both HPF and LPF can be given in the following equations: (145, 146).

$$y_h[k] = \sum_n x[n] \cdot h_{hp}[2k - n] \tag{1.21}$$

$$y_l[k] = \sum_n x[n] \cdot h_{lp}[2k - n] \tag{1.22}$$

where $y_h[k]$ and $y_l[k]$ are the respective responses of the HPF and LPF after sub-sampling by 2.

This process is repeated depending on the number of decomposition levels.

- The level k of decomposition can have any value between 1 and the maximum decomposition level (M) (147).

$$M = log_2 N; \text{ } N \text{ is the length of signal } x[n]. \tag{1.23}$$

The appropriate noise threshold by using a universal threshold for the detailed components can be expressed with (147):

$$T_N = \sigma_j^{\overline{noise}} \sqrt{2\log(N)} \tag{1.24}$$

where $\sigma_j^{\overline{noise}}$ is the estimated noise level.

In the last step, the inverse-DWT (IDWT) is applied to k detail components and k^{th} approximation component to generate the de-noised signal.

Cross-correlation

Cross-correlation is one of the simplest and yet effective signal processing approach which is used to find the correlation or similarity between two signals. However, the entire procedure contains many iterations of multiplications and summations. In the case of GW signals, cross-correlation is used for comparing the time-domain signals from the reference signal (53, 122). In this way, the correlation between the defect-free and defective signals can be estimated. Since cross-correlation depicts the extent of similarity between two signals, the most similar signals show the maximum possible correlation and *vice-versa*.

This technique is widely used to detect defects in ultrasonic GW testing by extracting the information about the defects and damages from the dispersive and scattered waveform in the defective region.

If two discrete-time signals $x_1[n]$ and $x_2[n]$ are to be analyzed, the cross-correlation function $C[n]$ can be given by the following expression (119):

$$C[n] = \sum_{-\infty}^{\infty} x_1[k] \cdot x_2[k + n] \tag{1.25}$$

Besides detecting the defective region, the time delay between the signals can also be estimated by estimating the correlation-peaks using cross-correlation. It should be noted that the length of two signals must be similar in order to apply cross-correlation. Digital windowing techniques can be used to change the length of test signals to be equal to the reference signal. Hence, digital windowing can also be easily incorporated with cross-correlation to process the windowed signals (148). It should be noted that

the reference signal can be considered in the defect-free region for the detection of a defect by processing a single B-scan using cross-correlation. By plotting the maximum correlation along the distance and applying an appropriate threshold level, defects can be detected (53).

Mode decomposition techniques

In order to decompose nonlinear multicomponent signals with nonstationary noise, such mode decomposition techniques as EMD, EEMD and VMD are used (124, 125, 126, 136). This way a multicomponent signal is converted into principal monocomponent signals. These monocomponent signals are called as modes or intrinsic mode function (IMF). The signal can be reconstructed by separating the noisy IMFs. A definition of a mode or IMF can be described by two conditions (53):

- A lower or upper envelope of IMF must have a zero mean.
- The difference between the number of extrema of an IMF and the zero-crossings must be 0 or 1.

Huang et al. (125) proposed the EMD decomposition method. The basic principle of EMD is the recursive method for detecting the maxima/minima of the signal. The mean of envelopes or IMF can be estimated by eliminating the HF signal components. Although EMD is the basis of mode decomposition techniques, there are some serious issues with the process which includes the forced stopping criterion, the effect of extrema calculation on the decomposition process and interpolation method.

Ensemble empirical mode decomposition

The EEMD is an improved version of EMD which is used to remove *mode mixing* and *end effect* problems associated with EMD. *Mode mixing* relates to the presence of several oscillations in IMF and the same oscillations in many IMFs. The problem of *end effect* occurs due to the estimation of envelopes by spline fitting in EMD (53, 149). EEMD adds white noise to the signal which uniformly distributes over the time-frequency region. This leads to convert the differently scaled signal bits onto the white noise-configured reference scale (53, 126).

The basic steps of EEMD are described as follows (126):

- If $x(t)$ is an original time-domain signal, the new signal $x_{new}(t)$ will be calculated by adding the white noise signal $n_T(t)$ (126):

$$x_{new}(t) = x(t) + n_T(t) \tag{1.26}$$

- First, the local minima and maxima of $x_{new}(t)$ are calculated. Then, the lower envelope $e_{min}(t)$ and upper envelope $e_{max}(t)$ are estimated by applying cubic spline interpolation. The mean value of $e(t)$ from the lower upper envelope can be calculated as follows (126):

$$e(t) = \frac{e_{max}(t) + e_{min}(t)}{2} \tag{1.27}$$

- The difference $d(t)$ between the new signal $x_{new}(t)$ and mean value $e(t)$ is given by the following equation (126):

$$d(t) = x_{new}(t) - e(t) \tag{1.28}$$

- If $d(t)$ fits in the definition of IMF, the stopping criterion is correct and fulfilled. The $d(t)$ will then be the i^{th} IMF and is denoted as $c_i(t)$. The residual $r_i(t)$ will replace the signal $x_{new}(t)$ as follows (126):
-

$$r_i(t) = x_{new}(t) - c_i(t) \tag{1.29}$$

$r_i(t)$ will be the new data set and the shifting process will again be performed to get further IMFs.

- If the IMF definition is not fulfilled, $d(t)$ replaces x(t) in Eq. (1.26). Afterward, the following steps, as given in Eq. (1.27) to Eq. (1.29) are repeated until the IMF definition is fulfilled and the residue becomes monotonic.
- The number of trials (T) are continuously compared to the ensembles (E) and T is replaced by T+1 for Eq. 2.6 until (T<E). Therefore, the entire procedure is repeated with new white noise (53, 126).
- The final step includes the computation of ensemble mean for each IMF ($\bar{c_k}$) and the respective residue ($\bar{r}$) (126):

$$\bar{c_k} = \frac{1}{E}\sum_{T=1}^{E} c_{k,T} \tag{1.30}$$

$$\bar{r} = \frac{1}{E}\sum_{T=1}^{E} r_T \tag{1.31}$$

The IMFs and residue are added together for the reconstruction of signal as given in (126):

$$x(t) = \sum_{i=1}^{n} \bar{c_i} + \bar{r} \tag{1.32}$$

The EEMD with adaptive noise can improve reconstruction and mode separation (150).

Variational mode decomposition

The basic principle of VMD is based on adapting the Weiner filter translating into the distinguished bands. It was proposed by Dragomiretskiy and Zosso (136) to overcome the limitations associated with EMD and EEMD. VMD is the upgradation of EMD and EEMD. However, it is more efficient in removing noise and distortions associated with ultrasonic GWs in composite materials. Moreover, the computation/simulation time is much shorter than the EMD. The basic features of VMD are as follows (54, 55):

- All oscillating components can be separated because VMD does not consider amplitudes and frequency during the process.
- The decomposition of modes is possible in an exact manner or in the sense of least squares by overcoming the inverse problem of EMD. Hence, each mode occupies a unique bandwidth.

The flowchart (Fig. 1.5) presents sequential steps for the calculation of bandwidth of a mode (54). First, the Hilbert transform is applied to each IMF to produce an analytical signal and unilateral frequency spectrum can be obtained. After adding the exponentials with the tuning of the center frequency, each frequency spectrum can be shifted to the baseband. In the last step, bandwidth is estimated by H1-Gaussian smoothness (136).

The mathematical expression of the variational problem is given in (136)

$$\min_{u_k,\omega_k} \left\{ \sum_{k=1}^{K} \left\| \partial_t \left(\left[\delta(t) + \frac{j}{\pi t} \right] * u_k(t) \right) e^{-i\omega_k t} \right\|_2^2 \right\} \tag{1.32}$$

where u_k (k = 1,2…. K) is the k^{th} mode for a real-value signal (x); ω_k is the k^{th} center frequency; δ is the Dirac distribution.

$$\sum_{k=1}^{K} u_k = x \tag{1.33}$$

It should be noted that the reconstruction constraint is defined by utilizing the characteristics of Lagrangian multipliers and quadratic penalty. It is also called as augmented Lagrangian (151, 152).

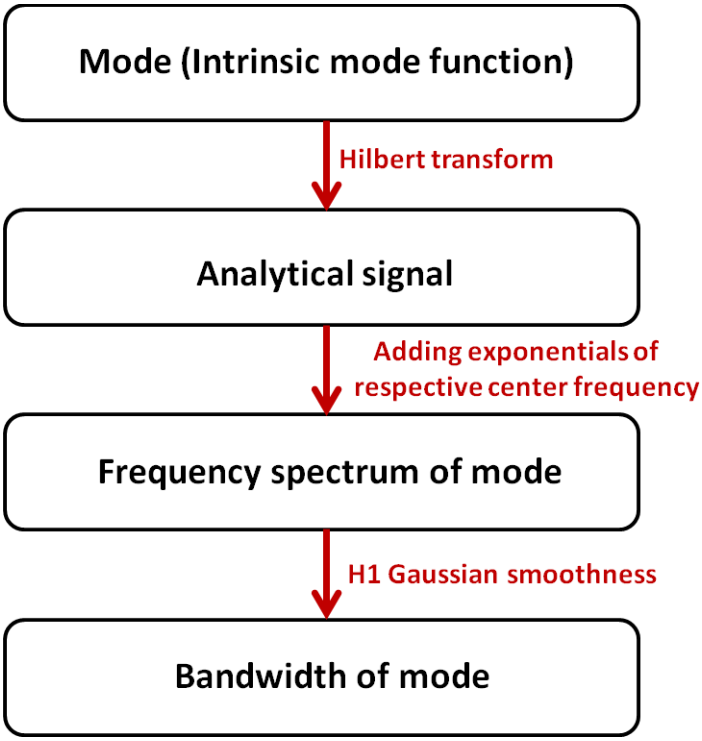

Fig. 1.5. Steps showing the computation of the mode-bandwidth in VMD (54).

Hilbert transform and instantaneous characteristics of a signal

HT is used to extract the analytical signal from a real-value signal. Instantaneous characteristics of a signal can be estimated. Hence, HT can be used to extract the instantaneous amplitude and instantaneous frequency variations of the GW signals in the defect-free and defective regions with respect to the time (124). Moreover the comparative analysis of instantaneous amplitudes can also provide information about the time of arrival of signals (53, 54, 55). If $x(t)$ is a real-value signal, the HT of the signal, $X_h(t)$ can be given in (124, 153):

$$X_h(t) = \frac{1}{\pi}\int_{-\infty}^{\infty} \frac{x(v)}{t-u}\,du \tag{1.34}$$

The analytical signal $x_a(t)$ can be extracted from a real-value signal $x(t)$ and its HT $X_h(t)$ as expressed by the following eq. (124, 153):

$$x_a(t) = x(t) + iX_h(t) = A_i(t).e^{i\varphi(t)} \tag{1.35}$$

where $A_i(t)$ and $\varphi(t)$ are instantaneous amplitude and instantaneous phase variations, respectively, of the real-value signal $x(t)$.

The mathematical expression of instantaneous amplitude $A_i(t)$ and instantaneous frequency $f_i(t)$ can be given by (124, 153):

$$A_i(t) = |x(t) + iX_h(t)| \tag{1.36}$$

$$f_i(t) = \frac{1}{2\pi}\frac{d\varphi(t)}{dt} \tag{1.37}$$

There is always the possibility of mode mixing in the GW signals after the interaction of layered composite materials. The instantaneous characteristics in such a case could give ambiguous and undesired results because an authentic analytical signal cannot be obtained with the presence of harmonics (154). Therefore, before processing by HT, EMD or VMD decomposition techniques should be applied on A-scans of GW signals in order to obtain monocomponent signals (54, 55).

Hilbert Huang transform

Huang et al. proposed the HHT to process and characterize non-stationary signals (53, 122, 125, 126). In principle, HHT is the combination of EMD/EEMD and HT. The decomposition techniques EMD/EEMD are first applied for the decomposition of nonstationary and nonlinear signals into the stationary or monocomponent IMFs and afterward, HT is used to obtain instantaneous amplitude and frequency characteristics. The local energy or amplitude distributions of the decomposed GW signals represented in the time-frequency plane are known as the Hilbert Huang spectrum. Previous research works observed that HHT can have a significant role in signal processing in NDT (53, 155, 156).

Two-dimensional fast Fourier transform

In the ultrasonic NDT, the 2D-FFT is used to transform the B-scan (time–distance measurements) into the phase velocity-frequency domain (50, 53, 55). The basic principle of the 2D-FFT is the representation of GW propagation by the transfer function (H) of arrival time and scanning distance. This in turn is transformed into frequency(f) – wavenumber (k) space. The mathematical expression of the 2D-FFT can be given as (63, 132):

$$H(k,\omega) = \iint_{-\infty}^{+\infty} u(x,t)\cdot e^{-j(kx+\omega t)}dxdt \tag{1.38}$$

Where ω is the angular frequency ($\omega = 2\pi f$) and f is the frequency; x is the distance, t is the arrival time and k is the wavenumber.

The phase velocity dispersive characteristics with respect to the time can be easily obtained as the phase velocity is the ratio of ω and k. The 2D-FFT can also be used to suppress the reflected signals from ultrasonic B-scan from the opposite edge

of the layered composite structures for further processing. It could be very useful to estimate the signal parameters in the case when phase velocity dispersive characteristics cannot provide the desired information due to mode mixing, reflection, scattering and another wave phenomenon (55).

Split-spectrum processing

Initially, the SSP development was performed by utilizing the frequency agility methods which were being used in radar applications (157). Later on, it was used to improve the improvement SNR by reducing the grainy scattering in the conventional ultrasonic testing (158).

In general, the basic principle of SSP is to convert the spectrum of ultrasonic GW signal into various sub-bands by using a bank of band-pass filters (BPF). The center frequencies of sub-bands are incremented in a prescribed order. Later, non-linear signal processing algorithms are applied to these sub-bands in order to achieve the output signal. The functioning of SSP can be expressed by a block diagram as presented in Fig. 1.6.

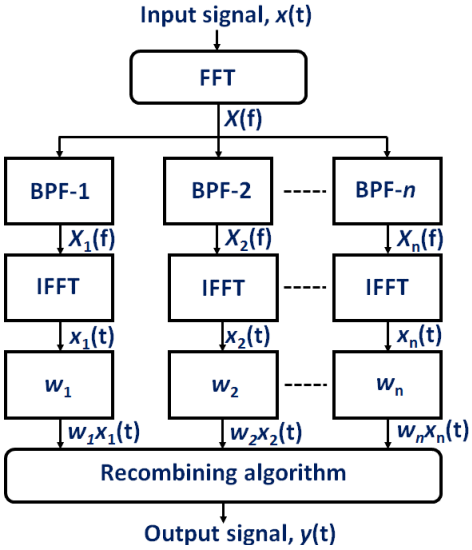

Fig. 1.6. Block diagram of basic operation of SSP

The basic steps of the SSP process are described as follows:

- Firstly, the input signal (x(t) is converted into the frequency domain (X(f)) by applying FFT.
- X(f) is filtered by a bank of bandpass filters.

- The IFFT is applied to the output of bandpass filters (X_i(f), i =1, 2, …. , n) to revert back to the time-domain signals.
- Appropriate weighting factors (w_i; i =1, 2, …. , n) are applied to normalized the non-linear time-domain signals.
- Finally, the signals are recombined by utilizing a recombination algorithm to receive an output signal (y(t)).

The number of filters (N) required for the SSP application is given by the following eq. (1.39)(159):

$$N = \frac{B}{F} + 1 \tag{1.39}$$

where B is the operating bandwidth and F (F=1/T; T is the total signal duration) is the filter separation.

The bandwidth of each BPF (B_{BPF}) is required to be three to four times of the filter separation (129). It should be noted that band-pass filtering can reduce temporal resolution and therefore, application of filter banks is one of the most serious steps in the SSP.

There are many SSP recombination algorithms available for reducing coherent noise presented in ultrasonic GW signals such as polarity thresholding (PT), polarity thresholding with minimization (PTM), mean algorithm and minimization algorithm, etc.(160). The bandwidth of each BPF (B_{BPF}) is required to be three to four times of the filter separation (129). It should be noted that band-pass filtering can reduce the temporal resolution and therefore, the application of filter banks is one of the most important steps in the SSP. The limitation of SSP is that algorithm entirely depends on the parameters of filter banks. Moreover, the optimal parameters are not certain and the processing time is longer for signal decomposition.

Short-time Fourier Transform

The scattering, dispersion and attenuation of GW signals after interaction with the composite structure is frequency dependent. Therefore, the analysis of nonstationary GW signals is a complex mechanism. Time-frequency analysis of GW signals is an effective technique to achieve selective frequency distribution at a span of time or selective time information at a certain frequency. There are many time-frequency analysis methods and STFT is being used for the analysis of GW signals in composite structures (161). In general, the STFT is modified FT in which a longer time signal is divided into different segments and FT of each segment is computed.

The STFT of a time-domain signal $x(t)$ can be expressed with (131, 162, 163):

$$STFT(t,f) = \int_{-\infty}^{+\infty} x(\tau) \cdot w(\tau - t) e^{-2j\pi f\tau} d\tau \tag{1.40}$$

where, t is time variable, τ is the time lag, $w(t)$ is the window function for analyzing the local spectrum of a signal.

The spectrogram of a signal $x(t)$ can be expressed with (131, 162, 163):

$$S_p(t,f) = |STFT(t,f)|^2 \tag{1.41}$$

There are many window functions which can be selected depending on the requirement. Better frequency resolution can be achieved by applying a wider window at the cost of time resolution. Conversely, a better time resolution can be obtained by applying a narrow window at the cost of frequency resolution. Therefore, an optimal solution is the key step in this approach.

Wigner Ville distribution (WVD)

Similar to STFT, WVD is also used to analyze the time-frequency distribution of nonstationary signals in both time and frequency domain. In contrast to the STFT and referring to the theoretical definition of WVD, the window function is not required. Hence, the signal of any length can be analyzed. However, a windowed WVD is required in most practical applications (134). The time-frequency analysis in short time spans can be performed by using the windowed WVD. Most common windows which are used in WVD include Rectangular, Hanning, Hamming and Blackman.

The WVD and windowed WVD is defined by eq. (1.41) and eq. (1.42) respectively (135, 164):

$$W(t,f) = \int_{-\infty}^{+\infty} s\left(t+\frac{\tau}{2}\right)\cdot s^*\left(t-\frac{\tau}{2}\right)\cdot e^{-2j\pi f\tau}d\tau \tag{1.42}$$

$$W(t,f) = \int_{-\infty}^{+\infty} s\left(t+\frac{\tau}{2}\right)w^2\left(\frac{\tau}{2}\right)\cdot s^*\left(t-\frac{\tau}{2}\right)\cdot e^{-2j\pi f\tau}d\tau \tag{1.43}$$

Where s(t) is an analytical signal of a real signal $x(t)$ and $w(t)$ is a window function.

There are some limitations associated with the WVD of a multi-component signal. One of the major concerns is the *ghost patterns* which are exhibited due to the interference of the multi-components. In order to solve this problem, smoother WVD is required which is called Pseudo Wigner–Ville (PWVL) (165). In the process of PWVL, the time-frequency smoothing is performed for the reduction of the amplitudes of unauthentic terms. The applications of WVD in the ultrasonic NDT included in the defect detection, decomposition of multi-component signals, time-frequency analysis and estimation of phase and group velocities of the propagating wave modes (165, 166, 167).

A comparison of the most widely used signal processing techniques used to process the GW signals is presented in Table. 1.2.

After reviewing and comparing all ultrasonic signal processing techniques described in Chapter 1.6, the following techniques have been considering the estimation of defects and characterization of the GW signals in the defect-free and defective regions.

- The DWT can be used for de-noising nonstationary GW signals. A large selection of wavelet families and threshold techniques makes it best suited for de-noising of GW signals after interaction of multi-layered composite structures.
- Mode decomposition techniques along with HT or HHT are the best available techniques to extract the instantaneous characteristics of GW signals due to their ability to convert multicomponent signals into monocomponent and to deal with correlated noise.

Table 1.2. Comparison of ultrasonic signal processing techniques

Name	**Advantages and applications**	**Disadvantages and limitations**
DWT	*Efficient method in both time and frequency domains to process non-stationary signals *Signal analysis is faster than Fourier transform. Wavelets are localized in both time and as compared to localized in only frequency in Fourier transform. * Useful method to improve defect/flaw detection and estimation in noisy environments and grainy materials.	*A small change/shift in input signal produces large variations in energy distribution of DWT
Cross-correlation	*Detection of signals in a noisy environment and delay estimation. * Can be combined with window methods so that ultrasonic signals can be segmented at different distances.	* Not efficient for scattered signals due to inhomogeneity in structure or when noise is correlated with the received signal (signal de-noising must be applied)
2D-FFT	*To estimate the phase velocity dispersion curves of propagating wave modes. * To suppress the reflected signals from the ultrasonic B-scan.	*Not efficient for the estimation of defect features. *Inaccurate results in the case of variable thickness of the structure
Mode decomposition techniques and HHT	*To estimate instantaneous characteristics of GW signals. *To convert multicomponent signals into monocomponent. *To estimate the time delay by comparing normalized amplitudes of monocomponent signals.	* Time-consuming. *Only for the characterization of GW signals (not efficient for defect estimations)
STFT	* Time-frequency distribution of signals. * Defect detection.	*Not efficient for defect estimation in the presence of correlated noise. *Compromise between a time or frequency resolution
SSP	*Defect estimation and noise suppression in	*Processing time is long.

	grainy materials. *Time-frequency distribution of signals.	*SSP algorithm depends on the number of filters and their parameters hence they are not robust.
WVD	*Defect detection and measurement of phase and group velocities of GWs. *Time-frequency analysis	*Not efficient with multicomponent signals. * Existence of negative power for some frequency ranges

1.7 Challenges in the inspection of wind turbine blade

Wind energy is one of the most prominent renewable energy resources available in the world. The WTB, generally constructed from GFRP and CFRP, is one of the most frequently damaged parts of the wind turbine. The blades are expensive and the installation cost of the 10 to 50 meter WTBs typically accounts for 10–20% of the overall cost of installation (168). The random nature of wind's force produces varying or cyclic loads to the wind turbine, therefore flaws, breakage and damages can exist in any component of the wind turbine blade (169). Moreover, wind turbine blades are more sensitive due to very high stress which may easily lead to damages and defects. Regular maintenance and inspection of wind turbine blades are necessary to avoid any system failure (170, 171, 172). There is a number of non-destructive testing methods which can be used to assess the quality of materials used in the manufacturing process of turbine blades (47). However, the dimension and complexity of wind turbine blades and limitation in applicability and accuracy of some methods make them unsuitable for on-site inspection of wind turbine blades (173). Due to the availability of a wide range of transducers and ability to travel a long distance, ultrasonic NDT is extensively used for the inspection of these type of structures (174, 175, 176, 177). That is why a segment of WTB is considered as an object in this dissertation to be inspected by ultrasonic GWs. However, the experimental approach itself cannot provide information about the dimension of the defects. The post-processing (signal processing or image processing) of the acquired experimental results have the same importance as the experimental approach. The main purpose of the NDT techniques using ultrasonic GWs is to develop a fast, cost-effective and less complex measurement technique with appropriate post-processing methods.

Although non-contact ultrasonic testing techniques can cover a large surface area, they have certain limitations due to the layered structures, thickness and low acoustic contact (178). In the field of contact ultrasonic testing, most of the research work and commercial testing of WTB is performed by pulse-echo techniques (46, 170, 175) and ultrasonic phased-array (72, 177). However, the real-time testing of WTB is still quite complex and challenging because of its composite and thick structure and one sided access. Therefore, more innovation and research is required in this field (179). Moreover, the limitation associated with the pulse-echo technique (less flexible and unsuitable for large structures) and the phased-array method (expensive and complex due to added number of devices) provide the motivation to develop

measurement techniques for smaller and larger structures based on pitch-catch operation which is more flexible as compared to the pulse-echo and economical as compared to the phased-array method (see Chapter 2 and Chapter 4 for details).

1.8 Conclusions

1. Ultrasonic guided waves are widely used for non-destructive testing and structural health monitoring of large and complex geometrical structures in a wide variety of applications. Guided waves are very sensitive to various kinds of defects, can travel a long distance and have many more other advantages as compared to other techniques. However, such wave mechanism as dispersion, mode conversion, reflection, refraction or attenuation during the interaction of guided waves creates complexity and ambiguity in defect estimation.
2. Out of the three most common scanning techniques used for ultrasonic testing, the pitch-catch technique is the most suitable for SHM of large composite structures and the structures having only one-sided access. The pitch-catch technique is flexible in nature as the location of transmitting and receiving transducers can be altered as per requirement.
3. The brief review of contact and non-contact ultrasonic testing methods reveal that non-contact methods can be used in different environments, in the inspection of different materials, at variable temperatures and for the structures which are not accessible easily from the test-site. However, contact type methods are still popular due to the easy handling of transducers and better acoustic contact between the transmitter and contact surface. Moreover, the configuration of contact-type methods as per requirement is very easy. One such configuration is the two point-type transducers fixed on a moving panel with an optimal separation distance. This configuration is suitable for the development of a measurement system for a short distance GW testing of a composite structure.
4. For a long distance GW testing and SHM of the structures, a transmitting transducer must be an integral part of the structure and an MFC transducer is the most widely used for such applications. Due to its compact size and low weight, it can be embedded or glued on the structure under investigation. MFC transducers are well-known actuators and sensors of the Lamb waves and widely used for non-destructive testing and structural health monitoring of the structures. However, effective generations of such transducers depend on its directivity and displacement characteristics of the propagative GW modes.
5. By knowing the directivity pattern of a transducer, the exact location of a transducer can be determined to effectively inspect the structure. Moreover, the excitation frequency, the appropriate propagating wave mode or the configuration of transducers can be selected to cover up the large region. This optimizes the overall cost of the NDT system. Therefore, a versatile analytical

model is required to predict the directivity of a contact-type transducer in any propagation medium and at any excitation frequency.

6. The three-dimensional displacement characteristics of an unloaded vibrating transducer before the experimental analysis can provide information about the applicability of the transducer in ultrasonic NDT and SHM applications. It can also provide information about the most dominant component of the propagating wave (the A_0, S_0 or SH_0 in the LF ultrasonic).
7. There are many ultrasonic signal processing methods that are available, such as wavelet transform, Hilbert transform, mode decomposition techniques, two-dimensional fast Fourier transform. However, the processing of received GW signals to extract the defect parameters requires a signal processing algorithm combining their positive features. The discrete wavelet transform is one of the most frequently used techniques to remove grainy and structural noise from the received guided wave signals in the process of ultrasonic NDT of composite structures. Wavelet transform can be combined with the amplitude detection technique for the estimation of size and location of defects. The cross-correlation of all A-scans of a single ultrasonic B-scan with the defect-free A-scan can provide information about the defective region. Moreover, the cross-correlation is also used for the time delay estimation. The instantaneous characteristics (instantaneous frequency and instantaneous amplitude variations with respect to time) of GW signals using Hilbert transform of a nonstationary, nonlinear and multicomponent signal containing various harmonics is not possible. Therefore, mode decomposition (empirical mode decomposition, ensemble empirical mode decomposition or variational mode decomposition) must be applied before applying Hilbert transform in order to convert the multi-component signal into monocomponent.

After reviewing the literature related to GW testing, a configuration of transducers for short and long-distance GW testing, possible techniques to improve the estimation of defects in structures using ultrasonic GWs and signal processing techniques for the post-processing of GW signals, the research plan of the dissertation is finalized and the workflow is presented in Fig. 1.7. The following chapters present the development of the measurement techniques for the defect detection and estimation and characterization of GWs in the composite structure by short-distance GW testing (using a pair of contact-type transducers) and by long-distance GW testing (using a glued/embedded transmitter *e.g.* P1-type MFC and a contact-type receiver). However, before proceeding to the long-distance GW testing, three-dimensional displacement characteristics and directivity of the ultrasonic contact-type transducer which can be glued on the structure to increase the accuracy in long-distance GW testing is estimated.

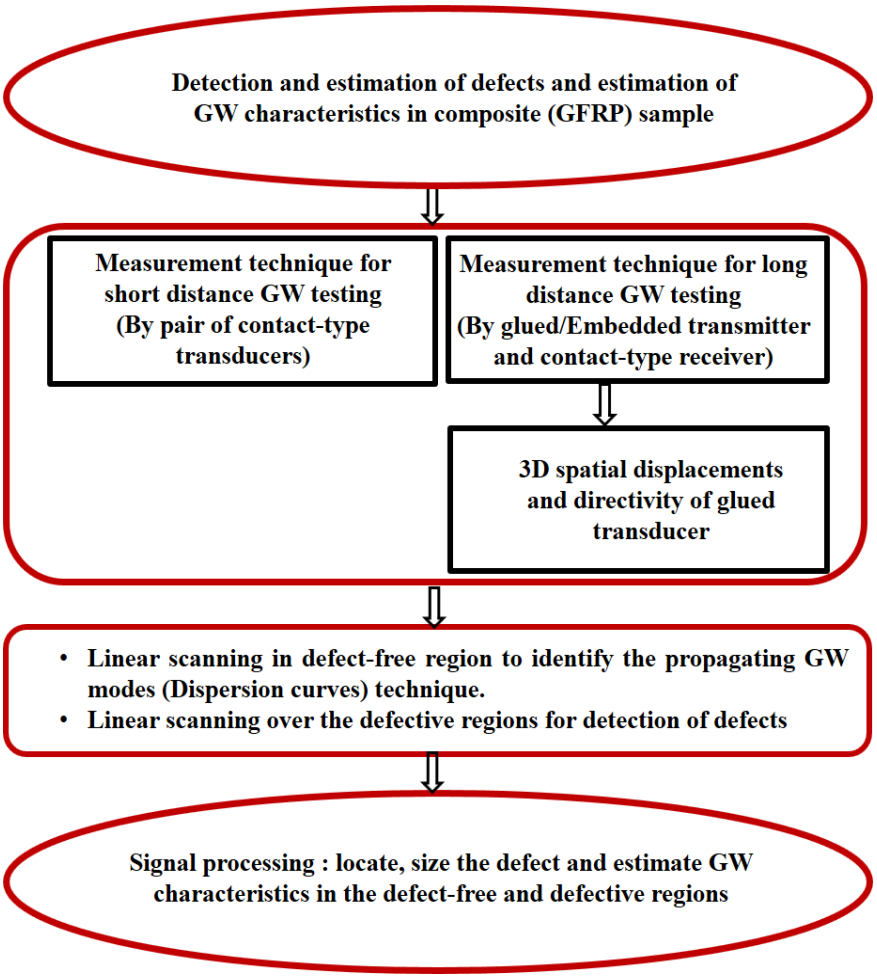

Fig. 1.7. A schematic of work flow of dissertation

It should be noted that only disbond-type defects created by the mechanical process (milling process) are analyzed in this research. In the short-distance GW testing technique, disbond-type defects located on the trailing edge of segment of WTB constructed from GFRP are analyzed. In the long-distance GW testing technique, disbond-type defects located on the main spar of the same sample are analyzed.

2. MEASUREMENT TECHNIQUE BASED ON SHORT DISTANCE GUIDED WAVES

2.1 Demand and motivation

As discussed in Chapter 1.4.1, contact-type transducers have limitations of low scanning speed and smaller coverage region during NDT of large composite structures by using GWs. However, for short-distance GW testing contact-type transducers (transmitter and receiver) can be the best solution in order to develop an effective measurement technique due to their easy handling and good acoustic contact, since a coupling medium between the transducers and the contact surface is applied. As contact-type transducers can be easily configured to operate in a pitch-catch mode, this approach is used in this Chapter to extract defect features in a composite structure.

During the experimental process, only a single linear scan (B-scan) or an A-scan signal is acquired using GWs which is very useful for testing and inspecting complex configured structures where conventional two-dimensional scanning process (C-scan) is not possible. The only condition is that the region of the structure to be inspected should be in the range (should be scanned over) of the receiving transducer. Moreover, a single B-scan or A-scans require a far shorter time as compared to the C-scan. However, only the lesser amount of experimental data, noise and disturbance of GW signals due to associated GW mechanism (reflection, refraction, scattering mode conversions, attenuation, etc.) in layered structures are the negative factors for the identification of damages in the structure from linear scanning.

The experimentally acquired signal intensity variations (B-scan) on the time-space may visually provide information about the existence of damage in the object. However, the signal processing/refining of GW signals is necessary to accurately calculate the size and location of defects and characterize the GW signals in the defect-free and defective regions. Before estimating the size and location of defects, the GWs must be de-noised by appropriate signal processing to remove nonstationary and structural noise. The instantaneous characteristics of the GWs can be calculated only after converting the multicomponent signals into monocomponent.

This Chapter deals with the development of a measurement technique based on short-distance GW testing with the adaptation and accumulation of ultrasonic signal processing techniques, which leads to the extraction and characterization of defects/damages located at various positions of the composite sample with a complex geometrical structure. The selected sample was a segment of a wind turbine blade (WTB). The multi-layered composite material used to manufacture the sample was GFRP. As discussed in Chapter 1.7, the blade of the wind turbine is one of the most sensitive and damage prone components as it has to sustain under cyclic loads. Moreover, it is constructed from a multi-layered composite structure and possesses a complex geometry, thus the segment of WTB is selected as an object. The disbond-type defects of different sizes (15 and 25 mm) were located at the trailing edge of the sample. A pair of contact-type transducers (see Chapter 2.2 for details) fixed on a moving panel with 50 mm separation is used for the investigation. The fixed distance

between the transducers reduces the attenuation and dispersion caused by the variable distance. Moreover, both transducers are point-type operating in thickness mode. Hence, they are more sensitive to the amplitude variations of propagating waves. The simple amplitude detection technique is useful in order to distinguish between the defect-free and defective region. There are only a few research works testing WTB based on the pitch-catch operation, therefore, this technique motivates to develop an improved configuration of similar kind of transducers by reducing the separation distance in the future.

The schematic of the measurement technique is presented in Fig. 2.1. Firstly, the experimental analysis of the sample is performed by using contact-type transducers operating in a pitch-catch mode. The resulting experimental B-scan is first processed to size and locate (defect estimation) the defect by using wavelet de-noising and amplitude detection. Then, HHT is applied to compare the instantaneous characteristics of GW signals in the defect-free and defective regions.

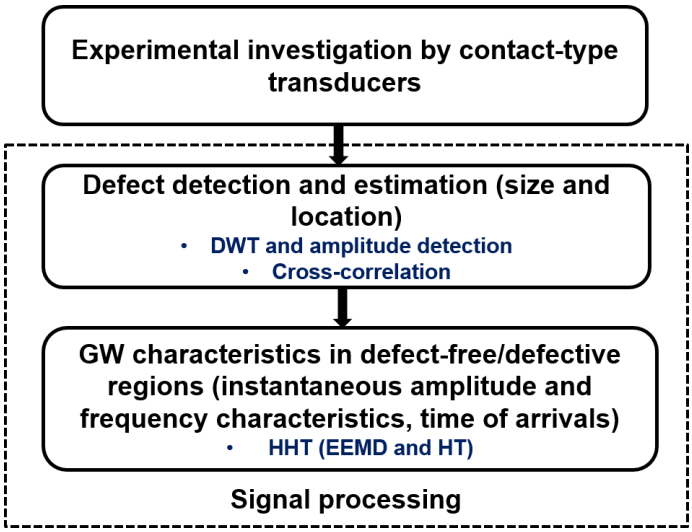

Fig. 2.1. Schematic of measurement technique for the defect estimation and characterization in composite structure by short-distance ultrasonic GWs.

The organization of Chapter is:

- Experimental investigation of the sample for the estimation of disbond-type defects with 15 and 25 mm diameters located on its trailing edge is performed in Section 2.2 by using a pair of contact-type transducers fixed on a mechanical moving unit.
- The development of a signal processing algorithm based on DWT, EEMD, 2D-FFT, cross-correlation and HHT to extract the features of disbond-type defects from the experimental signals is presented in Section 2.3. The GW characteristics in the defect-free and defective regions are also compared in this Chapter.

- The conclusions of the Chapter including the limitations and issues are presented in Section 2.4.

2.2 Experimental investigation on the trailing edge of sample containing disbond-type defects

2.2.1 Devices and sample

The contact-type ultrasonic transducers, made of piezoceramic material (PZ 29) are used in the experimental investigation. The contact-type ultrasonic transducers require a protection layer for testing composite materials using contact methods and providing the point-type contact. Therefore, wideband ultrasonic transducers with a convex protection layer (diameter of the contact surface ≤ 3 mm) containing -6 dB bandwidth up to 350 kHz (50, 53, 55, 101) are used.

The descriptive cross-section of the contact-type transducer is shown in Fig. 2.2 (101). The transducer consists of a piezoelectric element, a constant protector and a damper. By using two wires, the piezoelectric element is connected to the connector which is fixed into the cap of the housing. The entire arrangement was surrounded by a soft material layer and mounted into the housing. The replaceable protector (convex protector) and the fixing ring are the replaceable parts of the transducer. At excitation frequency of 220 kHz, 3-period burst, the frequency response of the transducer without a convex protector and with a protector are presented in Fig. 2.3a and Fig. 2.3b, respectively.

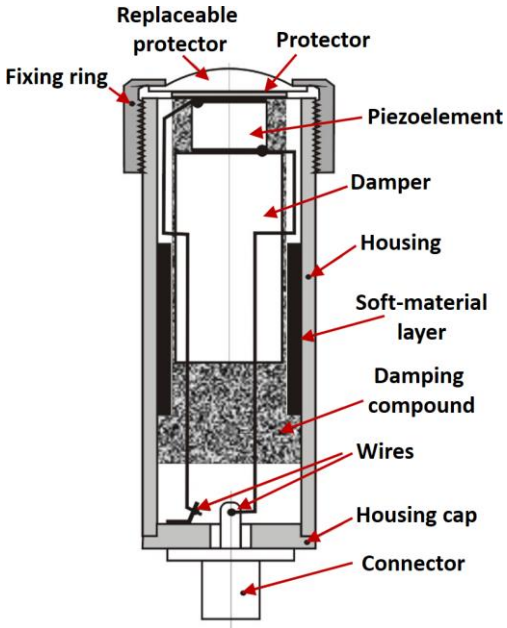

Fig. 2.2. A cross-section of the piezoceramic (PZ 29) contact-type transducer (Adopted from (101))

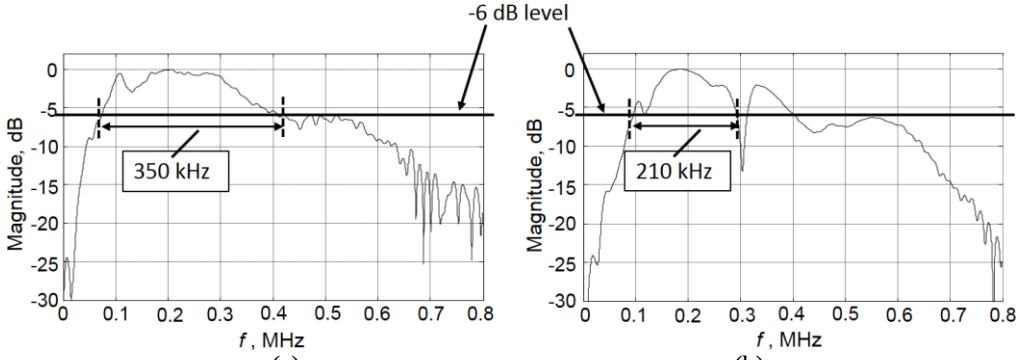

Fig. 2.3. Frequency response of the piezoceramic (PZ 29) contact-type transducer without a protection layer (a) and with a protection layer (b) (Adopted from (101))

Fig. 2.3a clearly shows that -6 dB bandwidth of the transducer without using the protection layer is up to 350 kHz whereas, 210 kHz bandwidth is achieved at -6 dB level with a protection layer. The parameters of the contact-type transducer are presented in Table 2.1.

Table 2.1. Parameters of contact-type receiver (53, 54, 55)

Parameters	**Description**
Material	Piezoceramic-PZ 29
Maximum value of -6 dB bandwidth	350 kHz
-10 dB bandwidth	35–640 kHz
Center frequency	190 kHz
Diameter of protection layer at bottom	2 mm

The cross-section of the WTB and the photo view of the GFRP sample are shown in Fig. 2.4a-b. Two artificial defects of 15 and 25 mm in diameters created by the milling process are located on the trailing edge of the WTB segment. There was a gap of 330 mm between the nearby ends of two defects (53).

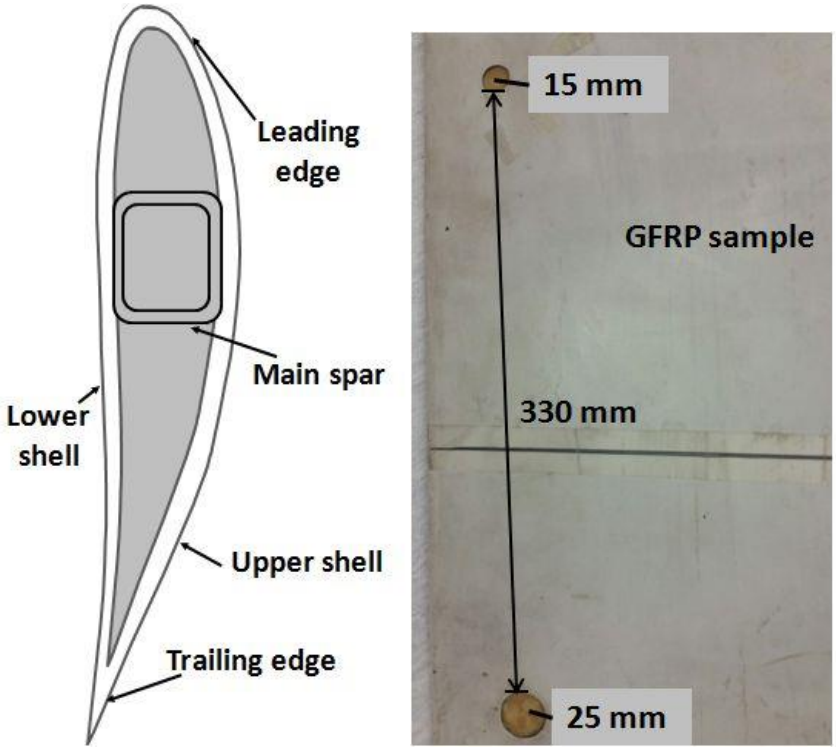

(a) (b)

Fig. 2.4. Cross-section of the segment of a wind turbine blade (a) and photo view of the test sample of a blade segment constructed from GFRP material (b) (53).

Table 2.2. Properties of GFRP material (55)

Parameters	**Numerical Value**
Paint or Surface layer:	
Density (ρ)	1270 kg/m^3
Young's modulus (E)	4.2 GPa
Poisson's ratio (υ)	0.35
Unidirectional GFRP layer:	
Density (ρ)	1828 kg/m^3
Young's modulus (E_1)	42.5 GPa
Young's modulus (E_2)	10 GPa
Poisson's ratio (υ_{12})	0.26
Poisson's ratio (υ_{23})	0.4
In plane shear modulus (G_{12})	4.3 GPa
Epoxy:	
Density (ρ)	1260 kg/m^3
Young's modulus (E)	3.6 GPa
Poisson's ratio (υ)	0.35

2.2.2 Experimental analysis

The entire experimental process consists of two parts. In the first experiment, linear scanning is performed in the defect-free region of a sample by using contact-type transducers for the estimation of phase velocity of the dominant mode of the propagating wave. One transducer was fixed at one position and another transducer was scanned away up to 200 mm to record the GW signals. The transmitter was excited with 150 kHz, 3 periods of burst with Gaussian symmetry (53). The scanning step used in the experiment was 0.5 mm and the sampling frequency was 100 MHz. It should be noted that a contact-type receiver operates in thickness mode which is more sensitive to pick up the *out-of-plane* dominating components of the A_0 mode in spite of excitation of both A_0 and S_0 modes. The LF ultrasonic system was used in the experiment (53, 54, 55). The characteristics of the LF ultrasonic system developed by Ultrasound Research Institute of Kaunas University of technology are described in Table 2.3.

Table 2.3. Parameters of LF ultrasonic system (53, 54, 55)

Parameters	**Numerical Value**
No. of input channels	2
No. of bits of analog-to-digital converter	10
Overall system gain (maximum)	113 dB
Ultrasonic system to computer interface	USB V.2
Frequency range	20 kHz-2 MHz

The photo of experimental investigation is shown in Fig. 2.5a and the acquired B-scan image is presented in Fig. 2.5b. After applying the 2D-FFT (see Chapter 1.6 for details) to the B-scan, the amplitude distributions in the time-space domain are converted into the wavenumber-frequency domain. Finally, the phase velocity-frequency characteristics (dispersion curve) can be obtained by converting wavenumbers into frequency. The estimated phase velocity dispersion characteristics along the frequency are shown in Fig. 2.5c. Since the contact transducers (both transmitter and receiver) are very sensitive to pick up A_0 mode, the dominant A_0 mode is clearly observed with phase velocity of 1160 m/s at the excitation frequency (150 kHz). The weak S_0 mode is also observed. Therefore, A_0 mode is the interesting mode of consideration when using the same contact-type transducers in further investigation of the sample.

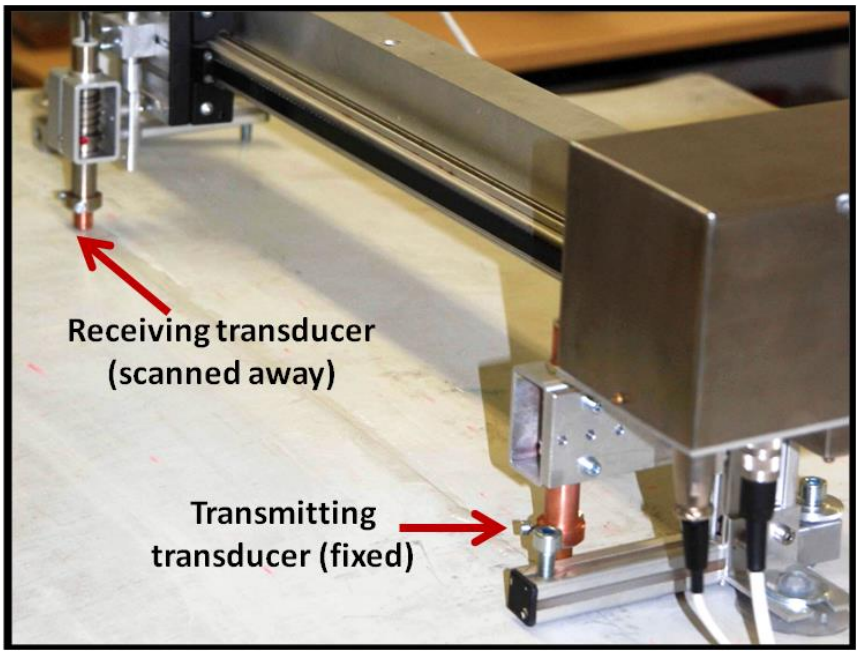

(a)

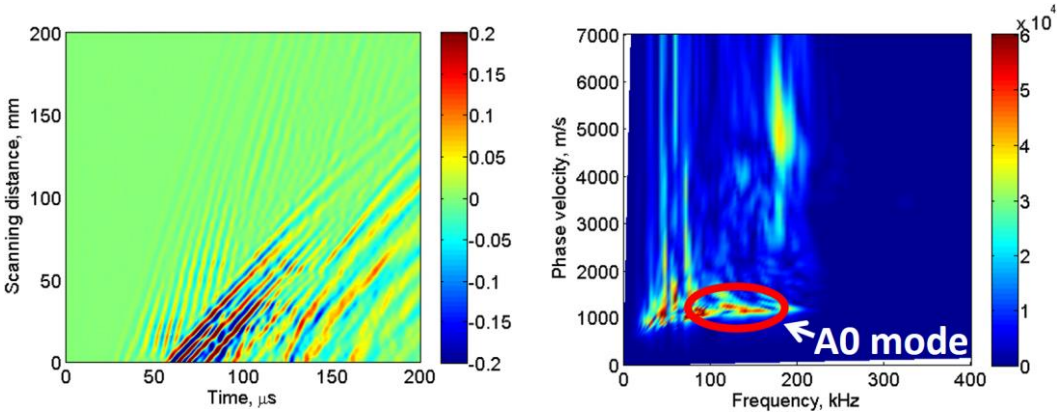

(b) (c)

Fig. 2.5. Linear scanning of sample in the defect-free region: Photo of experimental set-up (a); B-scan image (b); phase velocity dispersion characteristics (c) (49).

A second experiment (Fig.2.6) is performed to acquire a B-scan over the defective regions. Two contact-type transducers (same transducers used in the previous experiment as shown in Fig. 2.5a) were mechanically mounted/fixed on a moving mechanical unit/panel to form a special configuration as shown in Fig. 2.6a.

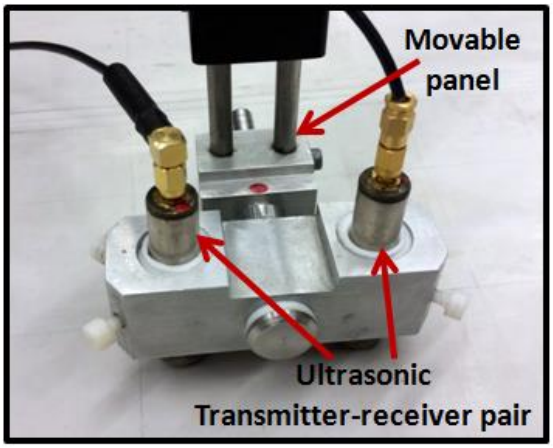

(a)

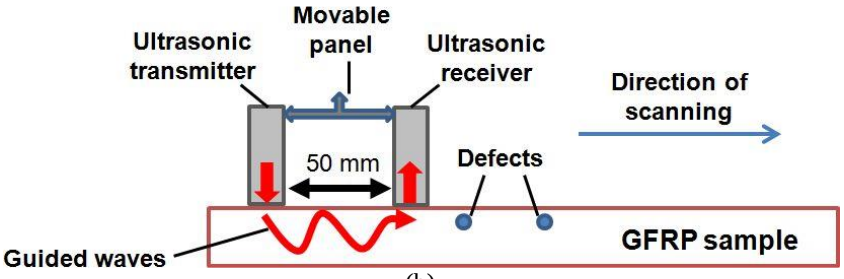

(b)

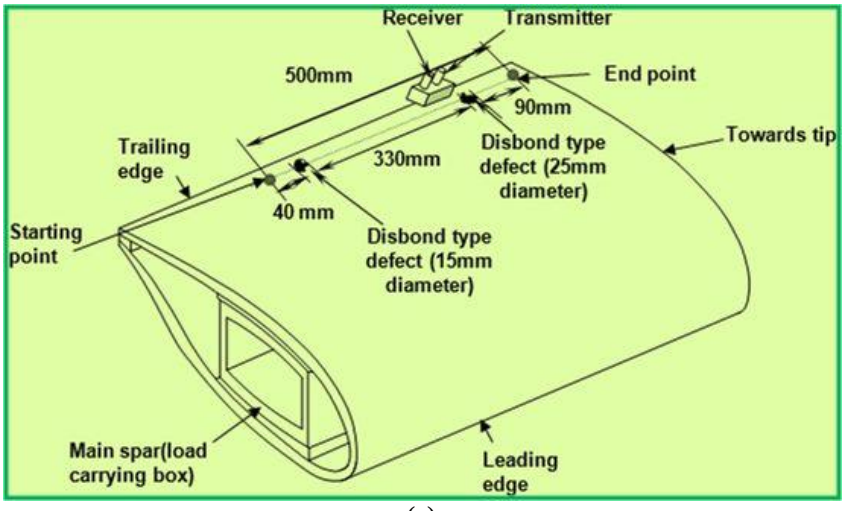

(c)

Fig. 2.6. Experimental investigation for the estimation of defects: photo of two transducers mounted on a moving panel (a); a schematic showing the basic principle of operation using transducer-pair (b); schematic of complete experimental analysis of a sample with the location of defects (c) (49).

Both transducers were kept 50 mm apart which was selected to ensure the significant resolution in the transmission/reception of GWs. Moreover, this distance was approximately equal to a multiple of some A_0 wavelengths (53, 54, 55). The scanning was performed in a pitch-catch mode. The basic configuration of the transducer-pair is presented in Fig. 2.6b. A schematic of the complete scanning process with the defects located on the trailing edge of the GFRP sample is shown in Fig. 2.6c.

The experimental scanning process and other details are described as follows:

- The sample was 6 mm thick in the defect-free region. The distance of the defective regions from the surface was 2.5 mm. It should be noted that scanning was performed on the opposite side of the sample. Therefore, the visualization of defects was not possible during the experimental analysis. A 150 kHz, 3-period burst signal was used to excite the transmitting transducer and a total of 500 signals were recorded by the receiver each at 1 mm up to 500 mm.
- Glycerol was used as a coupling between object and transducers.
- The received signal is averaged eight times to increase the signal-to-noise ratio (SNR) and the sampling frequency was 100 MHz.
- Moreover, the amplitude-based estimations are very sensitive to noise and variations of the environmental conditions. Therefore an ambient temperature of 25°C was maintained during the experiments.
- The B-scan image is acquired and shown in Fig. 2.7.
- It should be noted that the defect was not visually visible during the experiment. However, the transducer panel was set-up by knowing the position of defect because the defect estimation by linear scanning (B-scan) cannot be performed until the transducers do not scan over the defective regions. But this experimental technique is still valid for two-dimensional scanning (C-scan) without knowing the exact location of the defect.

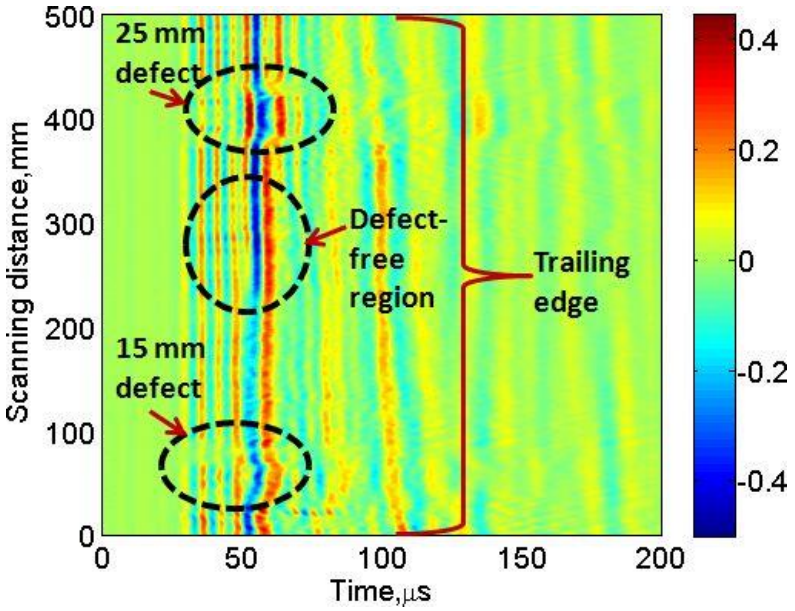

Fig. 2.7. B-scan image after scanning over the defects (53).

The significant changes in the waveform in the defective regions can be clearly observed in Fig. 2.7 which confirms the possibility of defects. However, the estimation and characterization of these defects from a single B-scan is not possible without post-processing the signals (53, 54, 55).

2.3 Signal processing

2.3.1 Wavelet de-noising and defect-estimations

The application of DWT for de-noising nonstationary and structural noise from GWs requires to select an appropriate wavelet family and its level and the thresholding method to discard the wavelet coefficients. There is no certain rule for selecting the appropriate wavelet family and it depends on the specific application and the characteristics of the GWs.

We are using point-type contact transducers which are working in thickness mode. They are more sensitive to amplitude variations of the GWs according to thickness of the structure. Hence, the wavelet family which is most energy preserving in nature could be an option. It is already explained in Chapter 1.6 that Daubechies wavelet is the most energy preserving and the simplest among the wavelet families. Therefore, first we select the appropriate level of Daubechies wavelet and then compare the appropriate Daubechies level with other wavelet families to select the most suitable. The soft and hard thresholding with a universal threshold is used to discard the wavelet coefficients as described in Chapter 1.6.

The order of Daubechies wavelet suitable for DWT is estimated by comparing the correlation coefficients of the widely used Daubechies levels (db4, db8 and db16)

(121). Three A-scan signals, each in the defect-free (average in the spatial range of 150–300 mm), 15 mm (average in the spatial range of 50–60 mm) and 25 mm (average in the spatial range of 400–410 mm) defective regions are selected and decomposed into 8 levels by using db4, db8 and db16 Daubechies levels. The detailed signal at the 8^{th} level (wavelet-de-noised) from db4, db8 and db16 levels are compared with the original signals in the case of defect-free and defective signals as shown in Fig. 2.8. The db16 level shows the highest correlation in each of the three cases (defective and defect-free signals).

In the next step, the conformity of selecting db16 Daubechies is performed by comparing it with the levels of other wavelet families. The A-scan signal in a 25 mm defective region (average in the spatial range of 400–410 mm) is considered for the comparison. The correlation coefficient of Daubechies (db16), Symlets (sym2, sym4 and sym8) and Coiflets (coif 2, coif4 and coif5) with their original signal counterpart are presented in Fig. 2.9. It is observed that db16 has the maximum correlation (0.83) with the original signal as compared to the levels of Symlets and Coiflets. Therefore, the db16 is selected for de-noising the experimental B-scan using DWT.

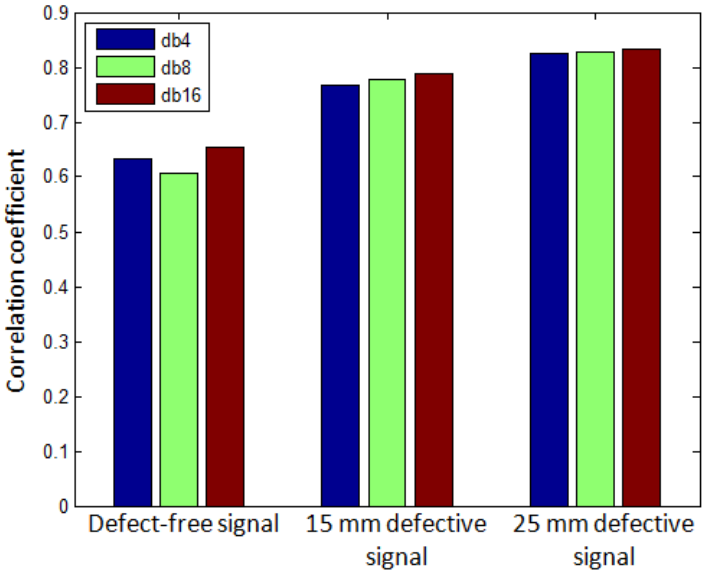

Fig. 2.8. Comparative correlations between Daubechies wavelet levels db4, db8 and db16 (53).

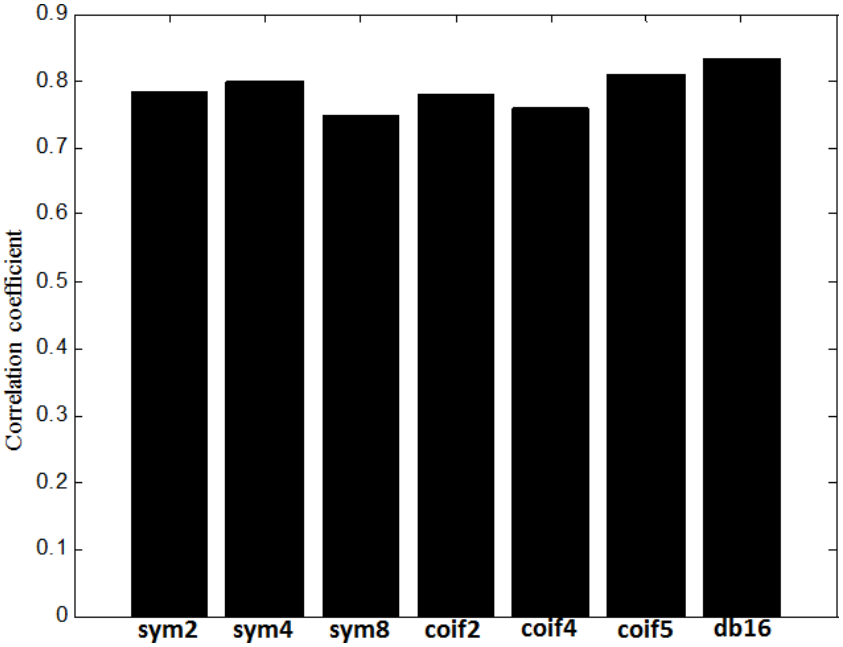

Fig. 2.9. Comparative correlations among db16, sym2, sym4, sym8, coif2, coif4 and coif5.

The process of signal de-noising and defect estimation using DWT is presented in Fig. 2.10 and described as follows (53):

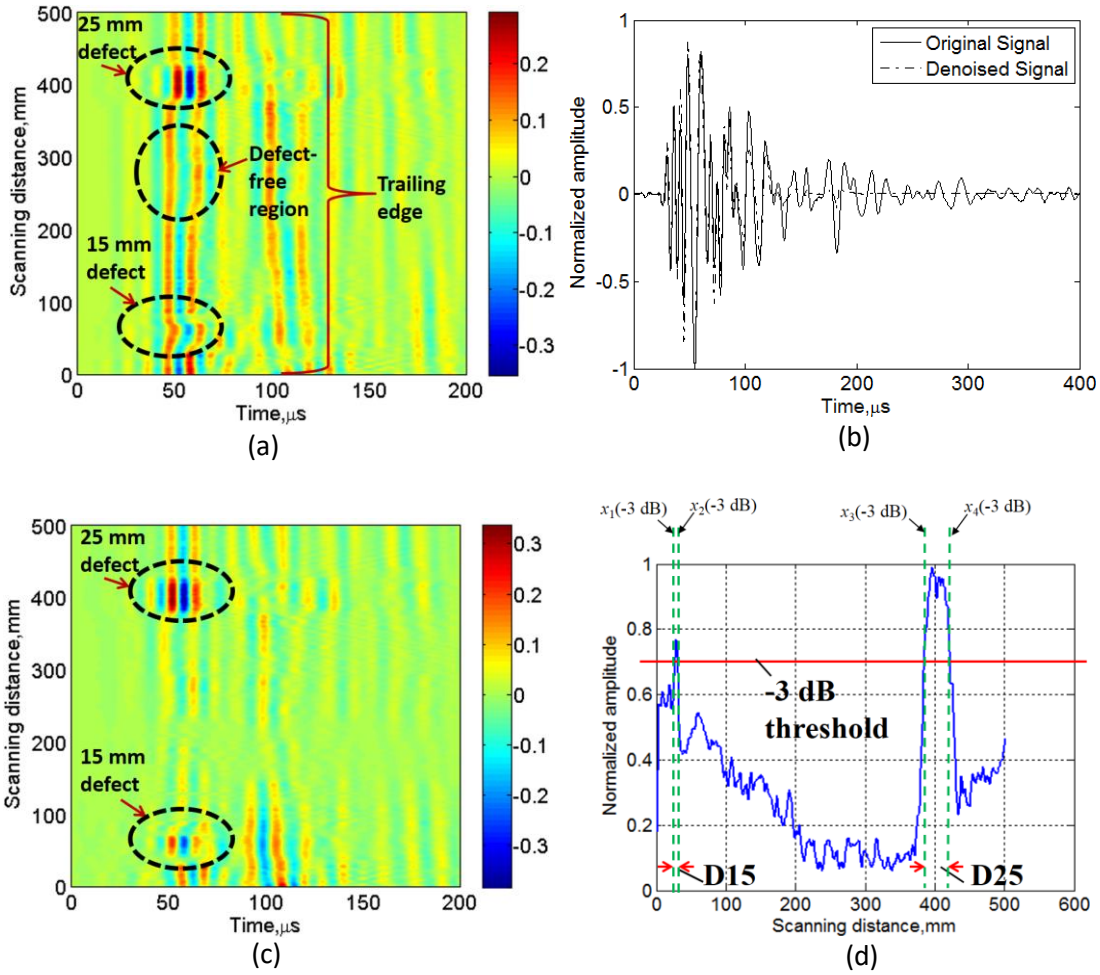

Fig. 2.10. Defect estimation after wavelet de-noising: Wavelet de-noised B-scan (a); A-scan at 50 mm scanned distance before and after de-noising (b); Modified B-scan after subtracting reference signal from each A-scan of de-noised B-scan (c); Amplitude detection for the estimation of size and location of defects (d) (49).

- DWT with db16 Daubechies wavelet is applied to decompose all A-scans of B-scan into 8 levels. The 8th level detailed signal contained minimum noise. Hence, the de-noised B-scan is obtained after considering the detailed signals at 8th level from each A-scan. The de-noised B-scan after DWT is shown in Fig. 2.8a.

- In order to properly visualize the de-noising process, the normalized A-scans in the 15 mm defective region at 50 mm scanned distance from the initial (first) scanned point are presented before and after de-noising (Fig. 2.10b).
- A reference signal in the defect-free region ($A_{1,\,ref}$) is then obtained by averaging the signals in the spatial range of (150–300 mm) in the defect-free region.
- The reference signal ($A_{1,\,ref}$) is subtracted from all A-scans of the B-scan. The modified de-noised B-scan is presented in Fig. 2.10c. It can be expressed as:

$$x_N(t,s) = x(t,s) - A_{1,ref}(t) \tag{2.1}$$

where $x\,(t,\,s)$ is the s^{th} A-scan signal from the de-noised B-scan (Fig. 2.10a), $x_N\,(t,\,s)$ is the new A-scan signal after subtracting $A_{1,\,ref}$ from it, and s is the scanned distance ($0 \leq s \leq 500$).

- Normalized peak-to-peak amplitudes of each A-scan from the modified de-noised B-scan (Fig. 2.10c) are calculated and plotted along the scanned distance as shown in Fig 2.10d. It can be expressed as follows:

$$A_{pp}(s) = \max[x_N(t,s)] - \min[x_N(t,s)] \tag{2.2}$$

$$A_{npp}(s) = \frac{A_{pp}(s)}{\max[A_{pp}(s)]} \tag{2.3}$$

where $A_{pp}\,(s)$ and $A_{npp}\,(s)$ are the peak-to-peak and normalized peak-to-peak amplitudes of the s^{th} A-scan signal from the de-noised B-scan.

- After applying a threshold of -3 dB level, the size and location of defects are estimated. If x_1, x_2, x_3 and x_4 are -3 dB points on the normalized amplitudes along the scanned distance (Fig. 2.10d), the location (distance from first scanned point) and the size of 15 and 25 mm defects can be calculated as:

$$\left.\begin{array}{l} Location\ of\ 15\ mm\ defect = x_1 \\ Size\ of\ 15\ mm\ defect = x_2 - x_1 \\ Location\ of\ 25\ mm\ defect = x_3 \\ Size\ of\ 25\ mm\ defect = x_4 - x_3 \end{array}\right\} \tag{2.4}$$

- The size of 15 and 25 mm defects was observed as 9 mm and 34.5 mm, respectively, with the respective absolute errors of 6 and 9.5 mm.
- The location of 15 and 25 mm defect from the starting scanned point was observed as 22.5 mm and 393 mm, respectively, with the respective absolute errors of 13.5 and 8 mm.

- The error also depends on the limitation of the optimal distance of 50 mm between the two transducers with other factors such as operating temperature, selection of threshold level in amplitude detection, wave dispersive characteristics, etc.

There are some limitations associated with the proposed technique. (i) Only a single B-scan is used for the estimation and characterization of defects. Hence, the accuracy depends on the interaction of the scanning transducer to the center of the defect. (ii) The experiment was performed by using a pair of contact transducers fixed on a mechanical unit. Since 50 mm was selected as the optimal distance between the transducers, the accuracy to locate or size the smaller sized defects (size <50 mm) can be affected. Hence, the estimation of 25 mm defect showed a higher accuracy than the 15 mm defect. The results can be improved by altering the optimal distance. (iii) The reproducibility of the results depends on the variations of signal amplitudes in the defect-free and defective regions. (iv) The accuracy also depends on the selection of -3dB threshold or peak-to-peak values of amplitudes. (v) The linear scanning (B-scan) used in experiments can be used to monitor and analyze larger defects (Diameter of defect > wavelength of propagating wave). The estimation and detection of smaller defects or microcracks can be possible only with non-linear ultrasonic scanning methods such as peridynamic theory (180, 181, 182). Due to variable size and the complexity of multi-layered composite materials, the standards are not yet set for the estimation of size and location of defects in the testing of WTB. However, as discussed in the introduction of this dissertation, contact-type testing of WTB at research and commercial levels are basically performed by using ultrasonic pulse-echo and phased array technique. Hence this technique would definitely motivate researchers to adapt the flexible and cost-effective pitch-catch approach in order to investigate multi-layered composite structures with complex geometries.

2.3.2 Application of cross-correlation

The cross-correlation on wavelet-denoised B-scan (presented in Fig. 2.10a) was applied in order to compare the defect-free reference signal to all A-scans of B-scan. The reference signal ($A_{2,\,ref}$) is selected by applying a time window (20–70 μs) and a spatial window (150–300 mm). The time window is considered in such a way that maximum possible interaction of GWs with the defective regions is covered. It should be noted that all A-scan signals were windowed in (20–70 μs) for the application of cross-correlation. The reference signal $A_{2,\,ref}$ is compared with each A-scan along the scanned distance of 500 mm as shown in Fig. 2.11a. The detection of defects was possible after applying -3 dB decision threshold. Due to the reduced thickness in defective region of composites, the phase velocity of GWs remains lower as compared to the defect-free region. Hence, the time-of-arrival of the dominant GW mode (A_0 in our case), in the defect-free region is shorter as compared to the region of defects. In order to estimate the time delay between the reference and other signals, cross-correlation with zero-crossing is utilized (Fig. 2.11b). The measured delay in time

between the reference signal $A_{2,\,ref}$ to all 15 and 25 mm defective signals was 1.75 and 3 μs, respectively (53).

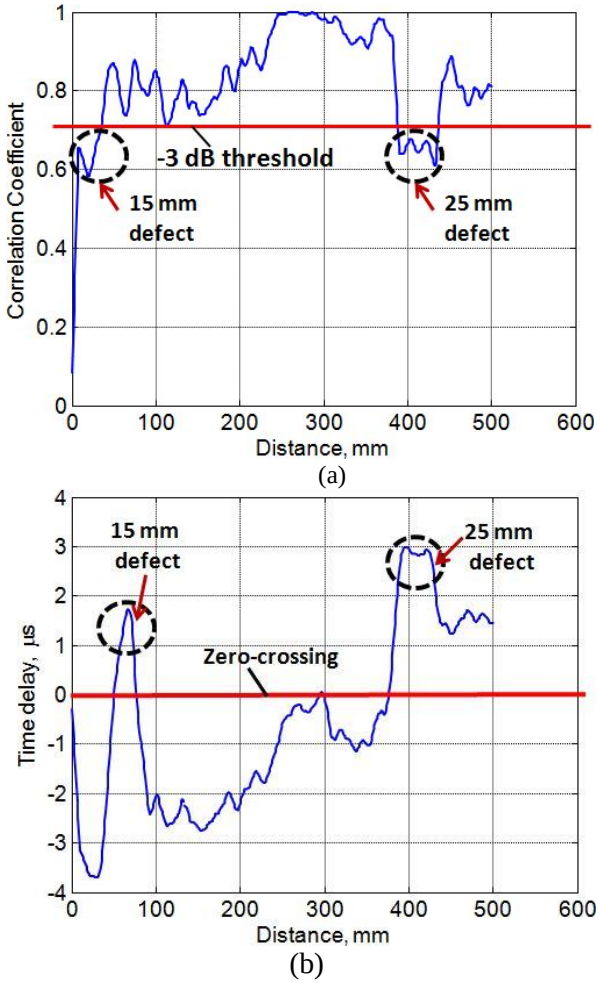

Fig. 2.11. Cross-correlation on a de-noised B-scan: Comparing correlation coefficients (a); Time-delay measurement (b) (49).

2.3.3 GW characteristics (instantaneous characteristics) by Hilbert Huang transform

The instantaneous characteristics of the GW signals (A-scans) in the defective and defect-free regions are estimated by using HHT (EEMD and HT). Detailed descriptions of HHT, HT and EEMD have already been discussed (Chapter 1.6 for details). Three A-scans each in defect-free and defective regions are obtained by

applying appropriate spatial windows, as illustrated in Section 2.3.1. These A-scan signals are denoted by $A_{1,\,ref}$, A_{15} and A_{25} for the defect-free, 15 mm and 25 mm defective regions, respectively. The procedure is described below (53):

- In the first step of HHT, each A-scan ($A_{1,\,ref}$, A_{15} and A_{25}) is decomposed into 14 IMFs by using the EEMD decomposition process. The ensemble size and noise standard deviation were selected as 500 and 0.2, respectively. The high-frequency components containing a significant amount of noise were clearly observed in the first five IMFs (IMF1 to IMF5) in all three cases. Therefore, only the IMFs from IMF6 to IMF14 were considered for the processing. The original A-scans and their decomposed IMFs (only IMF6–14) are shown in Fig. 2.12.
- The power spectral densities of each IMF from IMF6–14 were estimated in all three cases. The power spectral densities of the original A-scans were found closer to that of IMF6–9 and therefore added to reconstruct the new signals. The instantaneous frequency with respect to time of the reconstructed signal is shown in Fig. 2.13 as described in Chapter 2.2.4. The noise-free or response region can be clearly observed in Fig. 2.13. The oscillations are around the mean frequency (150 kHz) equivalent to the

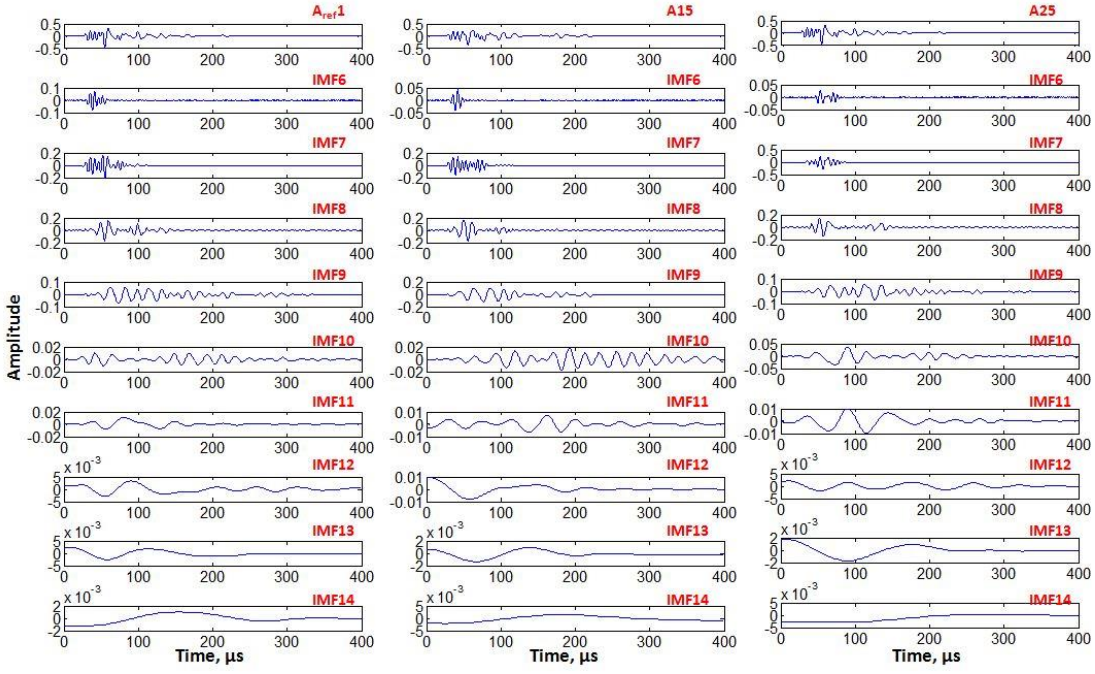

Fig. 2.12. EEMD decomposition: showing IMF6–14 of selective A-scan in the defect-free region (a), region of 15 mm defect(b) and region of 25 mm defect (c) (49).

excitation frequency. However, the oscillations achieve higher peaks in the case of defective signals compared to the defect-free (53).

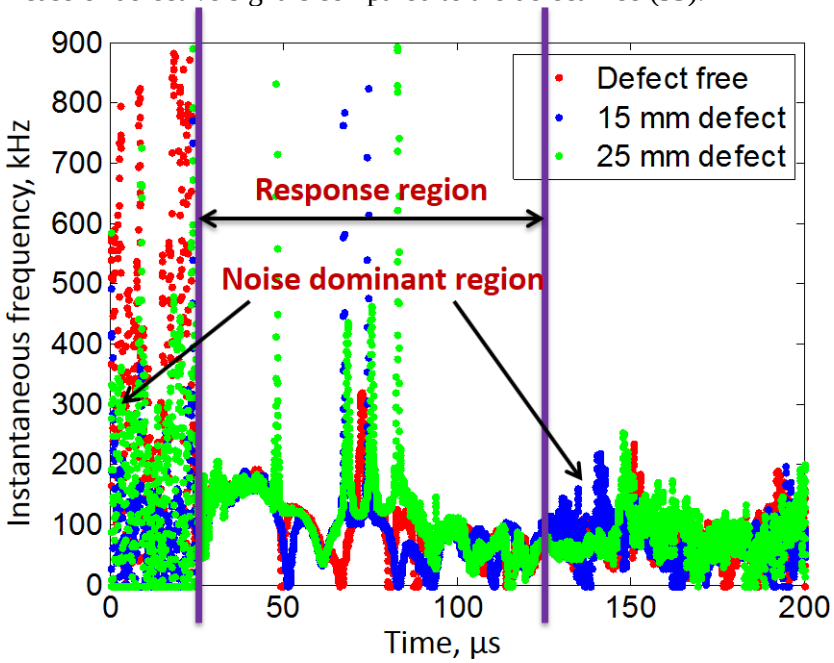

Fig. 2.13. Time-frequency characteristics of reconstructed signal (IMF6–9) after EEMD decomposition in each case (defect-free, 15 mm defective and 25 mm defective region) (53).

- The time-frequency characteristics provided no information about the signal intensities/energy variation in the defect-free and defective regions. Out of IMF6–9, the maximum power spectral density was contained in IMF6 and thus, was used to obtain instantaneous amplitude characteristics and the HHT spectrum of the signals in the defect-free and defective regions. The HHT spectrum is shown in Fig. 2.14a in the time range of 0 to 70 μs. This time-range covers the most interactive time range of 20 to 70 μs in which GWs interact in a more comprehensive manner with the defective regions. Fig. 2.14a shows that the time-span of the signals in the defective regions is longer as compared to the signal in the defect-free region. Moreover, the time-span of the noisy region is lower in the case of defect-free signals (30.65 μs) in comparison to the signals in 15 mm defective region (33.84 μs) and 25 mm defective region (45.30 μs) (53).
- The variation in normalized instantaneous amplitudes of defective and defect-free signals with respect to time is calculated by utilizing eq. (2.2) and eq. (2.3) and is presented in Fig. 2.14b. After applying a -3 dB of decision threshold, the time delays between the signals in defect-free and defective regions are calculated. If t_1, t_2 and t_3 are the -3 dB points as shown in Fig.

2.14b, the time delays of the 15 mm (t_d1) and 25 mm (t_d2) defective signals with respect to the defect-free signal can be estimated as follows:

$$t_d1 = t_2 - t_1 \tag{2.5}$$

$$t_d2 = t_3 - t_1 \tag{2.6}$$

- The estimated time delay in the case of 15 mm defective region is shorter (2.5 μs) in comparison to the signal in the 25 mm defective region (15 μs).

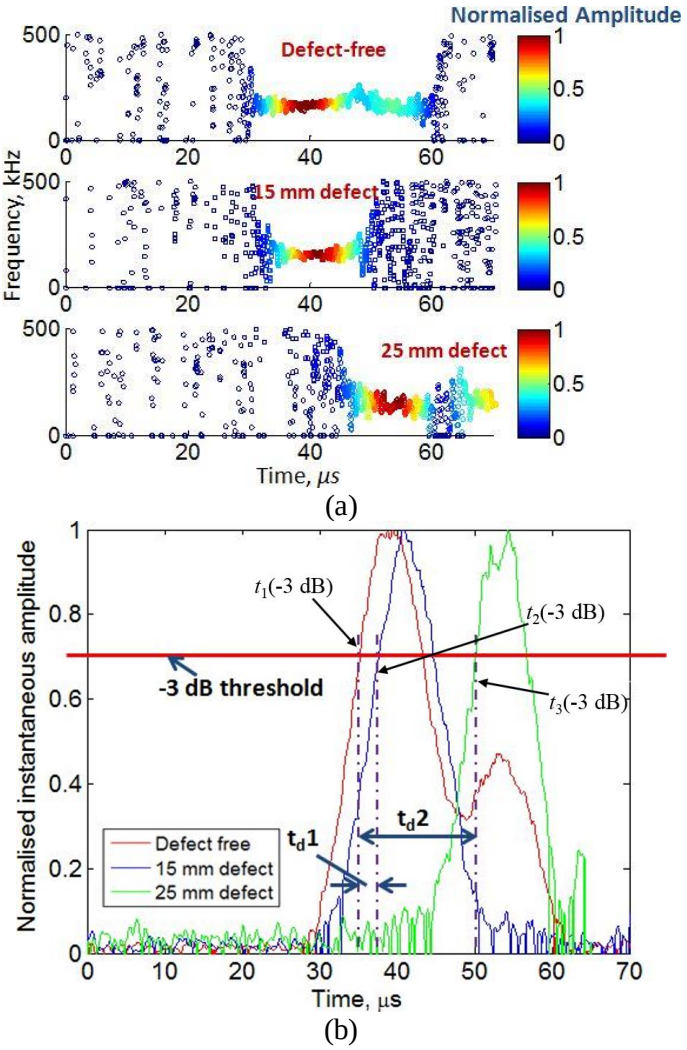

Fig. 2.14. HHT spectrum of the signals (IMF6) (a) and their normalized amplitude variation with respect to time (b) in the defect-free and defective regions (53).

The short-wave GW testing by using a pair of contact transducers operating in a pitch-catch mode presented in this Chapter is an efficient technique for testing composite structures. However, it is limited to the optimal distance between the transmitting and receiving transducers. Moreover, the continual monitoring of the composite structures and cover up the large region, the transmitter must be fixed or embedded at a desired location on the structure to form a measurement technique based on long-distance GWs. In order to proceed with long-distance GW testing, it is essential to effectively generate the transducer. Therefore, the displacement characteristics of a glued/ embedded transducer and its directivity characteristics must be known before its application in long-distance GW testing. MFC transducers are widely used with large structures by embedding due to their small size and weight and good actuators and sensors of the GWs. The following chapters present the three-dimensional displacement characteristics and development of an analytical model to predict the directivity characteristics of a transducer (MFC transducer) and later on the measurement technique based on long-distance GW testing (using an MFC transducer as a transmitter and a contact-type receiver) is developed.

2.4 Conclusions

The detailed conclusions along with the limitations and issues associated with the proposed techniques are:

1. The measurement technique based on short-distance guided waves by using a special configuration of two contact-type transducers fixed on a moving panel and operating in pitch-catch mode is proposed to estimate the disbond-type defects in small composite structures possessing an aerodynamic shape and complex geometries. Moreover, the signal processing techniques by combining the positive features of DWT, amplitude detection and HHT are also described for the estimation of size and location of defects, as well as the estimation of instantaneous characteristics of the GWs in the defect-free and defective regions.
2. The disbond type defects of 15 and 25 mm in diameters have been successfully detected. The size and positioning of the defects are also estimated. However, the technique is limited by the optimal distance between the transducers, the size of defects (defect must be greater than the operating wavelength) and the thickness of the layered structure.
3. In comparison to the current contact-based ultrasonic NDT techniques (*e.g.* ultrasonic pulse-echo and phased-array technique) used for structures possessing an aerodynamic shape and complex geometries (*e.g.* aircraft wings and WTB), the novel features of the proposed technique are its flexibility in terms of locating the transducers as compared to the ultrasonic pulse-echo, less complexity and cost-effectiveness in comparison to the ultrasonic phased-array technique in terms of number and configuration of transducers.

4. Other novel features in the proposed measurement technique and signal processing techniques can be summarized as follows: (i) The fixed distance between the contact-type transducers assure the reduction in attenuation and dispersion losses that could be produced due to the variable distance between transducers. (ii) Using the transducers operating in thickness mode and more sensitive to the *out-of-plane* radiations facilitates the application of simple amplitude detection techniques on the received guided wave signals to distinguish between the defect-free and defective regions. (iii) The selection of appropriate mother-level based on the correlation between the original signal to only the highest detailed level signal is proposed which reduces a significant amount of computation time.

3. THREE-DIMENSIONAL DISPLACEMENT CHARACTERISTICS AND DIRECTIVITY PATTERN OF P1-TYPE MFC TRANSDUCER

3.1 Demand and motivation

The transducer which can be glued/embedded (*e.g.* MFC transducers) within large composite structures plays a vital role in long-distance GW testing and SHM of the structures as explained in Chapter 1.4.2. However, the effective generation depends on the location of the transducer to cover the region of interest, the knowledge of propagating GW modes by using a transducer for different frequency of excitation and type of propagation medium. Therefore, it demands the following estimations:

- Calculation of 3D displacement characteristics of a transducer: by estimating the 3D displacement characteristics of a transducer, the dominant wave components can be obtained which could provide additional information to increase the accuracy of inspection method. Moreover, after comparing the 3D characteristics with the manufacturer data sheet, the defective and faulty transducers can be omitted from real-time applications (48). In the LF ultrasonic, three displacement components *i.e.* A_0, S_0 and SH_0 of ultrasonic GW are widely used to inspect structures depending on the type of transducer, excitation frequency and sample. In this chapter, P1-type MFC transducer (48, 103) has been considered to obtain the 3D spatial displacement components of the propagating wave. The description and characteristics of the P1-type MFC transducer have already been introduced in Section 1.4.2.
- The knowledge of directivity characteristics of a transducer or array of transducers can increase the accuracy of inspection of large and complex structures in different ways. It can facilitate the NDT engineer to decide the exact location where the transducer must be embedded/glued on the object under investigation, to decide the excitation frequency of a transducer for the propagation of the desired wave mode (e.g., the A_0, S_0 or SH_0 in LF ultrasonic) or to optimally select the appropriate configuration of transducers (49, 50). Analytical modelling is a fast and effective approach in comparison to numerical modelling and experimental approach which can be used to estimate transducer directivity in any propagation medium.

The objective of this Chapter is to investigate three-dimensional spatial characteristics of P1-type MFC transducer with an active dimension (28 x 14 mm) and its possible application for testing and structural health monitoring of composite structures using ultrasonic GWs. Another objective of this Chapter is to develop and validate an effective 2D analytical modelling for the estimation of directivity of any contact-type ultrasonic transducer or configuration of transducers at any excitation frequency by knowing the behavior of a transducer and dispersive characteristics of the propagating medium The P1-type MFC transducer is considered for the demonstration of the 2D model. The organization of this Chapter is as follows:

- Firstly, to estimate the resonant frequency, phase and impedance characteristics of unloaded P1-type MFC transducer.
- Secondly, to measure the 3D spatial displacement characteristics of unloaded P1-type MFC transducer by using the Polytec 3D laser vibrometer. The *in-plane* and *out-of-plane* displacement characteristics along the length and along the width of MFC are plotted and compared. The applicability of P1-type MFC transducer in ultrasonic NDT and SHM of composite structures based on displacement characteristics is also discussed.
- The 2D analytical model is developed to predict the directivity pattern of contact-type ultrasonic transducers and demonstrated by P1-type MFC transducer glued on Al alloy plate at two different excitation frequencies (80 kHz, 5 periods and 220 kHz, 5 periods). Finite element (FE) analysis is performed to verify the results of the directivity patterns of A_0, S_0 and SH_0 waves. The experimental investigation with special scanning by LF ultrasonic system developed at Kaunas University of Technology is performed for further validation of results (for A_0 wave).
- After validating the 2D model, the directivity pattern at the resonant frequency (43 kHz) of MFC transducer in Al and composite structure (GFRP) is estimated.
- Finally, the conclusions of the Chapter are presented.

3.2 P1-Type MFC transducer

Due to its small size, light weight, flat geometry, ability to work in actuation, transmission and sensing mode, the macro fiber composite (MFC) transducer is one of the best transducers (48, 103, 105, 114) for non-destructive testing (NDT) and structure health monitoring (SHM) of composite structures. Guided Lamb waves (the A_0 and S_0) can be effectively transmitted and received by using an MFC transducer (105). The S_0 (in the direction of wave propagation) mode is mainly distributed *in-plane* and the A_0 mode contains dominant *out-of-plane* components of the propagating waves. As P1-type MFC operates in elongation mode (the d33), the S_0 mode is the most dominant.

The inspection using MFC transducer can be easily combined with different contact and non-contact ultrasonic inspection methods for NDT and SHM of composite structures (7, 55). The MFC transducers can be easily glued or embedded within large and complex structures without damaging the surface (50). In aerospace applications, the embedded MFCs are frequently used for generating and harvesting ultrasonic wave energy, SHM of a structure and detecting defects and damages due to impact (48, 183). MFCs have the ability to control the twisting motion of aircraft wings as well as the airfoils' aerodynamic shaping (184, 185). Hence, it can increase the efficiency of an aircraft by improving its aerodynamic performance.

In comparison to active fiber composite (AFC), MFC has a high fiber volume fraction which ensures its high stiffness and performance. Moreover, MFCs have

better actuation performance compared to the most common piezoceramic actuators (48, 184, 185). Embedded MFCs can be used to detect defects or damages in large and composite structures which were verified by analyzing the composite structure of A320 wing tested by embedding 10 MFC transducers. The developed system was based on the transmission and detection of ultrasonic signals, using technology which can not only transmit ultrasonic waves and harvest the energy of vibrations, but also successfully detects impact-type damages (183).

MFC transducers (both actuator and sensor) were also used in the non-contact ultrasonic system with a laser transmitter and air-coupled sensors for analyzing the adhesively bonded joints of the skin-to-spar structure of the composite wing (186). MFC has also been used for testing the honeycomb sandwich structures, which are widely used in aerospace and transport industries, as well as in a sector of structural integrity testing of large engineering constructions. Although, conventional C-scan and radiography based methods are widely used to analyze the honeycomb structures (187), the researcher has been working on effectively utilizing the MFC transducers to improve the ultrasonic system. The embedded ultrasonic system was developed to inspect complex composite structures using MFC as a transmitter bonded to the honeycomb sample and the contact-type receiver to detect large delaminations/disbonds (diameter of around 200 mm) (188). The MFC actuators can also be used for vibration control in honeycomb structures. The P1-type MFC transducer can be applied to simplify the honeycomb sandwich model into the finite plate model. In this way, the vibrating plate can be actively controlled by surface-bonded MFCs by reducing the vibroacoustic radiations (189).

Applying the rosette principle (three P2-MFCs operate as a rosette) and two rosette sensors possessing high directivity can also be used for locating wave sources in complex composite structures without knowing the velocities of propagating waves and without using complex modelling as compared to the time-of-flight method (190). The P1-MFC actuators based on bimorph configuration were successfully tested and implemented in aerodynamic pressure flow control in which eight P1-8557-MFCs were used to form the active surfaces. In addition, MFCs have also effectively contributed to aerodynamic shape control (191). MFC-P1-type actuators of 3 different sizes were successfully tested for the efficient wavelength tuning of Bragg reflector laser which can be used to avoid multi-laser sources for the applications of wavelength division multiplexing (WDM) (192).

In our research, MFC transducer of P1-type (M-2814-P1) with dimensions of 28 × 14 mm is used. The photo image of a P1-type MFC transducer is shown in Fig 3.1 (50). The general parametric characteristics of the MFC-2814-P1 transducer are presented in Table 3.1 (48).

Table 3.1. General characteristics of MFC-P1-M2814 (48)

Features	**Typical value**
Active dimension	28 mm x 14 mm
Overall dimension	38 mm x 20 mm
Operating voltage	-500 V to +1500 V
Capacitance	1.15 nF
Free strain	1550 ppm
Blocking force	195 N
Operating bandwidth as an actuator	0 Hz to 700 kHz
Operating bandwidth as a sensor	0 Hz to 1 MHz
Maximum operational tensile strain	< 4500 ppm
Linear-elastic tensile strain limit	1000 ppm

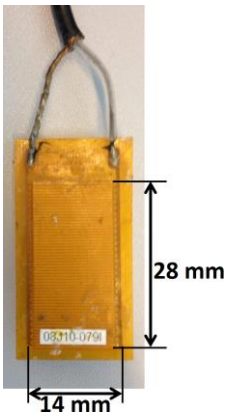

Fig. 3.1. A photo of P1-type MFC transducer with dimensions of 28 x 14 mm (45)

3.3 Impedance, phase characteristics and frequency response of P1-Type MFC

The MFC-P1-2814 (serial number: 08J10079l) manufactured by *Smart Materials* (48) was considered for the experimental analysis. In order to estimate the resonant frequency of the MFC transducer, the frequency response of the MFC should be known. The Wayne Kerr 6500B impedance analyzer was used to measure the phase and impedance characteristics of P1-type. Fig. 3.2 shows a schematic of the experiment.

The impedance and phase characteristics of the MFC transducer are presented in Fig. 3.3 from which the resonant and antiresonant frequencies can be obtained. The resonant and antiresonant frequencies were observed very close to each other as 41.38 kHz and 43.63 kHz, respectively (48). Moreover, the phase jump frequency of 42.58 kHz is also close to these frequencies. Hence, the excitation frequency of 43 kHz was selected to excite the MFC transducer for the analysis of 3D displacement using a Polytec 3D laser vibrometer.

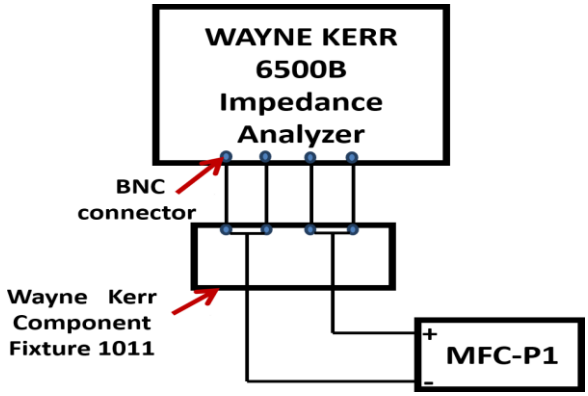

Fig. 3.2. A schematic showing the measurement of impedance and the characteristics of P1-type MFC transducer (MFC-P1-2814) using Wayne Kerr 6500B impedance analyzer (44).

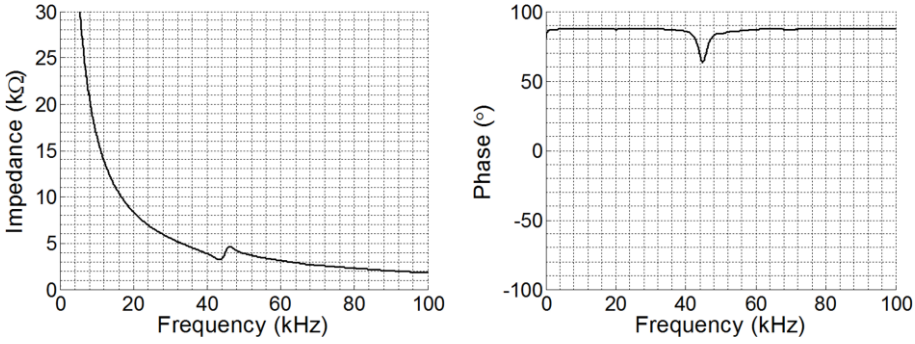

(a) (b)

Fig. 3.3. Impedance (a) and phase characteristics (b) of the P1-type MFC transducer (44).

In order to analyze the frequency response of the MFC transducer, the following steps have been performed:

Step 1: The MFC transducer was glued at the center of Aluminum (Al) alloy plate with dimension of 1000 × 1000 × 2 mm and excited with 220 kHz, 3-period excitation signal. The mechanical properties of the Al plate are presented in Table 3.2. The response $h_1(t)$ has been recorded with a contact-type transducer (see Chapter 2.2.1 for details) located at 100 mm along its longitudinal axis. The sampling frequency was 25 MHz. The response in frequency domain $H_1(f)$, is calculated as:

$$H_1(f) = FT(h_1(t)] \tag{3.1}$$

Step 2: Two contact-type transducers operating as a transmitter and receiver were used to record the response $h_2(t)$. The same parameters and medium (Al alloy plate) as described in step-1 were used. The frequency response in this case is given as:

$$H_2(f) = FT(h_2(t)] \tag{3.2}$$

Hence, the magnitude response $|H(f)|$ of P1-MFC in Al plate can be expressed as:

$$|H(F)| = \frac{|H_1(f)|}{\sqrt{H_2(f)|}} \tag{3.3}$$

These signals are plotted in Fig. 3.4a–e. The magnitude response $|H(f)|$ of the MFC transducer is shown in Fig. 3.4e. The $|H(f)|$ attains its maximum amplitude at 45 kHz frequency which is closer to the resonant frequency of the MFC transducer.

Table 3.2. Mechanical properties of Al-alloy plate (50)

Symbol	**Quantity**	**Numerical Value**
E	Modulus of elasticity	71 GPa
ρ	Density	2780 kg m^{-3}
υ	Poisson's ratio	0.33

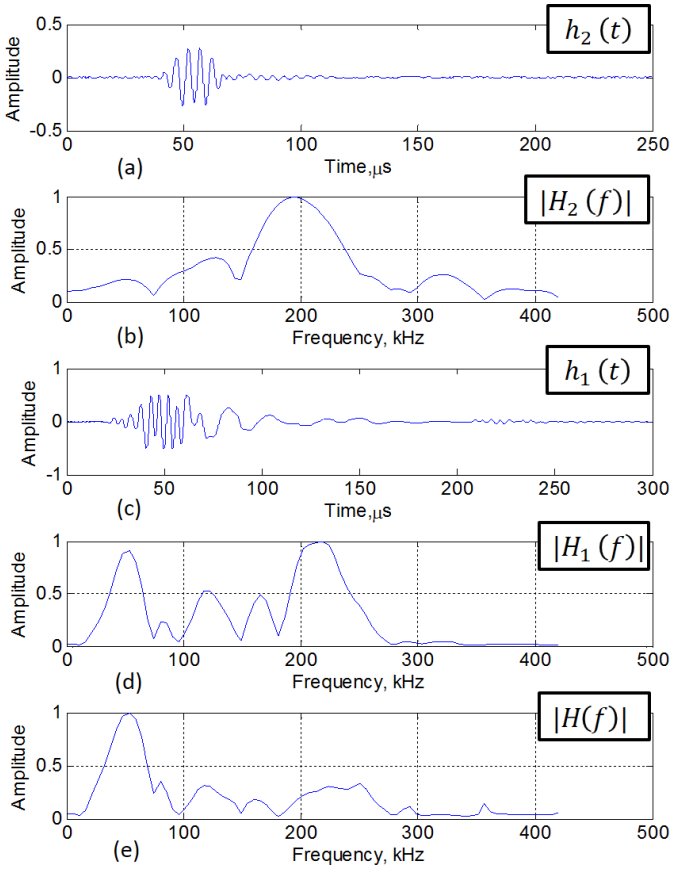

Fig. 3.4. Frequency response of MFC in Al plate: recorded A-scan signal and its respective magnitude response by using two contact-type transducers ((a), (b)) and by using MFC transducer with a contact-type transducer ((c) and (d)); Magnitude response of the MFC transducer (e)

3.4 Experimental investigation of P1-type MFC transducer by 3D laser vibrometer

In the next step, the 3D displacement (*in-plane* and *out of plane*) components of an unloaded and vibrating MFC-P1-2814 transducer at 43 kHz is measured with a 3D Polytec PSV-500-3D-HV scanning laser vibrometer. This experiment was performed to verify the dominant performance of spatial displacement of MFC along the length (d33 or elongation mode). The basic characteristics of Polytec PSV-500-3D-HV laser vibrometer are listed as follows (48):

- There are a total of three scanning heads in the vibrometer. The *top head* ((PSV-I-500) has very high precision and contains a geometry scan unit (PSV-G-500) and a full HD camera. The HD camera has the ability of 20x zoom for accurate and effective video triangulation, visualization and alignments (48).

- The other two heads are called Left/Right scanning heads which do not contain the geometry scan unit or an HD video camera.
- The decoder is used to decode the information of velocity from the HF Doppler signal feeding on the scanning head.
- Interfacing between the Front-end unit and scanning heads is provided by the Junction box (PSV-E-530).
- Finally, the data is supplied to a PC for further processing via an Ethernet interface.

The schematic of the experimental analysis of a free-vibrating MFC transducer is presented in Fig.3.5. Before proceeding with the experimental investigation, laser heads are aligned to the test sample (P1-type MFC) as well as to each other.

The positioning of laser beams on defined scan points on the surface of MFC is a two-way process (48).

- The 2D alignment is the first step which is also called standard alignment. A live video image is used for positioning the laser beam on scan points.
- The 3D alignment is the second step of this process. A 3D coordinate system is used to estimate the angles between the spatially scanned mirrors for a given point. It should be noted that PSV software itself provides corrections in the process so that all measurement points are covered by positioning the laser beam. This positioning is used for the experiment.

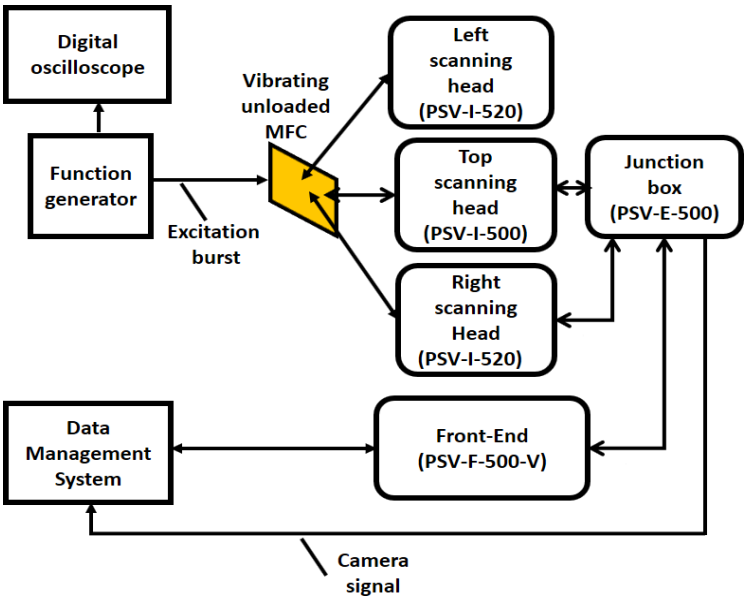

Fig. 3.5. A schematic of the experimental set-up for measuring the 3D displacementcomponents of P1-type MFC transducer using a 3D Polytec laser vibrometer (PSV-500-3D-HV) (44).

The accuracy of positioning the left, right and the top lasers was achieved as 0.2 mm, 0.2 mm and 0.1 mm, respectively. The 17 measurement points along the length of the MFC transducer with a step size of 1.75 mm were selected by the PSV software of the vibrometer. The same number of points along the width of the MFC transducer was selected with a step size of 0.875 mm. Therefore, the total number of measurement points along the structure of MFC was 289 (48). The 120 cycles of burst-type sinusoid signal of frequency 42 kHz and peak amplitude of 10 V is used to excite the MFC transducer. The received signals are recorded at a sampling frequency of 1.25 MHz(48). The accuracy of the results depends on the noise. Misalignment of laser heads and variations in operating temperature may cause error in the results. Therefore, 23ºC ambient temperature is maintained during the experiment and 64 signals are averaged before recording the signals.

Although a total of 289 points were scanned, the symmetry of the MFC structure facilitated to consider points along the two edges. Hence, 17 points on the edges (along the length and width) are considered to obtain the 3D displacement components of MFC. Fig. 3.6 shows the *in-plane* (*X*-component (along the width of MFC), *Y*-component (along the length of MFC)) and *out-of-plane* (*Z*-component) components of the propagating wave.

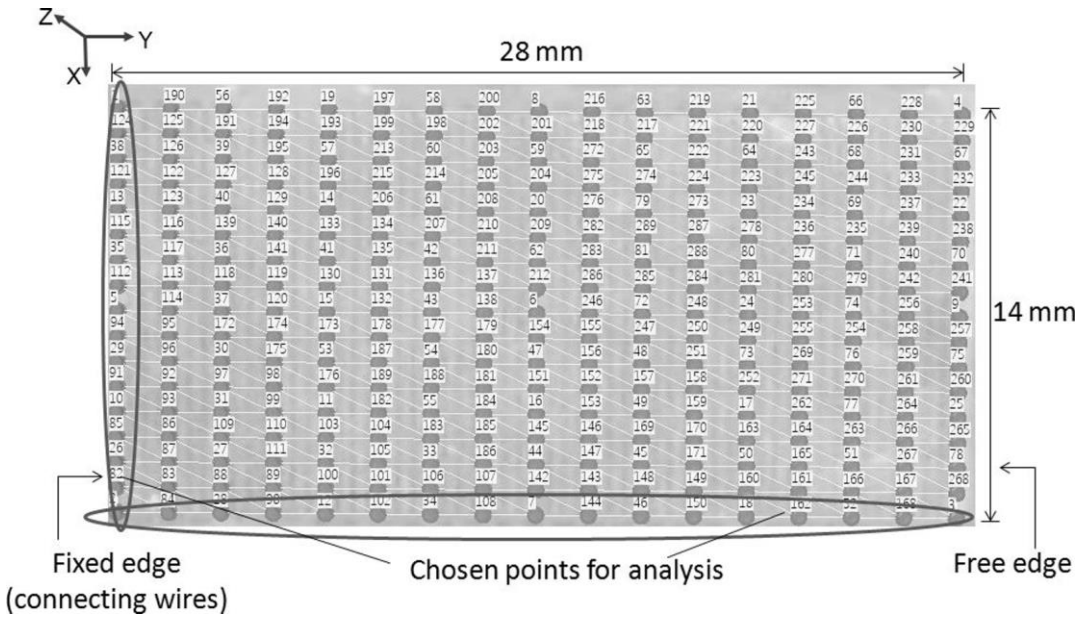

Fig. 3.6. The measurement points and chosen points along the edges of the MFC transducer for the analysis of 3D displacement characteristics (48).

3.4.1 Results and discussions

The maximum values of positive and negative 3D displacements are estimated in order to plot the *X*, *Y* and *Z* displacement characteristics along the length and width of MFC. The experiment was repeated three times and the variations in the results in each case were less than 1%. Fig. 3.7a–e shows the maximum positive and negative spatial displacements along the length and width of MFC.

The outcomes can be summarized as follows(48):

- Along the length of MFC, the variations in maximum Y-displacements (Fig. 3.7a) are the highest. On the other hand, variations in X-displacements (Fig. 3.7b) are the highest along the width among all three displacements.
- In comparison to the range of *X* displacement (-35 nm to +35 nm) and *Z*-displacement (-100 nm to +100 nm), *Y*-displacement range (-167 nm to +167 nm) is much higher (48). Hence, it confirms that P1-type MFC works in elongation or d33 mode and has dominant longitudinal displacements.
- The displacement profile of Z-displacement (which corresponds to the *out-of-plane* A0 mode) is similar to the Y-displacement profile but the amplitudes are much lower than that of Y-displacements. (Fig. 3.7e–f).

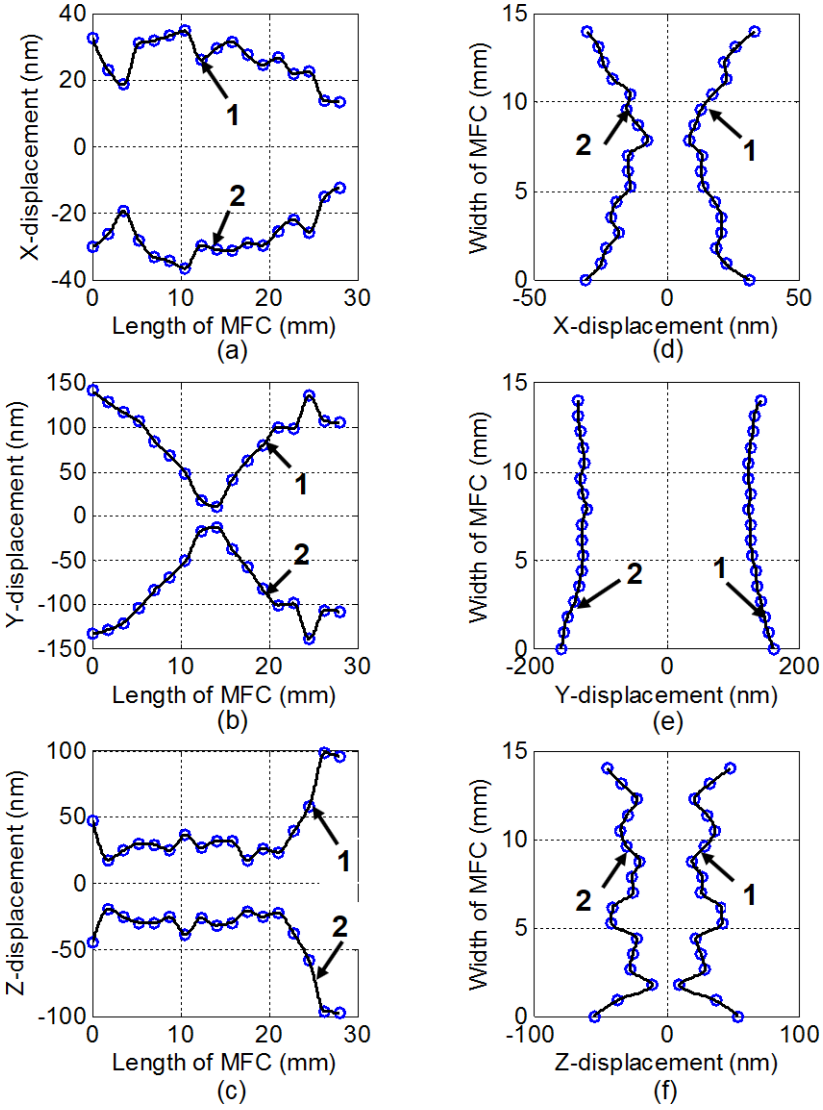

Fig. 3.7. Positive and negative 3D displacements (*X*, *Y* and *Z*) along the length and width of MFC: *X* displacements along the length (a) and along the width (d), *Y* displacements along the length (b) and along the width (e), *Z* displacements along the length (c) and along the width (f) (1- measured positive and 2- measured negative displacements) (44).

In LF ultrasonic, an MFC transducer can effectively generate and receive fundamental Lamb modes (the S_0 and A_0). The S_0 and A_0 waves contain the dominant wave components along the length and transverse (*out-of-plane*) directions, respectively (193). Hence, the performance of MFC transducer to generate and receive

the S_0 mode can be described by *in-plane* Y displacements (Fig. 3.7b, e). Similarly, the performance of MFC to generate and receive A_0 mode can be described by out-*of-plane Z* displacements (Fig. 3.7c, f). There is another type of non-dispersive guided wave mode in LF ultrasonic which is called the fundamental shear horizontal mode (SH_0) (114, 194). The dominant particle motion of SH_0 wave remains in in-plane and perpendicular to the S_0 wave. The performance of SH_0 mode is described by both X and Y displacement components (Fig. 3.7a, b, d, e) (50).

In order to compare the displacements at the center and corner of MFC transducer with respect to time, scanned points at the center (scanned point 6) and corner (scanned point 9) of the MFC transducer are selected (Fig. 3.8).

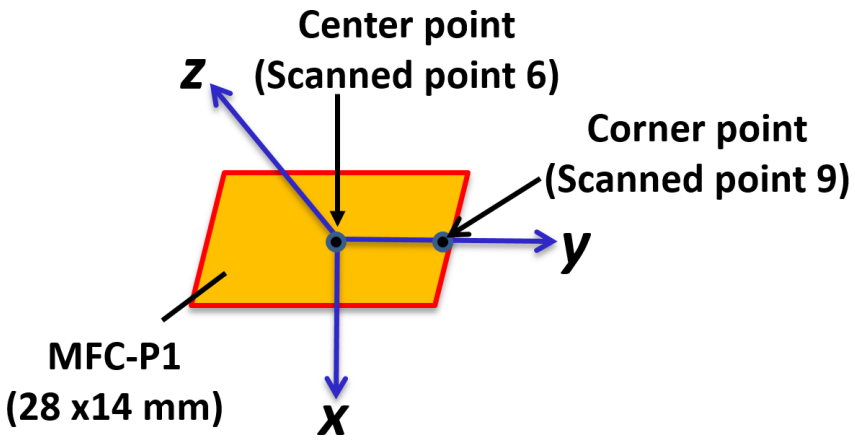

Fig. 3.8. Center (scanned point 6) and corner (scanned point 9) points of MFC transducer on its longitudinal axis (48).

The HT is applied to each of the three displacement components measured at the center and corner points in order to estimate their envelopes. The results are presented in Fig.3.9a-f. The time axis is selected to pick up the maximum displacements at each point.

The results (Fig.3.9a-f.) are described below (48).

- The *X*-displacements at both center (Fig. 3.9a) and corner (Fig. 3.89) points are minimum among all three displacement components. Moreover, there is no significant difference observed in the maximum X-displacements at center or corner point (range of 10 nm to12.2 nm). Hence the generation and reception of SH_0 wave by MFC transducers are not effective in ultrasonic NDT (48).
- After comparing the *Z*-displacement (Fig. 3.9b) and *Y*-displacement (Fig. 3.9c) at the center point of MFC transducer, it is clearly observed that maximum *Z*-displacement is slightly higher (the difference is 5.5 nm) as compared to the maximum *Y* displacement.

- The maximum Y-displacement (166.7 nm) at the corner point (Fig. 3.9e) is much higher than the maximum of *X* (12.3 nm) and *Z*-displacements (33.5 nm) at the corner points ((Fig. 3.9d) and (Fig.3.9f)). Moreover, a large increment in the value of maximum *Y*-displacement from 21.5 nm at the center to 166.7 nm at the corner point confirms its ability to receive and generate S_0 waves in a dominant manner.

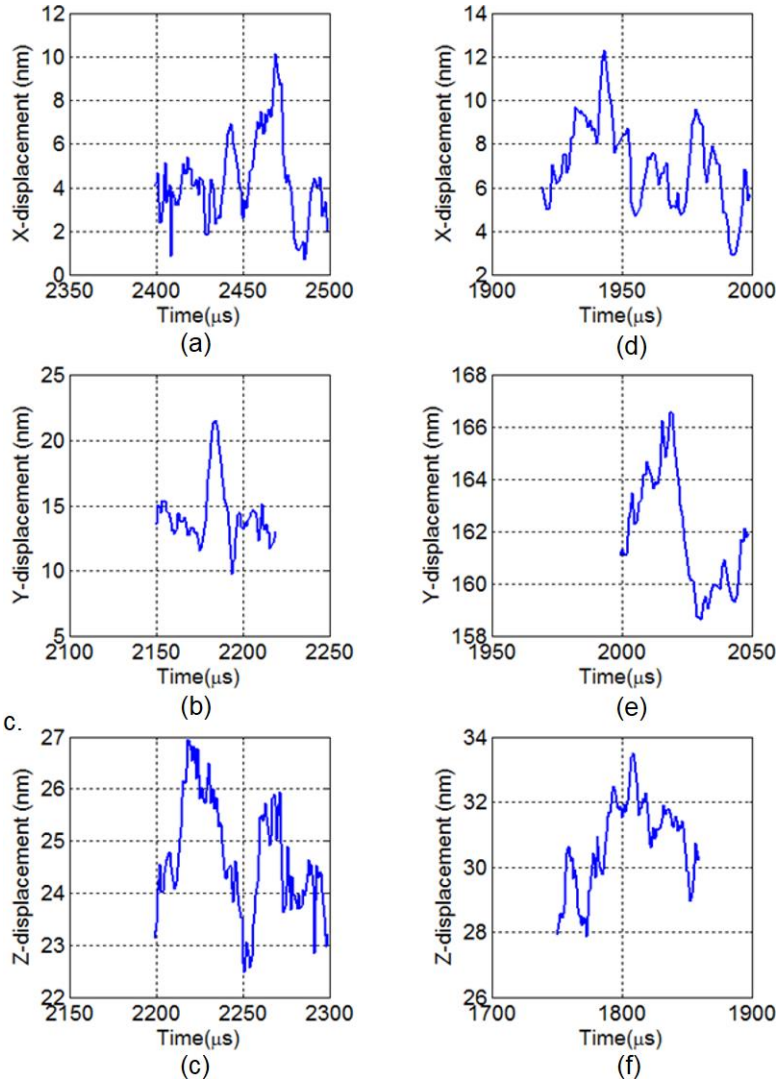

Fig. 3.9. The variations in *X*, *Y* and *Z* ((a),(b) and (c), respectively) displacements at the centre point; *X* , *Y* and *Z* ((d),(e) and (f), respectively) displacements at the corner point of MFC transducer with respect to time (44).

3.5 Two-dimensional analytical model for predicting the directivity of ultrasonic contact-type transducers

The 2D analytical model for predicting the directivity of ultrasonic contact-type transducers is developed on the basis of Huygens's principle of propagating waves (49, 50). Huygens's principle states that all points on a wavefront can be termed as point sources of wavelets traveling with the velocities of propagating wave modes (50, 195). The assumptions and the basic steps of the proposed 2D model are described as follows (50):

- The model is valid for a contact-type ultrasonic transducer of any shape and is considered as point sources distributed on a 2D surface. The 81 sensing elements are created by considering the arbitrary points spaced equally along the half-circle (0 to 180°). The distance between the sensing elements and the center of the transducer can be selected as per requirement.
- All distance vectors from all distributed point sources are integrated to each of the sensing elements.
- The transfer function is calculated by multiplying the attenuation and phase parts. The transfer function depends on the distance, phase velocity of the propagating wave and the frequency of excitation. It should be noted that a computational package *Disperse* (82) was used to compute the phase velocity to be included.
- The directivity of propagating wave modes S_0, A_0 or SH_0 also depends on the amplitude and direction of a specific propagating wave. Thus, a correction factor which depends on the amplitude and direction of propagating wave modes along the structure of the transducer is multiplied to the input signal. The calculation of correction factor is presented in Section 3.5.2. After including the correction factor, the spectrum (Fourier transform (*FT*)) of the input signal is called modified/corrected spectrum of the input signal.
- The diffraction in distances has been taken into account by including the diffraction factor.
- The output signal in the frequency domain is calculated by multiplying the corrected/modified spectrum of input signal, transfer function and the diffraction factor.
- The output signal in the time-domain is calculated by taking the inverse Fourier transform (FT^{-1}). Finally, the normalized peak-to-peak amplitudes of the output signal along the polar coordinates are plotted to obtain the directivity pattern of a particular propagating wave mode.

3.5.1 The formulation of a 2D analytical model for calculating the directivity of a transducer

The model is presented in Fig. 3.10 (49, 50). A rectangularly shaped transducer has been considered for the mathematical description of the proposed 2D model. However, the basic methodology behind this model depends entirely on the integration of distance vectors from point sources to the sensing point. The center of

the transducer is considered as the origin in a 2D coordinate system for the model (49, 50).

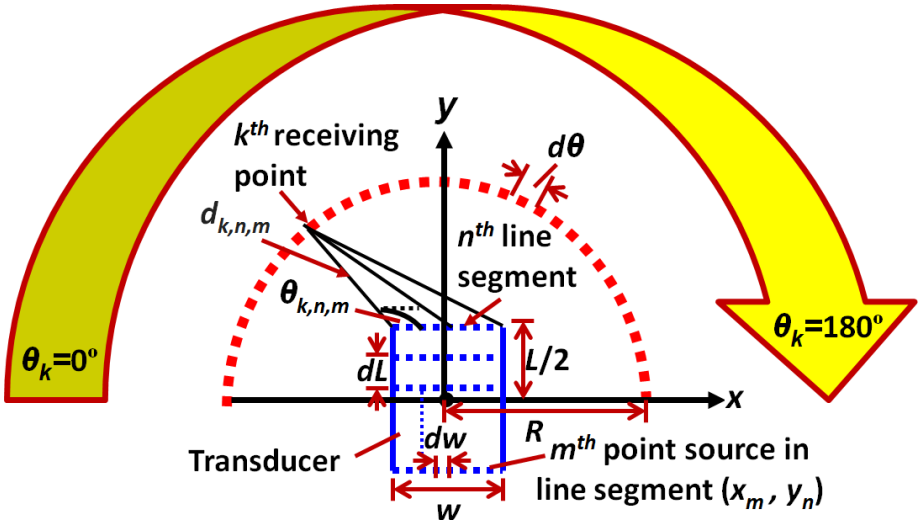

Fig.3.10. A schematic of the 2D analytical modelling for calculating the directivity of an ultrasonic trsnducer (46)

The rectangular section of the transducer is divided into *n* segments spaced by *dL* along the length of the transducer (*L*). All line segments are further divided into *m* different points with a step size of *dw* along the width of the transducer. Hence, the coordinates of point sources can be expressed as (49, 50):

$$x_m = (m-1)\cdot dw - \frac{w}{2}; y_n = (n-1)\cdot dL - \frac{L}{2} \quad (3.4)$$

where *n* line segments are given as (n = 1, 2 ... N); *m* point sources are given as (m = 1, 2 ... M); x_m and y_n are the *x* and *y* coordinates of the point sources.

The simulation time depends on step sizes (*dL* and *dw*). By keeping the step sizes longer, simulation time can be reduced by compromising the resolution and accuracy of results. The optimal values can be selected depending on the size of the transducers. The *k* arbitrary receiving elements equally spaced from 0 to 180° along the half-circle at distance *R* from the center of transducer (origin) are created. Hence, the location of receiving elements can be given as (49, 50):

$$x_k = R\cdot cos\theta_k;\ y_k = R\cdot sin\theta_k \quad (3.5)$$

where k receiving elements are given as (k = 1, 2 ... K); θ_k is the angle between the k^{th} receiving point and origin (θ_k = [(k−1) ·$d\theta$]; $d\theta$ is the angular separation between receiving elements); x_k and y_k are the x and y coordinates of the receiving elements.

The distance from the m^{th} point source to the k^{th} receiving element can be calculated as(49, 50):

$$d_{k,n,m} = \sqrt{(x_k - x_m)^2 + (y_k - y_n)^2} \tag{3.6}$$

$$\theta_{k,n,m} = tan^{-1}\left[\frac{y_k - y_n}{x_k - x_m}\right] \tag{3.7}$$

where $d_{k,n,m}$ is the distance vector and $\theta_{k,n,m}$ is the corresponding angle.

The transfer function for the plane waves can be calculated by multiplying the attenuation and phase components (49, 50):

$$H_T\left(f, d_{k,n,m}, v_{ph}\right) = e^{-\propto(f)\cdot d_{k,n,m}} \cdot e^{-j\frac{2\pi f d_{k,n,m}}{v_{ph}(f,h)}} \tag{3.8}$$

where H (f, $d_{k,n,m}$, v_{ph}) is the transfer function; $\alpha(f)$ is the frequency-dependent attenuation coefficient; v_{Ph} phase dispersion velocity depends on the thickness (h) of the medium and the frequency of excitation.

The correction factor (C_F) depends on the type of propagating GW mode (*e.g.* the A_0, S_0 or SH_0) and can be expressed as (50):

$$C_F = A_F \cdot D_F\left(\theta_{k,n,m}\right) \tag{3.9}$$

where A_F and D_F are the amplitude and direction factors of the particular wave mode.

The correction factor is multiplied to the input signal depending on the requirement to estimate the directivity-specific GW mode. Hence the modified/corrected time-domain input signal can be calculated as (50):

$$u_{EC}(t) = u_E(t) \cdot C_F \tag{3.10}$$

where $u_{EC}(t)$ is the corrected/modified input signal; $u_E(t)$ is the original input signal.

The frequency-domain output signal is therefore estimated as (50):

$$U_{R,k}(f, \theta_k) = \sum_{n=1}^{N}\sum_{m=1}^{M} U_{EC}(f) \cdot H_T\left(f, d_{k,n,m}, v_{ph}\right) \cdot \frac{1}{\sqrt{d_{k,n,m}}} \tag{3.11}$$

where $U_{EC}(f)$ is FT of the modified input signal $u_{EC}(t)$; $U_{R,k}$ (f, θ_k) is the FT of the received signal and $1/\sqrt{d_{k,n,m}}$ is the diffraction factor corresponding to the distance.

The time-domain received signal is calculated by taking the inverse Fourier transform (FT^{-1}) of the $U_{R,k}(f, \theta_k)$ (50):

$$u_{R,k}(t,\theta_k) = FT^{-1}\left[U_{R,k}(f,\theta_k)\right] \tag{3.12}$$

The peak-to-peak amplitudes (A_{pp}) and the normalized peak-to-peak amplitudes (A_{npp}) of received signals can be calculated as follows (50):

$$A_{pp}(\theta_k) = \max\left[u_{R,k}(t,\theta_k)\right] - \min\left[u_{R,k}(t,\theta_k)\right] \tag{3.13}$$

$$A_{npp}(\theta_k) = \left[\frac{A_{pp}(\theta_k)}{\max\left[A_{pp}(\theta_k)\right]}\right] \tag{3.14}$$

where $A_{pp}(\theta_k)$ and $A_{npp}(\theta_k)$ p-p amplitudes and normalized p-p amplitudes.

The directivity pattern therefore can be plotted as normalized amplitudes of the received signal with respect to the angle θ_k in a polar coordinate system.

3.5.2 2D analytical model in the case of P1-type MFC transducer glued on Al alloy plate

The P1-type MFC transducer with active dimension of 28×14 mm is considered for the demonstration of the proposed 2D analytical model. The 2 mm thick Al alloy plate with infinite length and width is considered as a propagation medium. The directivity of the fundamental Lamb modes (the S_0, A_0) and SH_0 mode has to be determined at a distance of 300 mm from the center of the MFC transducer. The 80 kHz, 5-period burst signal with Gaussian symmetry is used as an excitation signal. There were no specific criteria in selecting the 80 kHz frequency. The motivation behind this decision is to compare the directivity patterns at different frequencies and validate them with experimental and *FE* modelling. Firstly, an 80 kHz frequency is selected, then the directivity patterns at 220 kHz and resonant frequency (43 kHz) are estimated. The received signals are recorded at a sampling frequency of 1.6 MHz. The phase velocity dispersion characteristics for a 2 mm thick Al alloy plate are calculated with the computational package *Disperse* (82). The excitation signal and dispersion characteristics for a 2 mm Al plate are shown in Fig. 3.11. The parameters of the Al alloy plate have already been described in Table 3.2. The phase velocities at 80 kHz were observed as 1183 m/s, 2903 m/s and 5409 m/s in case of the A_0, SH_0 and S_0 modes, respectively.

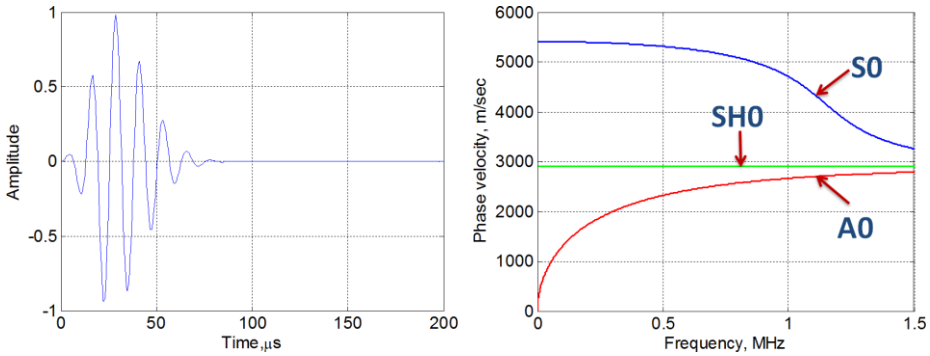

(a) (b)

Fig. 3.11. An excitation signal of 80 kHz, 5 periods (a) and phase velocity dispersion characteristics of 2 mm Al alloy plate (50)

According to the modelling steps discussed in Section 3.5.1, the directivity of the propagating wave modes (the S_0, A_0, SH_0) is estimated. Along the length (28 mm) of MFC transducer, 29 segments equally spaced by 1mm are considered. Each segment is divided into 15 points in order to describe the distributed point sources over the structure of MFC. The arbitrary receiving zone is created by considering 181 arbitrary sensing elements from 0 to 180° with an angular separation of 1° along the half-circle. The distance between all sensing points and the center of the transducer was selected as 300 mm. As aluminum is an isotropic and lossless medium, the value of attenuation coefficient α (f) was considered as *zero*. The direction and behavior of particle displacements of P1-type MFC transducer are shown in Fig.3.12a. Due to the operational behavior of P1-type MFC in elongation mode, the particles in the upper and lower half of MFC transducer travel in the opposite direction along its length. The estimation of correction factor (C_F) which depends on the amplitude and direction of propagating wave mode is presented in Fig. 3.12b. The amplitude factor (A_F) was selected as a linearly increasing value from 0 (at the center of MFC transducer) to ±1 (at the edges of MFC) along the length.

The theory of GW modes implies that S_0 mode possesses dominant radiation in the direction of wave propagation, while the SH_0 contains dominant radiation in the direction perpendicular to the direction of wave propagation and A_0 contains dominant *out-of-plane* radiations. By utilizing this theoretical description and the behavioral characteristics of MFC transducer, the direction factor (D_F), can be considered as constant (*e.g. unity*), *cos* ($\theta_{k,n,m}$) and *sin* ($\theta_{k,n,m}$) for the A_0, SH_0 and S_0 modes, respectively, as illustrated in Fig. 3.12b.

The correction factor for each mode can be calculated from Eq. (3.15) as (49, 50, 59):

$$\begin{aligned} C_F(S_0) &= A_F(y) \cdot sin\left(\theta_{k,n,m}\right), \\ C_F(SH_0) &= A_F(y) \cdot cos\left(\theta_{k,n,m}\right), \\ C_F(A_0) &= A_F(y) \end{aligned} \tag{3.15}$$

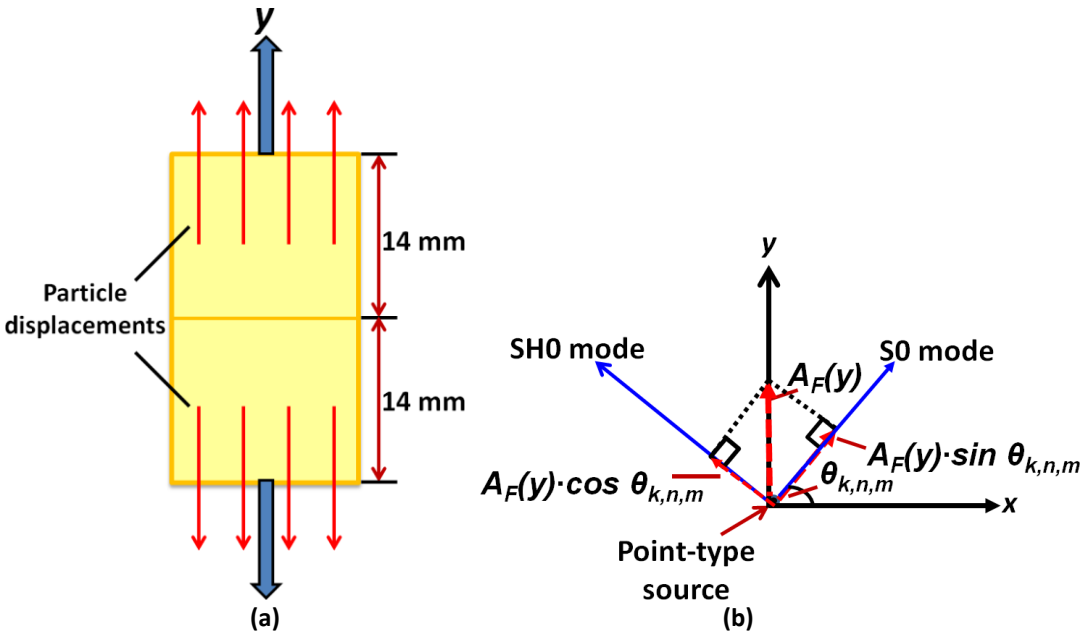

Fig. 3.12. Particle displacements in P1-type MFC transducer (a) and correction factor C_F (multiplication of amplitude factor A_F and direction factor D_F) (b) (46)

3.5.3 Numerical modelling using finite element analysis

The *FEA* is performed by *ANSYS* commercial software package to verify the proposed analytical model. The Al alloy plate of dimension 1000×1000×2 mm was modeled in a three coordinate system (3D). *SOLID* 64 elements were used to develop the 3D model which is frequently used for solid-type structures. Each element with a size of 1 mm had eight nodes with three degrees of freedom or translation into three coordinates (*x*, *y* and *z* directions). The mechanical properties of Al alloy plate are already presented in Table 3.2 (50).

Instead of developing an explicit model of P1-type MFC transducer, only its behavior was considered to be incorporated in the modelling (196). The same excitation signal (force) of 80 kHz, 5 periods of sinusoidal burst with Gaussian symmetry as shown in Fig. 3.11a is used to excite the transducer. The sampling frequency (1.6 MHz) was also similar to that used in analytical modelling. In order to create the transmitting zone similar to the behavior of P1-type MFC transducer of dimension 28x14 mm, lower and upper half sections of the MFC transducer were excited with excitation signals in opposite phases. Only an arc from 0 to 90° (one-

quarter of a circle) of 300 mm radius is considered in order to reduce the simulation time as illustrated in Fig. 3.13 (50).

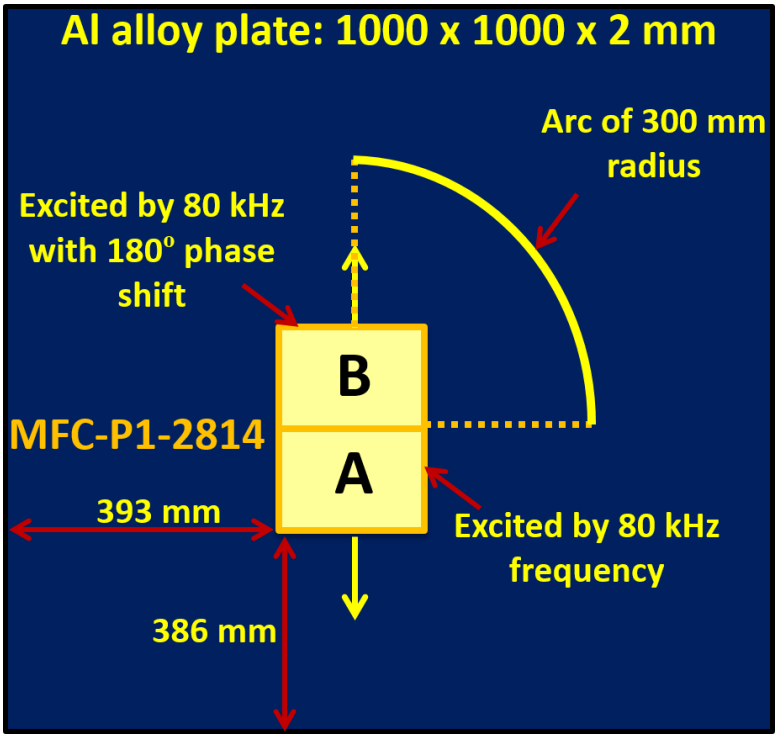

Fig. 3.13. Explanation of numerical modelling using *FEA* (50)

The rectangular section of the MFC transducer was located at 386 mm from the bottom and 393 mm from the left edge of the Al alloy plate. Numerical integration was performed to obtain a solution. The variations in particle velocities at various time instants were obtained in the structure. The calculation of resultant particle velocities in the direction of propagation, perpendicular to the direction of propagation and *out-of-plane* to plot the respective directivity patterns of S_0, SH_0 and A_0 modes is presented in Fig. 3.14 (50).

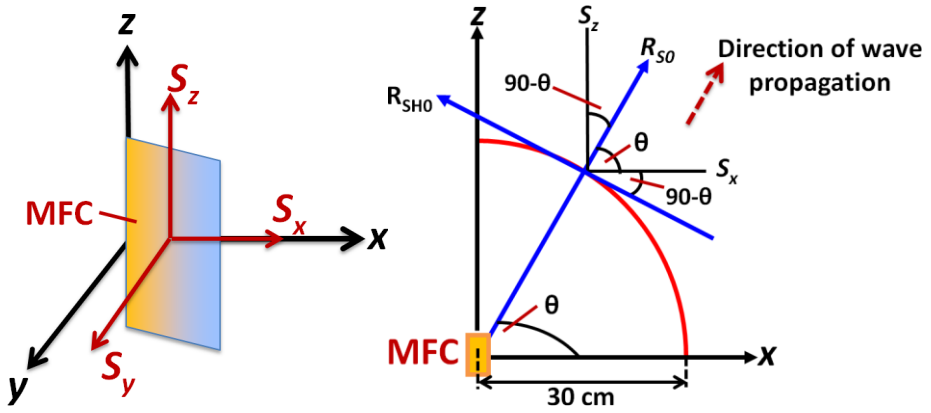

(a) (b)

Fig.3.14. Particle velocities (S_x, S_y and S_z) in the *x*, *y* and *z*-direction (a); Resultant received signals (R_{S0}) and (R_{SH0}) in the direction and perpendicular to the direction of propagation, respectively (b) (46)

- Let us consider the three components of particle velocities along the MFC width (*x*-axis), out-of-plane (*y*-axis) and along the MFC length (*z*-axis) are denoted by S_x, S_y and S_z, respectively, as shown in Fig. 3.14a (50).
- A graphical representation of the estimation of resultant signals for the calculation of directivity of S_0 (R_{S0}) and SH_0 (R_{SH0}) modes is presented in Fig. 3.14b. The resultant signal for calculating the directivity of *out-of-plane* A_0 mode (R_{A0}) is equal to S_y. If θ is the angle to the direction of wave propagation from the positive *x-axis*, the resultant signals can be expressed as (49, 50):

$$R_{S0} = S_z sin\theta + S_x cos\theta \quad (3.16)$$

$$R_{SH0} = S_z cos\theta - S_z sin\theta \quad (3.17)$$

$$R_{A0} = S_y \quad (3.18)$$

Fig. 3.15a-c shows the B-scan images of the resultant signals after processing the data in *MATLAB* (50). It can be observed from Fig. 3.15a-c that time-of-arrival of A_0, SH_0 and S_0 are 225 μs, 175 μs and 100 μs, respectively (50). Therefore, the fastest mode is S_0. The directivity patterns of each of S_0, A_0 and SH_0 modes can be constructed by plotting these signals (R_{S0}, R_{SH0}, R_{A0}) in the polar axis.

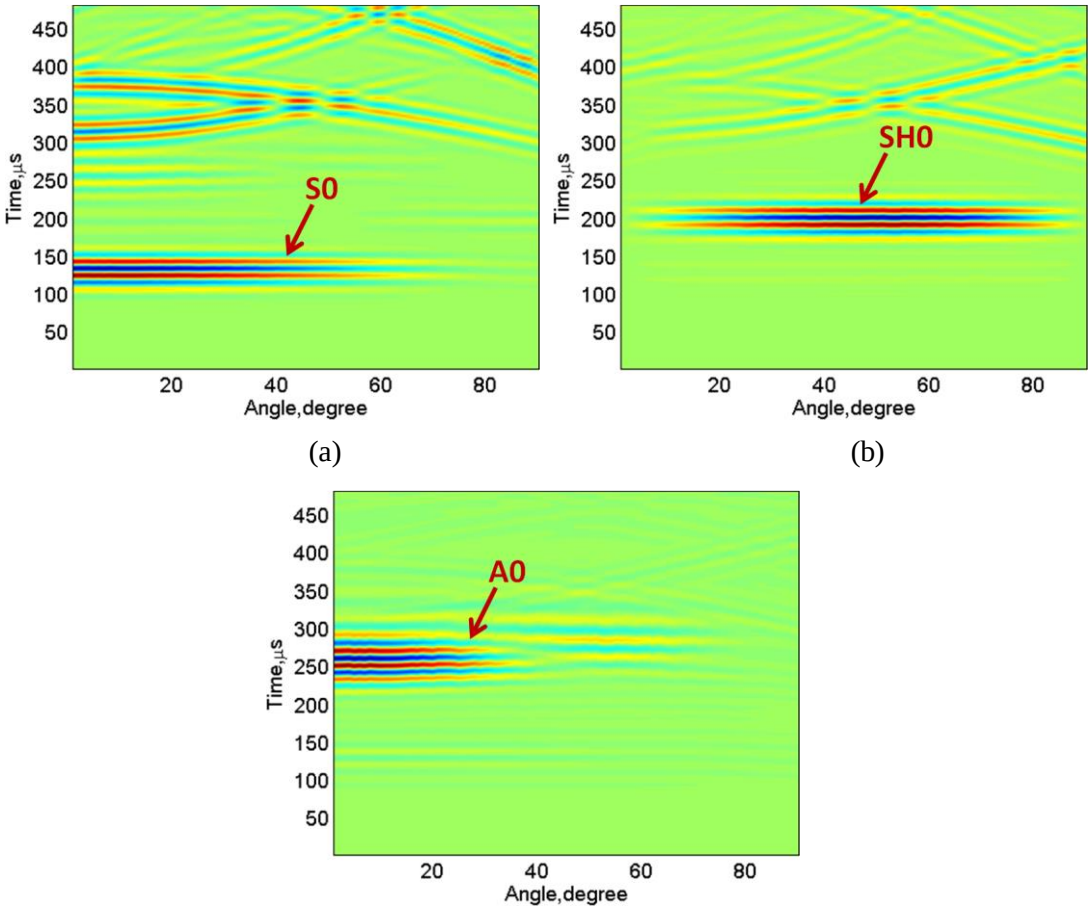

Fig. 3.15. The B-scan images of resultant particle velocities in the direction of propagation (the S_0) (a), perpendicular to the direction of propagation (the SH_0) (b), and *out-of-plane* (the A_0) (c) (46).

3.5.4 Experimental analysis

The experiment was performed to calculate the directivity of a P1-type MFC transducer. A schematic of the experiment is shown in Fig.3.16. The propagation medium was the Al alloy plate and its characteristics are already described in Table 3.2. The dimensions of Al alloy plate was 1000×1000×2 mm) and the MFC transducer was glued at its center. The MFC was excited with 80 kHz, 5-period burst signal having Gaussian symmetry. The point-type contact ultrasonic transducer, as described in Section 2.2.1, was used to record the GW signals (50, 53, 55, 101). The sampling frequency used was 100 MHz. It should be noted that a contact-type receiver operates in thickness mode which is more sensitive to the *out-of-plane* dominating components

of the A_0 mode. Hence the directivity of A_0 mode was calculated from the experimental analysis.

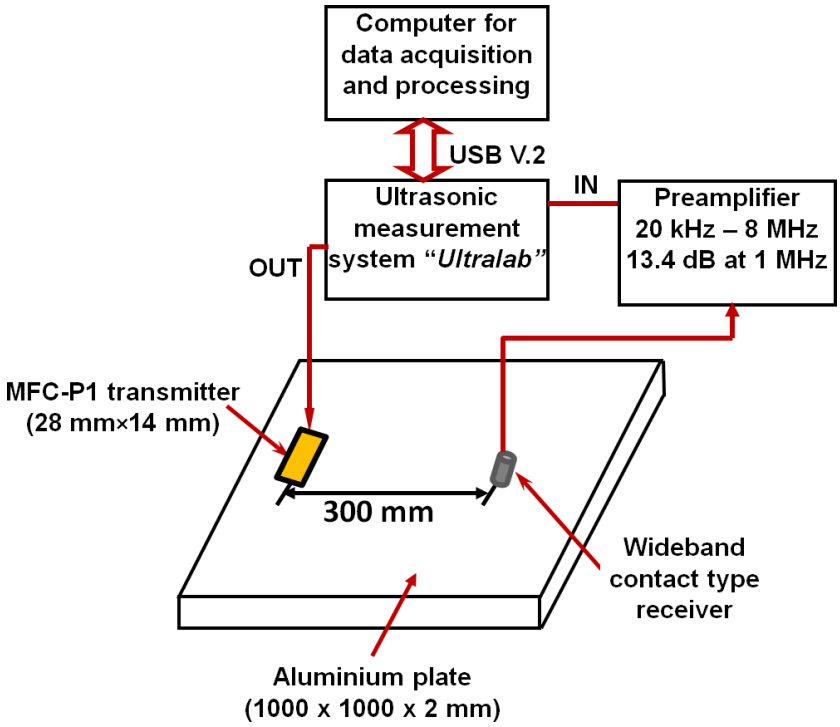

Fig. 3.16. Experimental set-up for the analysis of directivity of P1-type MFC transducer glued on an Al alloy plate (46).

The LF ultrasonic system *Ultralab* developed at the Ultrasound Institute of Kaunas University of Technology was used in the experiment. The characteristics of the LF ultrasonic system are already presented in Table 2.3 (see Chapter 2.2).

The experiment is performed in a pitch-catch mode. The MFC transducer was glued/fixed at the center of an Al plate and the contact-type receiver was scanned up to 200 mm towards MFC transducer. The initial position of the receiver was 300 mm from the center of the MFC transducer. In order to avoid interference and mode mixing, scanning along the arc to calculate directivity was not performed. Instead, the scanning and signal processing procedure as presented in Fig. 3.17 is performed (50).

Similarly to the numerical modelling, the symmetry in MFC structure facilitated to scan only an arc from 0 to 90° (one-quarter of a circle) of 300 mm radius for shortening the time spent in the experiment. In total, 19 B-scans are acquired at each 5° as shown in Fig.3.17a. The scanning step was 0.5 mm. In order to pick up the dominant A_0 mode, 2D-FFT (132) is applied to all B-scans. The rectangular window

of 60–110 kHz in frequency and 0.04-0.075 1/mm in spatial frequency was applied to the dispersion curves of all 19 B-scans after *2D-FFT*. However, only three dispersion curves obtained by the *2D-FFT* of the first, tenth and nineteenth B-scans obtained at 0°, 45° and 90°, respectively, are shown in Fig. 3.17b-d. After applying the frequency-window, the directivity patterns were constructed by taking into account the maximum energy of all 19 signals. To validate the modelling results at different frequencies, another frequency of excitation (*e.g.* 220 kHz) is selected. The experiment was performed again with the same set-up by exciting the MFC transducer with 220 kHz, 5-period burst signal.

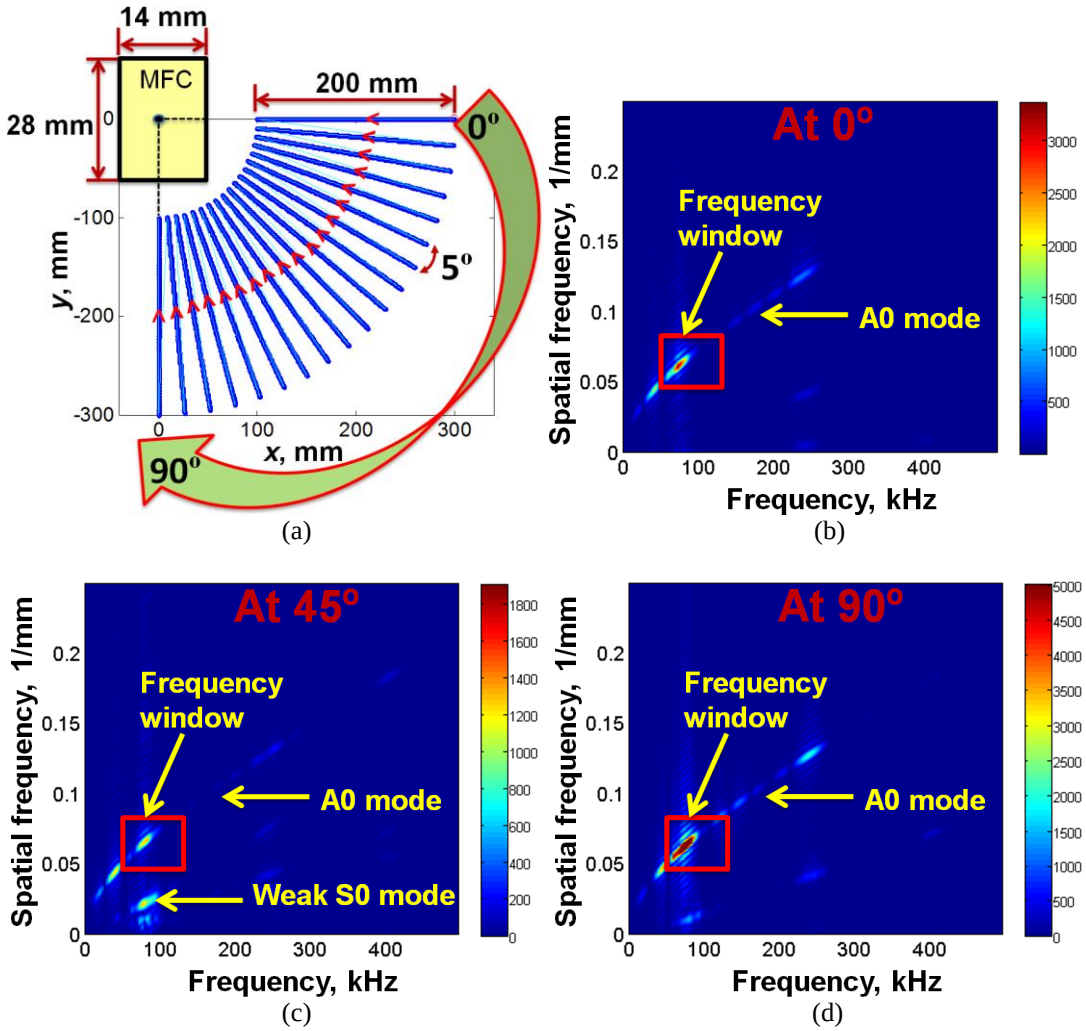

Fig.3.17. A schematic of the scanning procedure performed in the experiment (a); Dispersion curves and frequency window for the first, tenth and nineteenth B-scans at 0°, 45° and 90°, respectively (46).

3.5.5 Results and discussions

The directivity characteristics obtained from the analytical modelling and numerical modelling are perfectly match each other. Fig. 3.18a-c compares the directivity patterns of MFC transducer in S_0 mode, A_0 mode and SH_0 mode, respectively, at 80 kHz obtained by analytical and numerical modelling (49, 50):

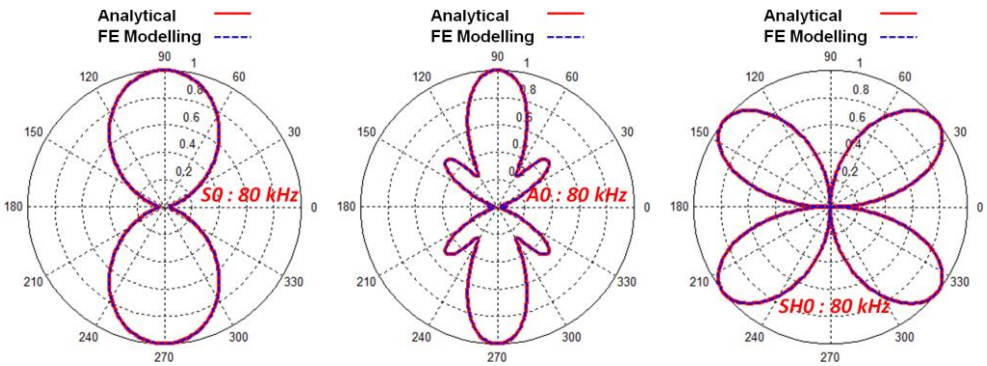

(a) (b) (c)

Fig. 3.18. Directivity patterns of the S_0 (a), A_0 (b) and SH_0 (c) GW modes at 80 kHz (46).

After observing the results (Fig. 3.18), the outcomes are described as follows (50):

- The S_0 guided wave mode is most directional and dominant among all three GW modes. It confirms the operation of P1-type MFC transducer in elongation mode. Moreover, S_0 and A_0 contain dominant wave energy (major lobes) in the longitudinal direction (90°or 270°). However, the beam-width of S_0 mode was observed as broader compared to the A_0 mode.
- The minor lobes at 0°, 40°, 140°, 180°, 220° and 320° were observed in the directivity pattern of A_0 mode (Fig. 3.18b).
- The directivity pattern of the SH_0 wave showed radiation intensities in the direction towards 40°, 140°, 220° and 320°.
- These directions could suggest where to locate the transducer or which GW mode must be used to inspect the damages/defects on the structure.
- Operating wavelength of S_0 wave was 67 mm as compared to the 14.83 mm that of A_0 mode. The comparison of wavelengths with the length of the MFC transducer affects the shape of directivity patterns (49, 50).

As analytical and FE modelling results are identical, the next step is to compare the analytical modelling and experimental results. The directivity patterns of the A_0 mode obtained using the proposed analytical model are compared with the experimental results at two different excitation frequencies (80 kHz and 220 kHz) and presented in Fig. 3.19. It should be noted that the selection of 80 kHz and 220 kHz

frequencies to present the modelling and experimental results had no specific reasons rather than showing the validity of the developed analytical model at different frequencies. It can be clearly observed from Fig 3.19a-b that the shape of major lobes of directivity patterns obtained experimentally are almost identical to the analytical results. The shape and number of minor lobes also match but the size of minor lobes shows a significant difference. In comparison to the directivity characteristics at 220 kHz (Fig. 3.19a), the major lobes are broader at 80 kHz (Fig. 3.19b), with a lesser number of minor lobes (50).

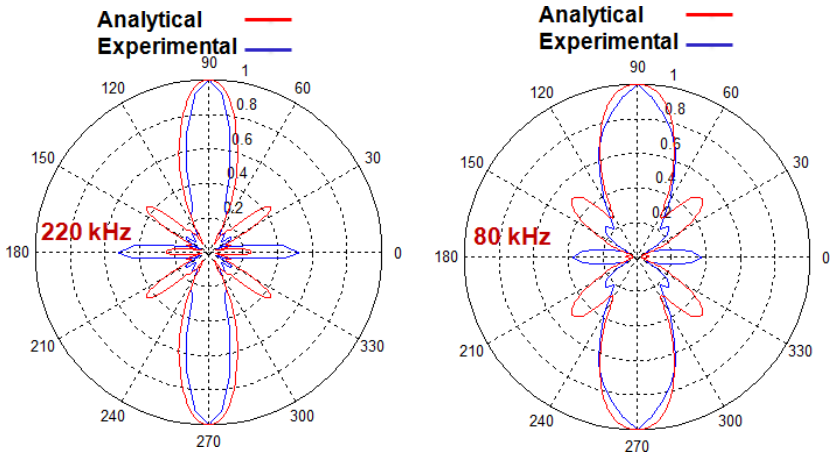

Fig. 3.19. A comparison of directivity patterns of the A_0 obtained by proposed analytical model and experiment at excitation frequency of 220 kHz (a) and 80 kHz (b) (46).

The difference between the size of minor lobes in analytical and experimental results is associated with the amplitude of signal distribution (amplitude correction factor (A_F)) along the MFC structure as described in Chapter 3.5.2. During the implementation of analytical modelling, the approximated value of the amplitude correction factor was considered as zero at the center and linearly increased up to ±1 at the edges of MFC. In future research, the modelling results can be improved by considering a more accurate value of the amplitude correction factor.

Apart from the shapes of the minor lobes, the results at two different frequencies showed a good matching, hence the developed 2D analytical model can be used to predict the directivity pattern of a contact-type transducer with known dispersive characteristics of the medium. The directivity of MFC transducer at resonant frequency (43 kHz) is also estimated by the analytical model and presented in Fig. 3.20.

It can be clearly observed in Fig. 3.20 that directivity patterns for S_0 and SH_0 modes are almost similar to that of 80 kHz frequency. However, the directivity pattern of A_0 mode at 43 kHz is not as directional compared to the 80 kHz but covers a broader

region. As mentioned earlier, the shape and size of major and minor lobes of directivity patterns depend on many factors, therefore, it is always better to estimate an approximated directivity pattern of a specific mode of interest in the case of glued/embedded transducer used before testing the sample.

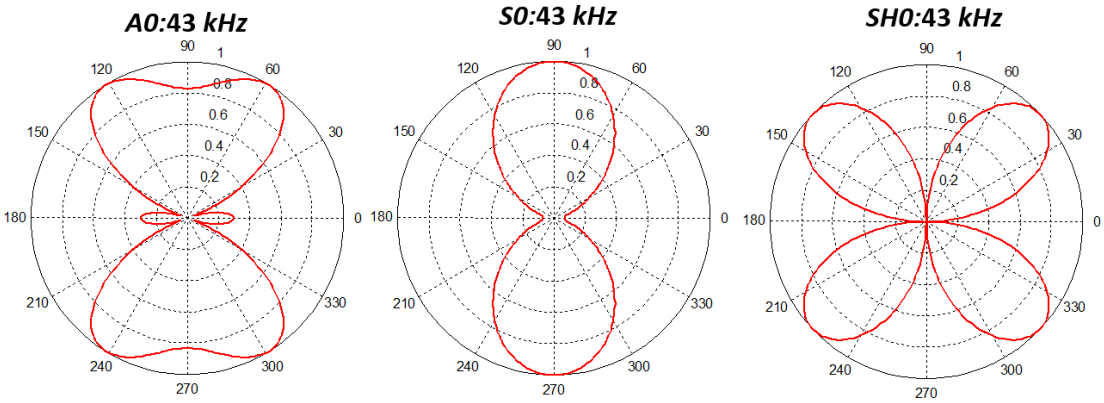

(a) (b) (c)

Fig. 3.20. Directivity patterns of the A_0 (a), S_0 (b) and SH_0 (c) GW modes at 43 kHz by the developed analytical model.

3.5.6 Directivity pattern of MFC transducer in GFRP material at resonant frequency

In this dissertation, an MFC transducer is glued on the GFRP material and a contact-type receiver is used to pick-up the A_0 mode for the estimation of defects by using long-distance GW testing by exciting the MFC at 43 kHz frequency (see Chapter 4). The directivity of the MFC transducer in the defect-free region of GFRP material at 43 kHz frequency has been estimated (in the case of A_0 mode). It should be noted that the dispersive characteristics of the multi-layered composite material (*e.g.* GFRP) are different in different angular directions in comparison to the isotropic materials. That is why the semi-analytical finite element (SAFE) method is used to calculate 19 phase velocity dispersion characteristics at every 5° angle in the range of 0° to 90° degrees (197, 198, 199, 200). Phase velocity dispersion characteristics at 90 (along the longitudinal direction of MFC), 45 and 0° (along the width of MFC) angular directions are shown in Fig. 3.21a-c. However, only the guided A_0 mode is considered to estimate the phase velocities. Afterward, the directivity pattern of A_0 modes is estimated in the range of 0 to 360° as the MFC transducer has a symmetrical structure. It is also assumed that the layered structure of composite is similar in the angular range of (0–90° and 90–180°.) and (0–180° and 180–360°). The properties of GFRP material is already presented in Table 2.2 (see Chapter 2.2.1 for details). The thickness of various layers in the defect-free and defective regions are illustrated in Table 3.3 (55).

However, only the defect-free region is considered to estimate the dispersion curves by using the SAFE method. The overall thickness of the GFRP sample is considered as 22 mm. The attenuation in the medium is ignored for the prediction of directivity pattern.

The phase velocities of A_0 mode did not show any significant differences and the phase velocity of A_0 mode along 90, 45 and 0° at 43 kHz resonant frequency was observed as 1190, 1196 and 1183 m/s, respectively. The directivity pattern of A_0 mode is presented in Fig. 3.21d. It is clear that major lobes (maximum directivity) occur at 90 and 270 (in the longitudinal direction of the MFC transducer), hence the defects located on the GFRP sample can be inspected by the A_0 waves if they exist along the longitudinal axis of MFC.

Table 3.3. The thickness of layers in defect-free and defective region (55)

Parameters	**Numerical Value**
Defect-free region:	
Thickness of paint	0.5 mm
GFRP (0°/90°/45°/−45°/0°) layer	2 mm
Epoxy	1 mm
GFRP (45°/−45°) layer	18.5 mm
Defective region:	
Thickness of paint	0.5 mm
GFRP (0°/90°/45°/−45°/0°) layer	2 mm
Epoxy	1 mm

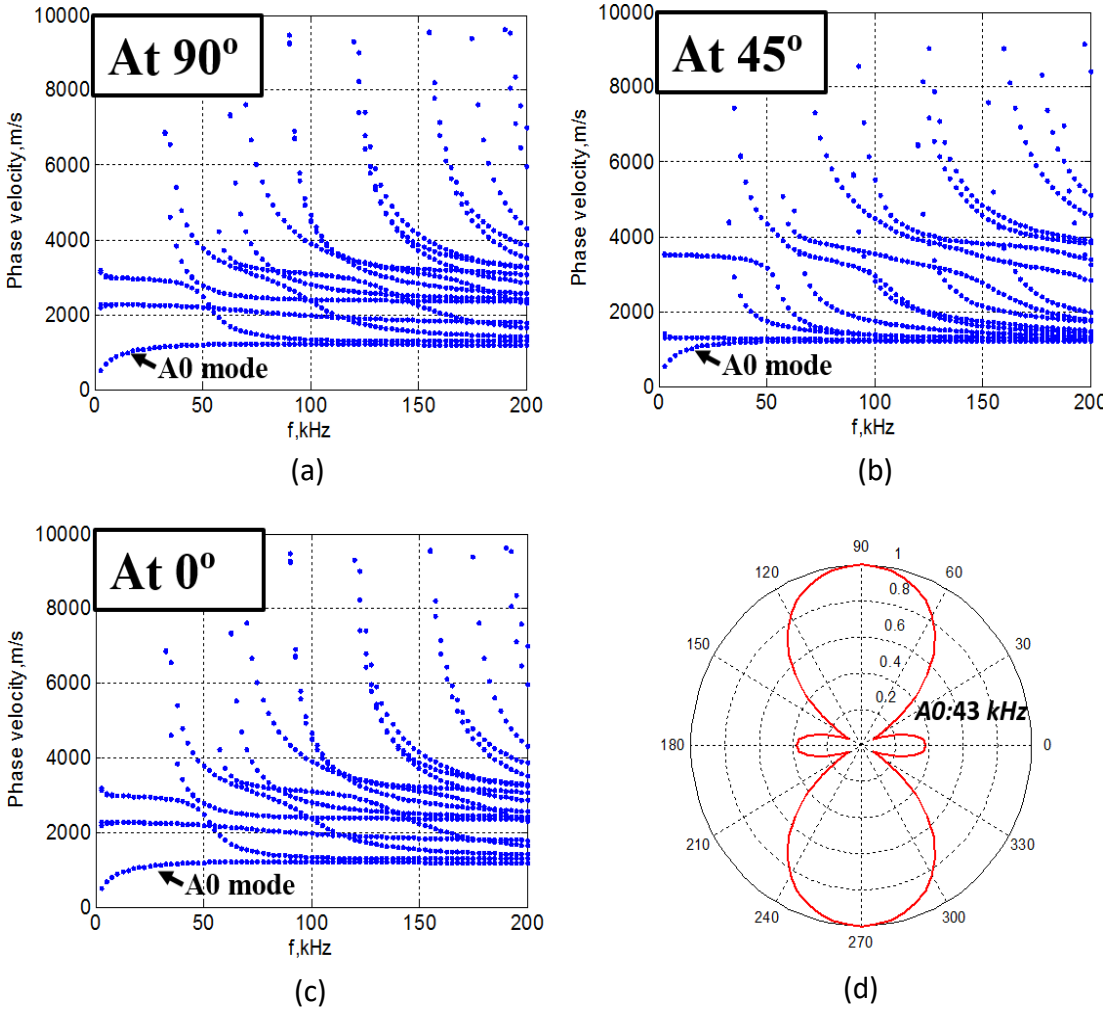

Fig. 3.21. Phase velocity dispersion curves along the 90, 45 and 0° in GFRP material. (a–c); The directivity pattern of P1-type MFC transducer (A_0 mode) in GFRP material at 43 kHz (d).

After analyzing the 3D characteristics of the MFC transducer and directivity patterns of MFC transducer in Al and GFRP material, the next Chapter presents the utilization of an MFC transducer as a transmitter for the generation of GWs and estimation of disbond-type defects located on the main spar of GFRP material using long distance GW testing. The directivity of MFC transducer (A0 mode) in GFRP concludes that the MFC transducer should be glued on the GFRP sample in such a way that defects align along the longitudinal direction of the MFC transducer.

3.6 Conclusions

1. The feasibility of an MFC transducer to be glued/embedded on the composite structure for long-distance GW testing has been analyzed by estimating its three-dimensional displacement characteristics and directivity patterns. Analyzing the three-dimensional characteristics of an unloaded transducer can assure its validity for its application in the nondestructive testing of composite structures. Moreover, it also ensures that the transducer itself is defect-free to be used in real-time applications. The estimation of directivity patterns can assure the position where the transducer can be fixed, the selection of appropriate wave mode and an excitation frequency of a transducer.
2. The measured value of the maximum longitudinal displacement (*in-plane Y* component) was observed as highest (167 nm) when compared to the *in-plane X* component (35 nm) and *out-of-plane Z* component (100 nm) (48). As the S_0 wave contains dominant wave components in longitudinal and the direction of propagation, it confirms that the MFC transducer of P1-type can effective generate/receive the S_0 Lamb wave for non-destructive testing and structural health monitoring of structures. However, the A_0 wave also has a significant value of maximum displacement. The variations of three displacement components with respect to the time were also compared at the center and corner points of the MFC transducer. The maximum amplitudes of X and Z displacements at the center and corner were almost identical. On the other hand, the rapid rise in the maximum amplitude of Y displacement component was observed from its value at the center to the corner point. It once again confirms that the P1-type MFC works in elongation or d33 mode.
3. The measurement results of three-dimensional displacement characteristics showed a good compromise with the behavior of P1-type MFC transducer as presented by the manufacturer. Hence, analyzing the three-dimensional characteristics of the unloaded transducer can assure its validity for application in the nondestructive testing of composite structures. Moreover, it also ensures that the transducer itself is defect-free to be used in real-time applications.
4. A novel 2D analytical model based on the Huygens's wave propagation principle is proposed to predict and estimate the directivity pattern of any contact-type transducer. A P1-type MFC transducer and 2 mm thick Al alloy medium are used for a demonstration of modelling. It should be noted that dispersive phase velocity in the modelling is included by calculating the theoretical dispersion curves based on the thickness of propagating medium. The model has significant flexibility by providing the option of selecting the propagation medium, frequency of excitation, type of transducer, etc. Moreover, the simulation time is significantly shorter as compared to the time spent on achieving results by experiments and finite element modelling.

5. The 2D model is verified with finite element modelling in *ANSYS* for the excitation frequency of 80 kHz. The modelling of the propagation medium (Al alloy) has been performed but the MFC transducer is included in the modelling based on its behavior. As P1-type MFC operates in elongation mode, the upper and lower halves of the transducer section (28 x 14 mm) on the Al plate are excited with same frequency but opposite in phase. The analytical and results obtained by numerical modelling showed good similarities. Further validation for the reproduction of results from the 2D analytical model, the experimental analysis has been performed at two different frequencies (80 kHz and 220 kHz). The contact-type receiver operating in thickness mode is used to pick up the *out-of-plane* radiations. Later on, the directivity patterns at resonant frequency of MFC transducer (43 kHz) are estimated. The directivity patterns of S_0, A_0 and SH_0 modes provide the direction of these propagating wave modes. These directions are very important in the utilization of MFC transducer for inspecting structures using ultrasonic non-destructive testing. These directivity patterns suggest that defects/damages along the direction and perpendicular the direction of wave propagation cannot be tested by SH_0 waves in Al alloy. Moreover, the S_0 and A_0 are highly directional in the direction of propagation for testing the structures. It is also observed that the beam width of S_0 and A_0 waves reduces with an increase of excitation frequency but the directivity reduces.
6. After validating the developed 2D model for the directivity pattern of MFC transducer in Al plate, the model is used to estimate the directivity patterns in GFRP composite material. The phase velocities of A_0 mode in GFRP material along different angular directions are estimated by the SAFE method. It is concluded that defects located on a GFRP sample can be investigated by using the A_0 waves generated by a glued MFC transducer providing that the defects exist along the longitudinal axis of the MFC transducer.

4. MEASUREMENT TECHNIQUE BASED ON LONG-DISTANCE GUIDED WAVES

4.1 Demand and motivation

Large structures can be inspected by gluing or embedding an MFC transducer (transmitter) and a contact-type transducer (receiver) can be scanned away. In this research the contact-type transducer used to receive GWs is more sensitive to the *out-of-plane* (A_0) GWs. In Chapter 3, it is observed that a P1-type MFC transducer has dominant longitudinal or S_0 wave components but it still generates significant *out-of-plane* wave components. The directivity pattern of A_0 waves generated by a P1-type MFC transducer in the GFRP (see Chapter 3.4.6) also confirms that defects in GFRP can be estimated by the A_0 waves if an MFC transducer is glued longitudinally towards the defective region. In this way a single linear scan (B-scan) acquired by scanning away the contact-type receiver is enough to estimate and characterize defects by processing the dominant A_0 waves.

In this Chapter, a measurement technique based on an MFC transducer as a transmitter and a contact-type transducer as a receiver with appropriate signal processing methods are proposed for the inspection of disbond-type defects in large composite structures by using long distance GW testing. The same multi-layered composite sample (GFRP) which has been a segment of WTB, as used in Chapter 2, is used for the experimental investigation. However, the defect is located on the main spar of WTB instead of the trailing edge of WTB.

The flow-graph of the measurement technique is presented in Fig. 4.1. The experiment is performed by gluing the MFC transducer and scanning away the contact-type receiver. A B-scan acquired after linear scanning over the defective region is processed for the estimation and characterization of the defect. DWT and amplitude detection are performed to locate and size the defect. Thereafter, the 2D-FFT is applied in order to suppress the reflected waves from the other side of the surface. Finally, VMD and HT are applied to obtain instantaneous amplitude characteristics of GWs in the defective and defect-free regions, which in turn is used to calculate the time-or-arrival and phase velocities of the propagating wave modes.

The organization of the Chapter is described below:

- Experimental investigation of the GFRP sample containing an 81 mm disbond-type defect on the main spar is performed in Section 4.2 by using a glued P1-type MFC transducer (transmitter) and a contact-type transducer (receiver).
- The development of signal processing algorithm based on DWT, 2D-FFT, HT and VMD to extract and characterize the defect by processing the single B-scan is presented in Section 4.3. The SAFE method is also used to compare phase velocities calculated by the signal processing approach.
- The conclusions of the Chapter including limitations and issues are presented in Section 4.4.

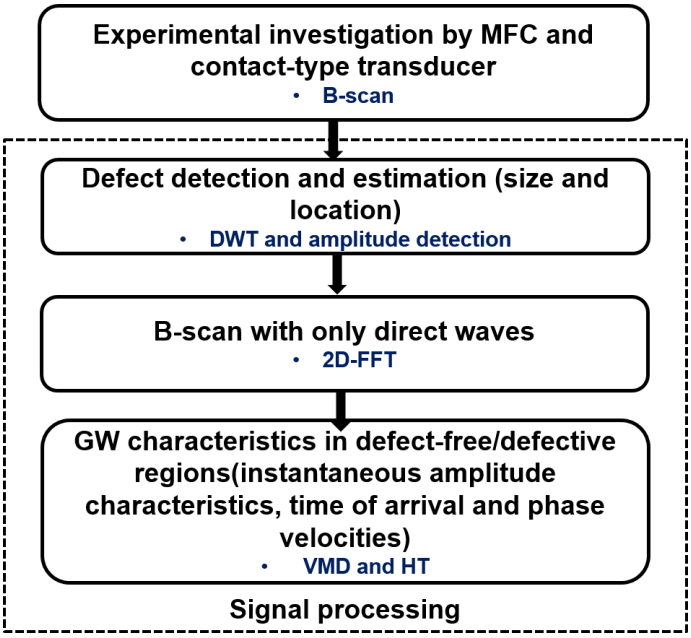

Fig. 4.1. Flowgraph of measurement technique for the defect estimation and characterization in composite structure by long-distance ultrasonic GWs.

4.2 Experimental investigation on the main spar of sample containing a disbond-type defect

The same GFRP sample described in Section 2.2 which is a segment of a WTB that was used in this analysis. The artificially constructed 81 mm disbond-type defect using the milling process was investigated. The defect was located on the main spar of GFRP sample. The thickness of the sample was not fixed in the defect-free and defective regions.

The thickness range was 20–23 mm in the defect-free and 3–4 mm in the defect-free region. The front and inner views of the sample are shown in Fig. 4.2a, b. In order to transmit guided Lamb waves, the P1-type MFC transducer (103) analyzed in Chapter 3 was used. As the P1-type MFC transducer contained dominant S_0 and A_0 wave modes in the direction of longitudinal axis and *out-of-plane* (50), the variations in the propagating waves can provide information about defects. The MFC transducer was glued on the inner side of the sample where the defect was visible. The contact-type piezoceramic transducer as described in Chapter 2.2 is used in the experimental investigation. The visualization of the defect was not possible during the experiment as scanning was performed on the front side whereas the defect could be visible only from the inner side of the sample.

It should be noted that the contact-type receiver was more sensitive to A_0 waves, our analysis to extract the defect features would be on the basis of characteristics of

A_0 wave in the defect-free and defective regions. The receiver was initially located at 291.5 mm from the transmitter before beginning the scanning process. The complete arrangement showing the locations of the defect, the glued MFC transducer and receiver on the GFRP sample is shown in Fig. 4.2c.

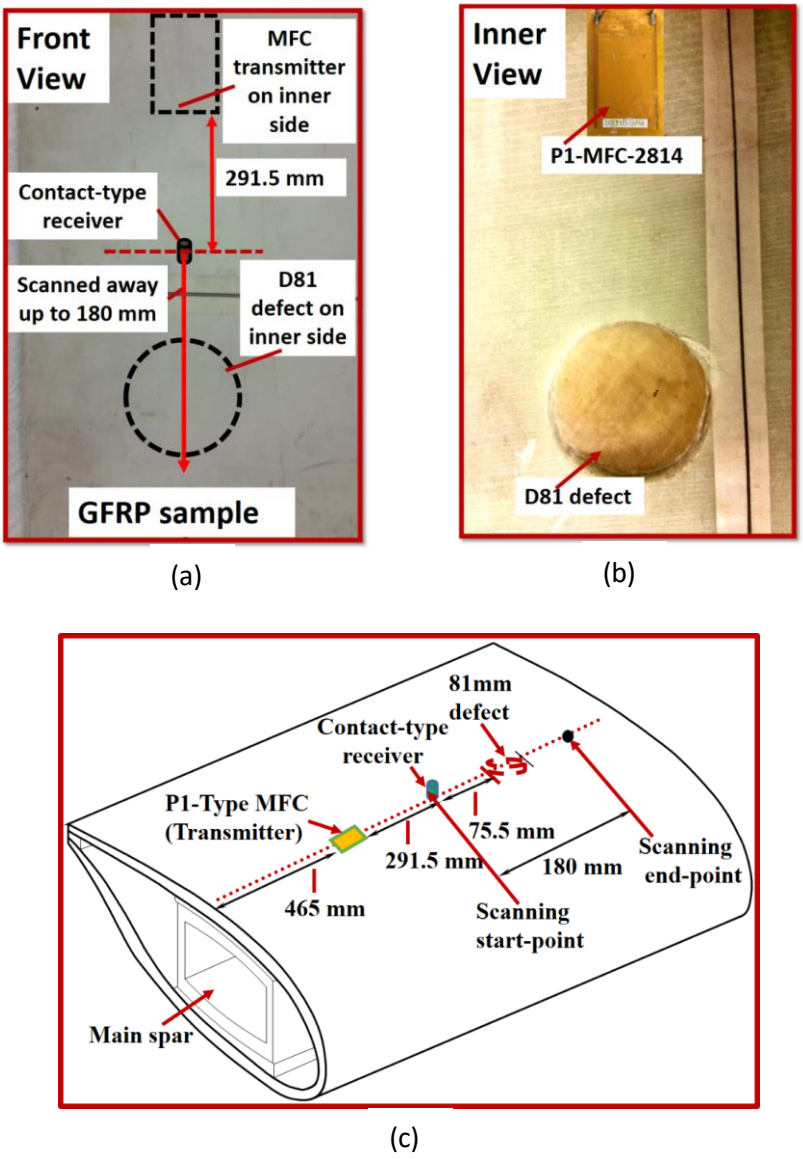

Fig. 4.2. Front view (a) and inner view (b) of the GFRP sample showing an 81 mm defect, P1-MFC transmitter and contact-type receiver; the complete arrangement of transducers and their position on the sample (c) (51)

A 43 kHz, 3-period sinusoidal burst signal was used to excite the glued MFC transducer and the contact-type receiver attached to a mechanical unit was scanned away. The selection of 43 kHz as an excitation frequency for the P1-type MFC transducer was based on resonance. In Chapter 3, it was observed that the resonant frequency of P1-type MFC transducer is closer to 43 kHz. The LF ultrasonic system developed by the Ultrasound Research Institute of Kaunas University of Technology was used in the experiment. The parametric specifications of LF ultrasonic system have already been presented in Table 2.3 (see Section 2.2 for details). In order to maintain an appropriate acoustic coupling, glycerol was used. The scanning distance and step was 180 mm and 0.2 mm, respectively. Total 901 signals were recorded at a sampling frequency of 100 MHz to be processed by the data acquisition system. In order to increase the signal-to-noise ration and compensating the noise and interference due to electrical/electronic circuity, the received signal was averaged eight times. The experimental schematic and recorded data in terms of a B-scan image are shown in Fig. 4.3a and Fig. 4.3b, respectively.

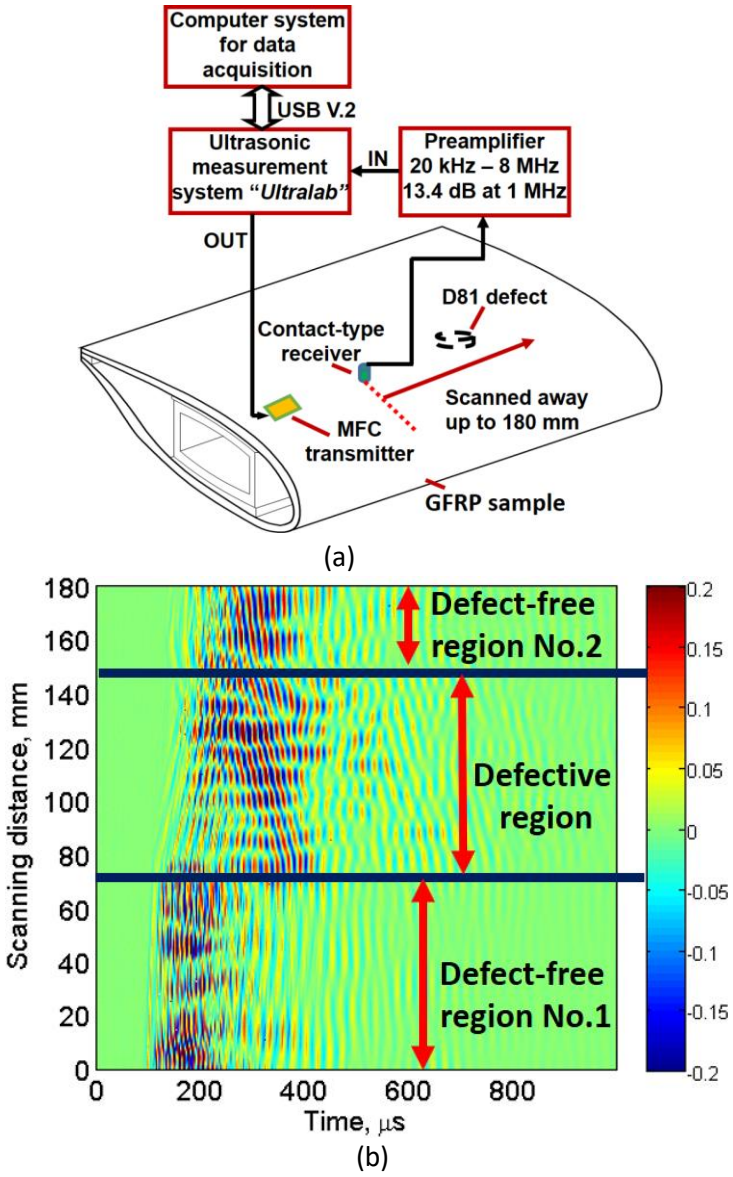

Fig. 4.3. A schematic of experimental analysis of GFRP sample using LF ultrasonic system (a) and the recorded B-scan image (b) (51)

The parameters such as velocity, time-of-arrival or amplitudes of GW signals may vary in the defective region as compared to the defect-free region due to the change in thickness. It should be noted that the distance between a transmitter and receiver is continuously changing in comparison to a fixed distance of 50 mm between transmitter and receiver during the experimental investigation on the trailing edge as

presented in Section 2.2. The scattering, attenuation and considerable alteration of GWs can be clearly detected as the wave propagates from the defect-free region into the defective region. However, the location and size of the 81 mm defect cannot be estimated from the B-scan image (Fig. 4.3b) without an appropriate signal processing approach.

4.3 Signal processing

4.3.1 Wavelet denoising and defect-estimations

The B-scan signal (Fig. 4.3b) is denoised by DWT. The Daubechies mother wavelet db8 is used to decompose signals into 8 levels. Order 8 of Daubechies wavelet is selected on the basis of correlation as described in Section 2.3.1. The soft-threshold is used to discard the coefficients with a universal threshold. The denoised B-scan image in the time range of 0–200 μs and in the spatial range 0–180 mm is shown in Fig. 4.4a. The defective region in the denoised B-scan (Fig. 4.4a) is more clearly visible as compared to the experimental B-scan (Fig. 4.3b). Recent research works on GW testing of composites by using contact-type transducers demonstrate how the *out-of-plane* (A_0 waves) GW could scatter, reflect and disperse; moreover, their amplitude could reduce significantly in the region of defects (32, 55, 175, 201). Therefore, amplitude detection can be very effective.

It should be noted that the average value of a defect-free signal was subtracted from all A-scans in Section 2.3.1 (see eq. 2.1). However, in this case, the distance between the transmitter and receiver is continuously changing (transmitter is fixed and receiver is scanned away) as compared to the measurement technique based on short-distance GWs. Therefore, the amplitude detection technique is applied without subtracting the average value of the defect-free signal from all denoised A-scans.

By using the Eq. 2.2 and Eq. 2.3, the normalized peak-to-peak amplitudes of all signals (A-scans) of a denoised B-scan signal (Fig. 4.4a) along the scanned distance is plotted and presented in Fig. 4.4b. The threshold of 0.707 (-3 dB) for the identification of size and location of 81 mm defect was applied in Fig. 4.4b. If x_1 and x_2 are the -3 dB points on the amplitude characteristics as shown in Fig. 4.4b, the location (distance from the first scanned point) and size of 81 mm defect can be estimated as follows:

$$Location\ of\ 81\ mm\ defect = x_2 \tag{4.1}$$

$$Size\ of\ 81\ mm\ defect = x_2 - x_1 \tag{4.2}$$

The estimated value of location and size of the 81 mm defect was 74.55 mm and 89.5 mm, respectively, with the corresponding absolute error in the measurement of 0.95 and 8.5 mm, respectively, (55). Irrespective of such errors in measurement, this technique proposes an economical pitch-catch technique with a single MFC and a contact-type transducer for ultrasonic NDT of large structures. Moreover, errors can

be reduced by developing a contact-type transducer with a center frequency closer to the MFC transducer, by developing a more effective signal processing approach, etc. which could be the motivation for further research.

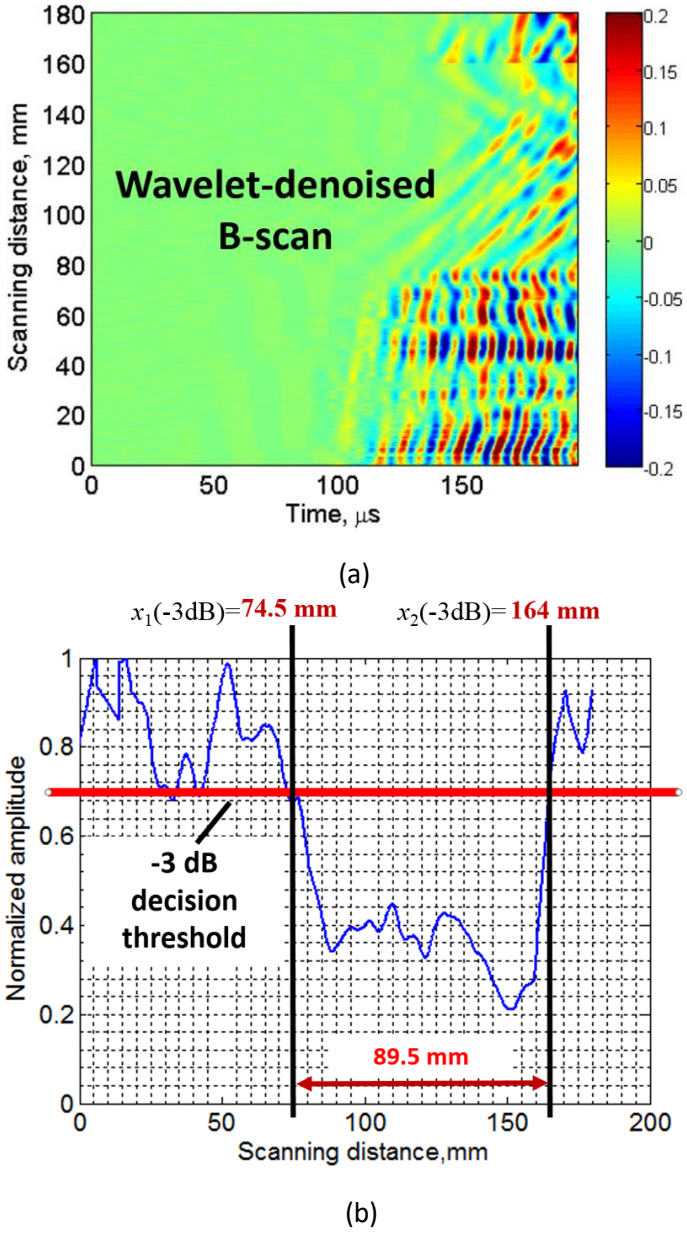

Fig. 4.4. Denoised B-scan after DWT (a) and amplitude detection process (b) (51)

4.3.2 Estimation of GW characteristics by using two-dimensional Fourier transform, variational mode decomposition and Hilbert transform

In some cases, it is not possible to calculate the phase velocities of the dominant wave mode (A_0 mode in this case) by calculating the dispersion curves using 2D-FFT. In order to improve the accuracy, back-reflected radiations and scattered signals from the opposite sides of sample the can be suppressed by using 2D-FFT. Hence, the 2D-FFT was applied to the experimental B-scan signal. In the next step, the signals that may be reflected from the edge of the other side of the object were filtered out. The inverse Fast-Fourier transform (2D-IFFT) was applied to reconstruct the B-scan only from direct waves. The process is described in detail in the previous work (202, 203). After filtering out the reflected waves the modified B-scan is shown in Fig. 4.5.

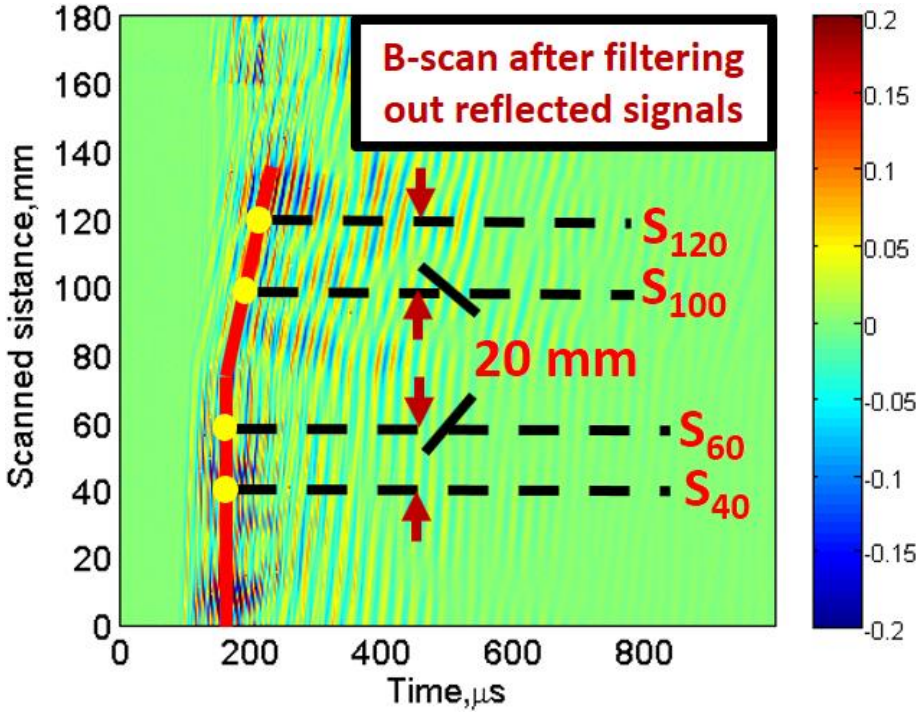

Fig. 4.5. B-scan image containing only direct waves (51).

In order to proceed with the estimation of time-of-arrival and phase velocities, two A-scan signals separated by a fixed distance in the defect-free and defective regions were considered. In the defect-free region, two signals (S40 and S60) at a scanned distance of 40 mm and 60 mm, respectively, were selected. Similarly, the two signals in the 81 mm defective regions were selected at a distance of 100 mm and 120 mm (S100 and S120). In both cases, there is a fixed spatial separation of 20 mm between acquisition points of the two signals (Fig. 4.5).

The next step is the application of mode decomposition for the reduction of coherent noise and mode-mixing from each of the four A-scans. The VMD decomposition technique (see Section 1.6.3.2 for details) was used to decompose all four A-scan signals into their six corresponding IMFs as shown in Fig. 4.6a-d. Initially, a uniformly distributed center frequency for each mode is assumed. A total of 500 iterations with convergence tolerance of (1×10^{-7}) were used in the process. Fig. 4.6 clearly shows that most of the noisy and HF components are contained by IMF3-6. Moreover, only IMF1-2 showed considerable correlation with the original signals in terms of power spectral density. Hence, the new signals are regenerated by adding the IMF1 and IMF2 in each of the four cases. The new reconstructed signals are denoted as S40', S60', S100' and S120' (55).

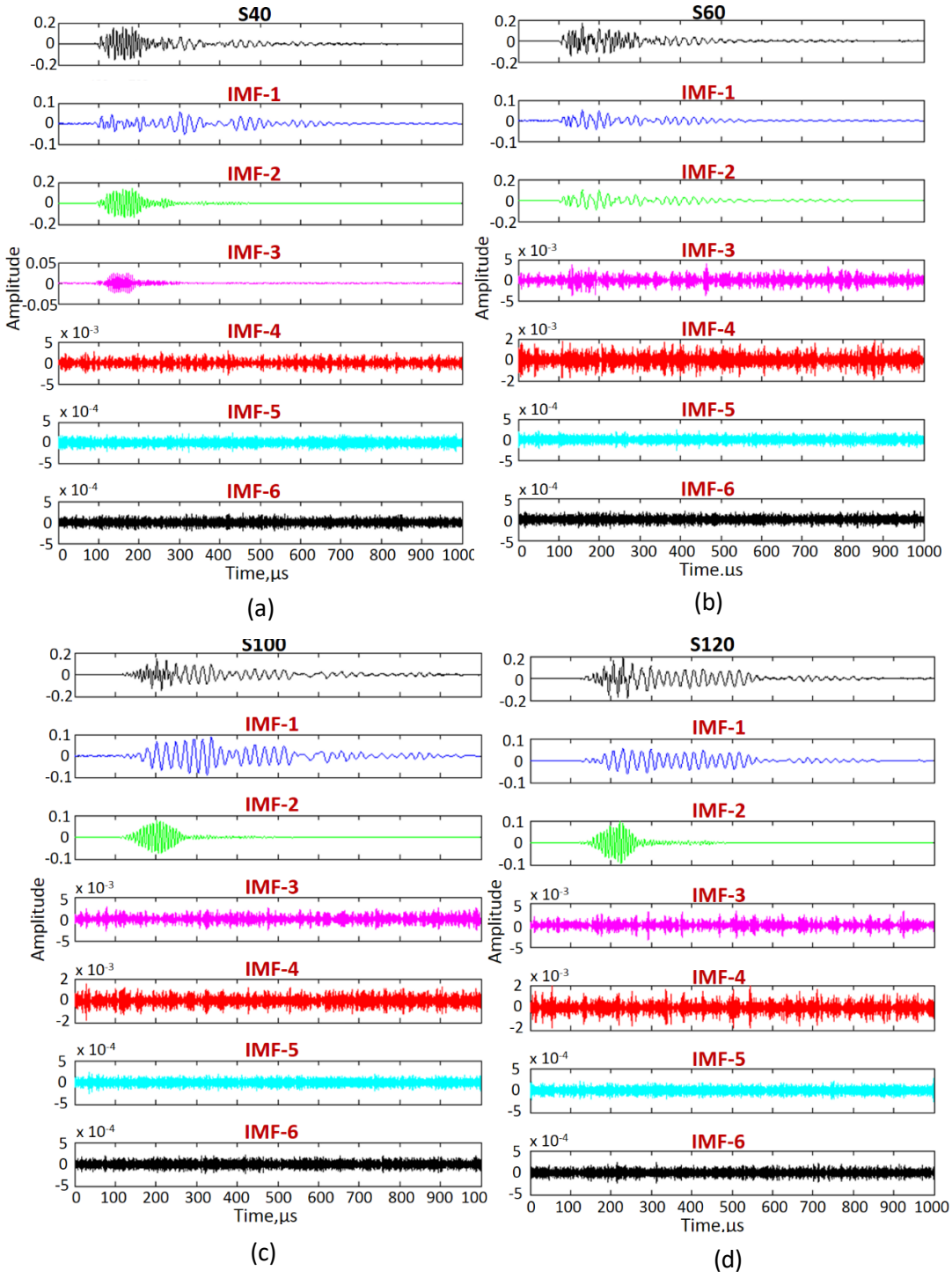

Fig. 4.6. VMD decomposition of defect-free signals at a distance of 40 mm (a) and 100 mm (b) and defective signals at distance 100 mm (c) and 120 mm (d) S40 (51).

The instantaneous amplitudes of all four reconstructed signals (S40', S60', S100' and S120') are calculated by using the Hilbert Transform as described in Chapter 1.6. Afterward, normalized peak-to-peak amplitudes are calculated by using Eq. 2.2 and Eq. 2.3. The next step is to compare the normalized amplitudes of the signal pairs in the defect-free (S40' and S60') and defective (S100' and S120') regions with respect to time.

The time-instantaneous amplitude characteristics are presented in Fig. 4.7a, b. After applying a threshold of -3 dB, the time delays between two signals t_{d1} (in case of S40' and S60') and t_{d2} (in case of S100' and S120') can be estimated as follows.

- If t_1 and t_2 are the -3 dB points on time-amplitude characteristics of the defect-free signals (Fig. 4.7a), and t_3 and t_4 are the -3 dB points on time-amplitude characteristics of the defective signals (Fig. 4.7b), the time delays between two signals can be calculated as:

$$t_d1 = t_2 - t_1 \tag{4.3}$$

$$t_d2 = t_4 - t_3 \tag{4.4}$$

Where td1 is the time-delay between two signals (S40', S60') in the defect-free region and td2 is the time-delay between two signals (S100', S120') in the defective region.

The estimated values of t_{d1} and t_{d1} were obtained as 13.5 μs and 19.8 μs, respectively. As there was a fixed distance of 20 mm between two signals in the defect-free and defective regions, the phase velocity (approximated value) can be calculated by dividing the distance by time. The calculated value of phase velocity of GW in the defect-free region is 1482 m/s which decreases significantly in the defective region with a phase velocity of 1010 m/s.

In order to verify the measured phase velocities, the theoretical calculation of the phase velocities of the propagating GW modes was performed by the semi-analytical finite element (SAFE) method (197, 198, 199, 200). The properties of GFRP material are already presented in Table 2.2 (see Chapter 2.2.1 for details). The thickness of different layers in the defect-free region is illustrated in Table of the GFRP sample are similar to those presented in Table 3.3 (see Chapter 3.4.6 for details).

The thickness of the sample in the defect-free region was considered as 22 mm whereas 3.5 mm was selected for the defective region. These values are the intermediate values of the real sample in the defect-free and defective regions. The simulation results are presented in Fig. 4.8a, b. In the defect-free region, the phase velocity of the dominant *out-of-plane* A_0 mode was observed as 1253 m/s whereas, the phase velocity in the defective region was calculated as 745 m/s (55).

In comparison to the results obtained by the SAFE method, results obtained by the signal processing methods are slightly different in absolute values but similar in velocity decrease over the defective region as compared to the defect-free region. The possible issues and limitations of the proposed signal processing approach and causes of differences in obtained results by the proposed signal processing algorithm and SAFE method are discussed in the Conclusions (Section 4.4) of this Chapter.

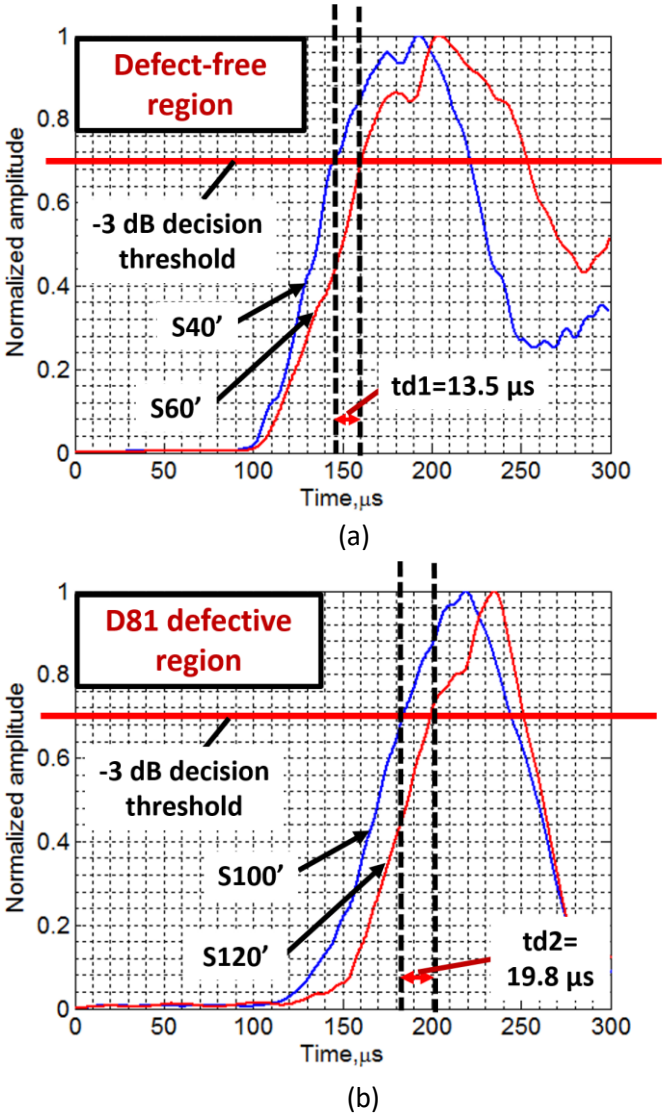

Fig. 4.7. Instantaneous amplitude characteristics of signal pairs (S40' and S60') in the defect-free region (a) and (S100' and S120') in the 81 mm defective region (b) (51).

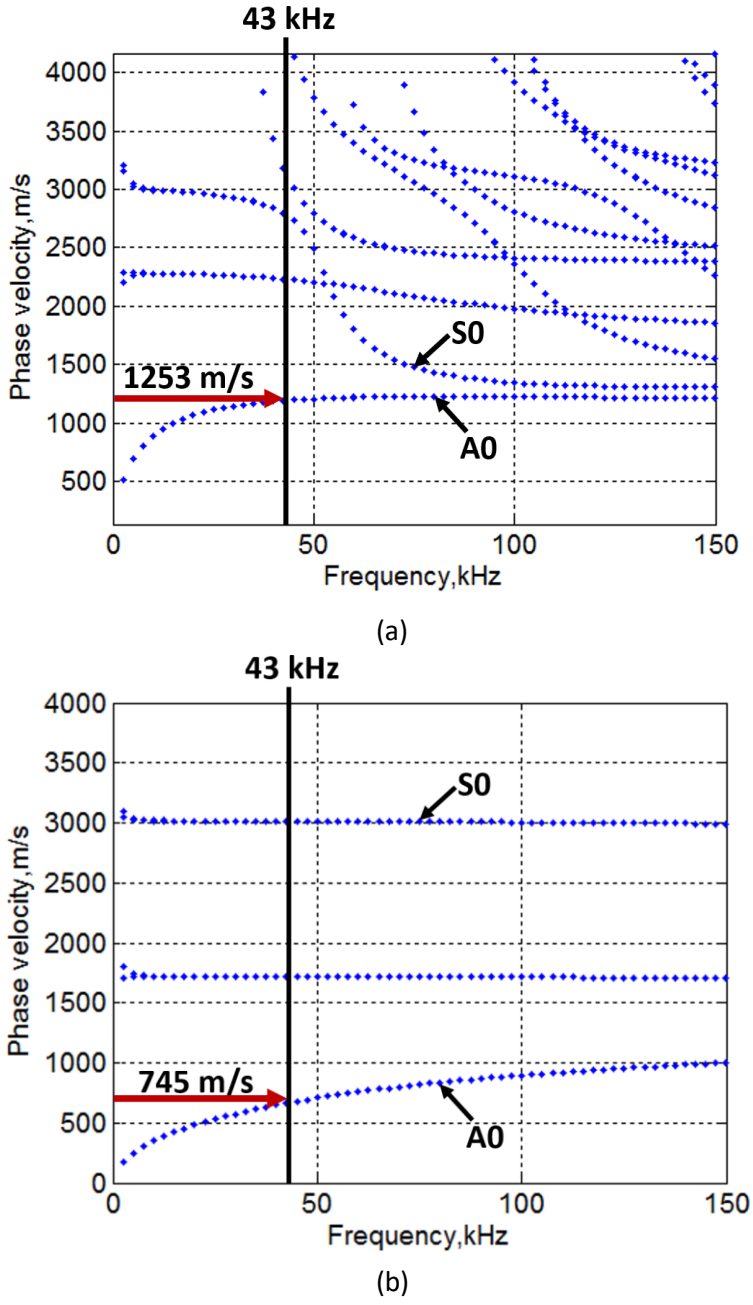

Fig. 4.8. Phase velocity dispersion characteristics by using the SAFE method: defect-free (**a**) and defective region (b) (51).

4.4 Conclusions

The detailed conclusions of the Chapter along with the limitations and issues associated with the proposed techniques are:

1. A pitch-catch based economical measurement technique has been developed to estimate defects in large composite structures using long-distance guided waves. A P1-type MFC transducer is used as a transmitter and a contact-type receiver is used for the experimental analysis of a GFRP sample. i.e. a segment of WTB. After successfully detecting an 81 mm defect located on the main spar of the segment, signal processing techniques are applied to estimate defect features and instantaneous characteristics of the guided waves.
2. The size and location of the defect are estimated by reducing the structural noise using DWT. Afterward, the size and location of the defect are calculated by applying the peak-to-peak amplitude detection technique with a decision threshold of -3dB.
3. The application of 2D-FFT is proposed to filter out the reflections from the opposite edge before calculating the instantaneous characteristics of the GW signals using VMD and HT. The estimation of phase velocities and time-of-arrivals is also proposed based on instantaneous characteristics. The 2D-FFT was applied to filter out the reflections from the opposite edge. The measured phase velocity of the propagating A_0 waves is compared with the SAFE method. There was a significant difference in the measured phase velocities and the SAFE method. However, it should be noted that the thickness of the sample was considered as fixed in the case of SAFE simulations. On the other hand, the thickness of the real sample was not fixed in both defect-free and defective regions. Moreover, the possible wave mechanism with the interaction of GWs with defects such as mode conversions, scattering, reflections was not considered in the SAFE method.
4. The reproducibility of the results depends on the variations of signal amplitudes in the defect-free and defective regions. The accuracy also depends on the selection of -3dB threshold or peak-to-peak values of amplitudes. Moreover, the amplitude-based estimations are very sensitive to noise and variations of the environmental conditions. Thus the ambient temperature of 25℃ was maintained during the experiments.
5. The proposed technique can be improved by using a different contact-type transducer with a center frequency closer to the MFC transducer and improving the signal processing techniques. However, the proposed technique provides motivation to develop a cost-effective measurement technique for inspecting large composite structures.

5. OVERALL RELIABILITY IN DEFECT ESTIMATION

This Chapter deals with the amount of uncertainty presented in the experimental investigation of defects in the process of calculating the size and location of defects in the GFRP sample by using experimental analysis and adaptation of various signal processing techniques. Therefore, the calculation of uncertainty in each measurement technique (short and long distance GW testing) comprises of uncertainty in the measurement and the uncertainty due to the application of signal processing techniques.

The uncertainty in measurement depends on the measured value and several factors influencing the measurement (204). The evaluation of uncertainty results from an appropriate mathematical model and, in general, can be expressed as:

$$y = f(x_1, x_2 \ldots\ldots\ldots\ldots\ldots\ldots x_n) \quad (5.1)$$

where x_n (n=1,2…) are the input quantiles which influence the output quantity (y) and function f denotes the measurement process.

In the case of presented work to analyze the defect size and location, the statistical approach (type-A) cannot be applied for the calculation of measurement uncertainty because a single B-scan was acquired without repeating the measurement at the same points. The measurement was based on the estimation of time-of-arrival of A-scans at various points and their respective amplitudes. The time-of-arrival depends on the phase velocity of propagating wave modes which further depend on the thickness of the structure and excitation frequency. However, the amplitude of the waves depends on the excitation frequency, thickness of the structure, etc. Moreover, the decision level (-3 dB) is also one of the contributing factors in order to calculate the size and location of a defect in the signal processing approach. With the assumption that all possible parameters contribute independently, the sources of Type-B standard uncertainty in our measurement based on GWs are listed as follows:

- *The resolution of mechanical scanner used in the experiment (m):* The resolution of the mechanical scanner is 20µm and therefore the deviation is ±10µm.
- *The spatial resolution of contact-type transducers with a contact surface* (*c*)*:* The resolution of contact-type transducers is ±0.5 µm and therefore the uncertainty is ±0.25 µm.
- *The location of MFC transducer* (*s*)*:* In the Experimental Investigation No.2, the MFC transducer was glued on the structure. Uncertainty in this case is assumed as ±1 mm.
- *Excitation frequency* (*f*)*:* Excitation frequency of a transducer is selected in such a way that the defect size must be greater than λ/4 to λ/2. The frequency deviation is considered as ±25 kHz.

- *The thickness of acoustical contact (glycerol)* (*tc*)*:* This is approximately varied between 0.4 mm to 0.5 mm. In this case, deviation is considered as ±0.05 mm.
- *The optimal distance between transmitter and receiver* (*d*) *(only for experimental investigation No.1)*: The optimal distance between transducers was selected as 50 mm which basically lies between 5λ to 10λ. Deviation in this case is considered as ±2 mm.
- *The thickness of the sample in the defective region* (*td*): The thickness of the sample is not fixed in the defective region. In the case of defects located on the trailing edge of the sample (experimental investigation No.1), the thickness of the structure lies between 3 and 3.5 mm in the defective region. On the other hand, the thickness of the structure lies between 3 to 4 mm in the defective region of the main spar (experimental investigation No.2). Hence, the approximate deviation (from the mean value) is considered as ±0.75 mm and ±0.50 mm in the case of first and second experiments, respectively.
- *Quantization error* (*q*): The quantization error in case of 10-bit ADC with a 1V reference voltage is ±488 µV. The quantization error can be significantly reduced by using averaging techniques (205, 206). After considering the averaging of eight times, the quantization error reduces to ±61 µV.
- *Discretization interval* (*n*)*:* The rate of discretization for the sampling frequency 100 MHz is 10 ns and therefore deviation is ±5 ns.
- *Electrical noise* (*N*): Random electrical noise can be assumed as negligible after averaging the signals.
- *Uncertainty due to operating temperature*(*T*): The experiment was performed at room temperature (25 ºC ± 2 ºC).
- *Uncertainty due to -3 dB* (0.707) *threshold during signal processing* (*th*): The variance has been observed as ±0.25 mm.

The description of measurement uncertainties for the calculation of size/location of defects in the case of both measurement techniques is presented in Table 5.1 and 5.2, respectively. The weighting factors are selected depending on the priorities of individual sources and their respective measurement units.

Table 5.1. Uncertainties in measurement by short distance GW testing

S.N.	Source of uncertainty	Estimate	Probability distribution/divisor	Variance after distribution	Weightage factor, W_i
1	Resolution of scanner, *m*	±0.01 mm	Normal / 2	±0.005 mm	100 (1/1)
2	Resolution of contact-type transducers, *c*	±0.50 mm	Normal / 2	±0.25 mm	1 (1/1)
3	Excitation frequency, *f*	±25 kHz	Rectangular/ √3	±14.43 kHz	0.25 (mm/kHz)

4	Thickness of acoustical contact, *tc*	±0.05 mm	Normal / 2	±0.03 mm	1 (1/1)
5	The optimal distance between transducers, *d*	±2 mm	Normal / 2	±1 mm	1 (1/1)
6	The thickness of the defective region, *td*	±0.75 mm	Rectangular/ √3	±0.43 mm	10 (1/1)
7	Quantization error, *q*	±61 µV	Rectangular/ √3	±35 µV	0.01(mm/ µV)
8	Discretization interval, *n*	±0.005µs	Normal / 2	0.003 µs	10 (mm/ µs)
9	Temperature *T*	±2 ºC	Normal / 2	±1 ºC	0.1 (mm/ ºC)
10	Decision threshold of -3dB (0.707)	±0.1 mm	Normal / 2	±0.05 mm	10 (1/1)

Table 5.2. Uncertainties in measurement by using long-distance GW testing

S.N.	**Source of uncertainty**	**Estimate**	**Probability distribution/divisor**	**Variance after distribution (u_i)**	**Weightage factor (W_i)**
1	Resolution of scanner, *m*	±0.001 mm	Normal / 2	±0.005 mm	100 (1/1)
2	Resolution of contact-type transducers, *c*	±0.50 mm	Normal / 2	±0.25 mm	1 (1/1)
3	Location of MFC transducer, *s*	±1 mm	Normal / 2	±0.5 mm	1 (1/1)
4	Excitation frequency, *f*	±25 kHz	Rectangular/ √3	±14.43 kHz	0.25 (mm /kHz)
5	Thickness of acoustical contact, *tc*	±0.05 mm	Normal / 2	±0.03 mm	1 (1/1)
6	Thickness of the defective region, *td*	±0.5 mm	Rectangular/ √3	±0.29 mm	10(1/1)
7	Quantization error, *q*	±61 µV	Rectangular/ √3	±35 µV	0.01 (mm / µV)
8	Discretization interval, *n*	±0.005 µs	Normal / 2	±0.003 µs	10 (mm / µs)
9	Temperature *T*	±2ºC	Normal / 2	±1 ºC	0.1 (mm / ºC)
10	Decision threshold of -3dB (0.707)	±0.1mm	Normal / 2	±0.05 mm	10 (1/1)

Following the assumption that all individual uncertainties are independent from each other and the influence of all other sources is negligible in the calculation of combined standard uncertainty (u_{sE}), the combined standard uncertainty in the measurement of defect size or location is given by the following equations.
The combined standard uncertainty can be expressed as (204):

$$u_{sE} = \sqrt{\sum_{i=1}^{10}((W_i)^2 \cdot (u_i)^2} \tag{5.2}$$

where u_i and W_i ($i = 1, 2 \ldots 10$) are the respective variance and weighting factors of the individual sources of uncertainties, as presented in Table 5.1 and Table 5.2.

Hence, the combined standard uncertainty in size/location of defects is calculated as ±5.76 mm and ±5.82 mm in the case of first and second measurement technique, respectively.
The expanded uncertainty in the entire process is given by (204, 207):

$$U_{Exp} = k \cdot u_{sE} \tag{5.3}$$

where k is the coverage factor which is equal to 2 for normal distribution with the probability equal to 0.95.
The expanded uncertainty for the entire process (experimental and signal processing) is 11.52 and 11.64 mm for the measurement techniques based on short-distance and long-distance GWs, respectively.

The overall metrological characteristics of the presented measurement techniques can be summarized as follows (Table 5.3):

Table 5.3. Metrological characteristics of the presented techniques

S.N.	Parameters	Numerical value
1	Minimum detectable defect size ($\lambda/4$)	2 mm
2	Minimum measurable defect size (λ)	8 mm
3	Resolution	0.5 mm
4	Maximum range of inspection (short-distance GW testing)	1 m
5	Maximum range of inspection (long-distance GW testing)	3–5 m

GENERAL CONCLUSIONS

1. In this dissertation, two ultrasonic measurement techniques based on short-distance and long-distance guided wave propagation are proposed for the detection and estimation of disbond-type defects in small and large multi-layered composite structures, respectively. A segment of wind turbine blade constructed from GFRP material has been selected for the investigation which contained disbond-type defects of 15 to 81 mm in diameters at different locations. In comparison to the commercially used pulse-echo and phased-array technique of inspection, the ultrasonic pitch-catch method is used in both proposed measurement techniques which is more flexible in comparison to the pulse-echo method and less complex and more cost-effective than phased-array method. All defects were successfully detected by the developed techniques. The signal processing methods based on discrete wavelet transform are utilized to remove non-stationary structural noise. Afterward, an amplitude detection technique with a -3 dB threshold is applied to locate and size the defect. The size and location of defects with 15 and 25 mm diameters investigated by short-distance GWs are measured with a measurement uncertainty of ±5.76 mm. On the other hand, the size and location of defects with 81 mm diameter investigated by long-distance GWs are measured with a measurement uncertainty of ±5.82 mm.
2. The measurement technique based on short-distance guided waves was performed by using a special configuration of two contact-type transducers as a transmitter-receiver pair, fixed on a moving panel and operating in a pitch-catch mode. The configuration is well suited for automatic NDT. There was a fixed separation distance of 50 mm between the two transducers. By keeping the fixed distance between the transducers, the dispersion, attenuation and scattering due to variable distance can be reduced. On the other hand, the P1-type MFC transducer as a transmitter and a contact-type piezoceramic transducer as a receiver is used to develop a measurement technique based on guided waves propagating to a long distance.
3. In order to estimate the instantaneous characteristics of GWs, we propose to compare the power spectral densities of intrinsic mode functions with the original signal after mode decomposition. In this way, the best intrinsic modes can be selected to regenerate the signals before estimating the instantaneous amplitude and frequency characteristics of guided waves by using the Hilbert transform. We also propose to filter out the reflections from the opposite edge by using 2D-FFT in the case of complex structures (more reflections and noise in an ultrasonic B-scan), before applying mode decomposition techniques.
4. Since the MFC transducer is a small, thin and flexible transducer, we propose to estimate its 3D displacement characteristics in order to confirm its accuracy and feasibility for NDT of structures. The novel 2D analytical model for the estimation of directivity patterns of contact-type transducers in the generation of guided waves is also developed. This model can predict the directivity

pattern of a contact-type ultrasonic transducer or a configuration of transducers in any medium, at any excitation frequency, at any distance with known dispersive characteristics. The developed model can provide information about the appropriate excitation frequency for a transmitter, the dominant wave modes, placement of transducers, etc. Moreover, this model reduces a significant amount of computation time spent on numerical modelling and experimental analysis for directivity estimation.

MOTIVATIONS FOR THE FUTURE SCOPE

The proposed methods can contribute to real-time applications in the field of ultrasonic non-destructive testing. However, there is a scope for future research in order to improve the practical adaptability of the developed techniques and methodologies:

- The three-dimensional displacement characteristics of an unloaded transducer could provide information to discard the faulty transducers. However, there is a scope to compare the displacement characteristics of an unloaded transducer to the transducer embedded in metallic and composite structures.
- The results obtained by the developed 2D analytical model and the experimental results showed a significant coincidence and similarities. However, a considerable difference in the size of minor lobes of directivity patterns was observed, which is related to the approximated value of the amplitude correction factor used in the analytical model to decrease complexity. In future research, the results can be further improved by including a more accurate value of amplitude correction factor.
- The measurement techniques based on the combination of contact and non-contact ultrasonic methods can be developed to increase the accuracy of defect estimation.
- The results obtained by signal processing algorithms were based on the amplitude variations with time and space. The signal processing algorithm based on other parametric estimations rather than amplitudes can be developed. Moreover, the estimation and characterization of defects depend on the A_0 mode waves with a dominant *out-of-plane* component, the reception of which was performed by high sensitivity contact-type receiver. In future work, the algorithm can be improved and validated for the S_0 waves.

REFERENCES

1. CAWLEY, P. and ADAMS, R.D. Defect Types and Non-Destructive Testing Techniques for Composites and Bonded Joints. *Materials Science and Technology*, 05/01, 1989, vol. 5, no. 5. pp. 413-425 ISSN 0267-0836.

2. CHUNG, D.D.L. Composite Materials: Functional Materials for Modern Technologies D.D.L. CHUNG ed., London: Springer London, 2003 *Applications of Composite Materials*, pp. 1-13 ISBN 978-1-4471-3732-0.

3. SHINJI, O. Flexural Properties of Long Bamboo Fiber/ PLA Composites. *Open Journal of Composite Materials*, 2015, vol. 5. pp. 70-78 ISSN 2164-5655.

4. MRAZOVA, M. Advanced Composite Materials of the Future in Aerospace Industry. *INCAS Bulletin*, 2013, vol. 5, no. 3. pp. 139-150 ISSN 2066-8201.

5. XU, B. and LI, H.Y. *Advanced Composite Materials and Manufacturing Engineering: Selected Peer Reviewed Papers from the 2012 International Conference on Advanced Composite Materials and Manufacturing Engineering (Cmme2012).* Trans Tech Publication, 2012 ISBN 9783037855225.

6. CALLISTER JR., W.D. *Materials Science and Engineering: An Introduction, 7th Edition.* 7th ed. N.Y., U.S.A.: Wiley, Jan, 2006 ISBN 978-0-4717-3696-7.

7. Tiwari, K., Raisutis,R. Comparative Analysis of Non-Contact Ultrasonic Methods for Defect Estimation of Composites in Remote Areas. *CBU International Conference Proceedings*. 2016th ed., 2016, vol. 4. pp. 846-851 ISSN 1805-9961.

8. KUDVA, J.N., GRAGE, M.J. and ROBERTS, M.M. Structural health monitoring 2000 : proceedings of the 2nd International Workshop on Structural Health Monitoring, Stanford University, Stansford, CA F.K. CHANG ed., 1st ed. Lancaster: CRC Press, September 8-10, 1999., 1999 *Aircraft Structural Health Monitoring and Other Smart Structures Technologies-Perspectives on Development of Smart Aircraft*, pp. 122-132 worldcat. ISBN 9781566768818.

9. BAR-COHEN, Y. Emerging NDE Technologies and Challenges at the Beginning of the 3 Rd Millennium--Part II, Part I. *NDT.Net*, 2000, vol. 5, no. 2. pp. 141-150 ISSN 1435-4934.

10. KOŁAKOWSKI, P. Structural Health Monitoring – a Review with the Emphasis on Low-Frequency Methods. *Engineering Transactions*, 2014, vol. 55, no. 3. pp. 239-275 ISSN 2450-8071.

11. OCHÔA, P., INFANTE, V., SILVA, J.M. and GROVES, R.M. Detection of Multiple Low-Energy Impact Damage in Composite Plates using Lamb Wave Techniques. *Composites Part B: Engineering*, October 2015, 2015, vol. 80. pp. 291-298. Available from:

http://www.sciencedirect.com/science/article/pii/S135983681500373X ISSN 1359-8368. DOI https://doi.org/10.1016/j.compositesb.2015.06.010.

12. SU, Z. and YE, L. *Identification of Damage using Lamb Waves: From Fundamentals to Applications*. 1st ed. London: Springer-Verlag, 2009 ISBN 978-1-84882-783-7.

13. FARRAR, C.R. and WORDEN, K. New Trends in Vibration Based Structural Health Monitoring A. DERAEMAEKER and K. WORDEN eds., Vienna: Springer Vienna, 2010 *An Introduction to Structural Health Monitoring*, pp. 1-17 ISBN 978-3-7091-0399-9.

14. WILCOX, P.D., KONSTANTINIDIS, G., CROXFORD, A.J. and DRINKWATER, B.W. *Strategies for Guided Wave Structural Health Monitoring*. London ed. AIP, 2007 ISBN 0094-243X. DOI 10.1063/1.2718139.

15. RAGHAVAN, A. and CESNIK, C.E. Review of Guided-Wave Structural Health Monitoring. *The Shock and Vibration Digest*, 2007, vol. 39, no. 2. pp. 91-114.

16. ROSE, J.L. Ultrasonic Guided Waves in Structural Health Monitoring. *Key Engineering Materials*, 2004, vol. 270-273. pp. 14-21 ISSN 1662-9795.

17. MICHAELS, J.E., DAWSON, A.J., MICHAELS, T.E. and Massimo Ruzzene. *Approaches to Hybrid SHM and NDE of Composite Aerospace Structures*. KUNDU, Tribikram ed., SPIE, 9 March, 2014 ISBN 9780819499905. DOI 10.1117/12.2045172.

18. OSTIGUY, P., QUAEGEBEUR, N. and MASSON, P. Non-Destructive Evaluation of Coating Thickness using Guided Waves. *NDT & E International*, December 2015, 2015, vol. 76. pp. 17-25. Available from: http://www.sciencedirect.com/science/article/pii/S0963869515000869 ISSN 0963-8695. DOI https://doi.org/10.1016/j.ndteint.2015.08.004.

19. ROSE, J.L. Successes and Challenges in Ultrasonic Guided Waves for NDT and SHM. *Materials Evaluation*, May 2010, 2010, vol. 68, no. 5. pp. 494-500 ISSN 0025-5327.

20. DELRUE, S. and VAN DEN ABEELE, K. Detection of Defect Parameters using Nonlinear Air-Coupled Emission by Ultrasonic Guided Waves at Contact Acoustic Nonlinearities. *Ultrasonics*, December 2015, 2015, vol. 63. pp. 147-154. Available from: http://www.sciencedirect.com/science/article/pii/S0041624X15001699 ISSN 0041-624X. DOI https://doi.org/10.1016/j.ultras.2015.07.001.

21. CLARKE, T., CAWLEY, P., WILCOX, P. D., CROXFORD, A. J. Evaluation of the Damage Detection Capability of a Sparse-Array Guided-Wave SHM System Applied to a Complex Structure Under Varying Thermal Conditions. *IEEE Transactions on Ultrasonics, Ferroelectrics, and Frequency Control*, 2009, vol. 56, no. 12. pp. 2666-2678 ISSN 0885-3010.

22. CAWLEY, P. *Practical Guided Wave Inspection and Applications to Structural Health Monitoring.* MARTIN, V., et al ed., Brisbane, Australia ed. Brisbane: Engineers Australia, 10-12 December, 2007, 2007 ISBN 0 8582 5862 5.

23. RATHOD, V.T. and ROY MAHAPATRA, D. Ultrasonic Lamb Wave Based Monitoring of Corrosion Type of Damage in Plate using a Circular Array of Piezoelectric Transducers. *NDT & E International*, November 2011, 2011, vol. 44, no. 7. pp. 628-636. Available from: http://www.sciencedirect.com/science/article/pii/S0963869511000910 ISSN 0963-8695. DOI https://doi.org/10.1016/j.ndteint.2011.07.002.

24. SHARMA, A., SHARMA, S., SHARMA, S. and MUKHERJEE, A. *Ultrasonic Guided Waves for Monitoring Corrosion of FRP Wrapped Concrete Structures.* , 15 October 2015, 2015 Available from: http://www.sciencedirect.com/science/article/pii/S095006181530297X ISBN 0950-0618. DOI https://doi.org/10.1016/j.conbuildmat.2015.08.084.

25. LU, Y., LI, J., YE, L. and WANG, D. *Guided Waves for Damage Detection in Rebar-Reinforced Concrete Beams.* , October 2013, 2013 Available from: http://www.sciencedirect.com/science/article/pii/S0950061813004145 ISBN 0950-0618. DOI https://doi.org/10.1016/j.conbuildmat.2013.05.016.

26. WILLEY, C.L., SIMONETTI, F., NAGY, P.B. and INSTANES, G. *Guided Wave Tomography of Pipes with High-Order Helical Modes.* , July 2014, 2014 Available from: http://www.sciencedirect.com/science/article/pii/S0963869514000449 ISBN 0963-8695. DOI https://doi.org/10.1016/j.ndteint.2014.03.010.

27. LØVSTAD, A. and CAWLEY, P. *The Reflection of the Fundamental Torsional Guided Wave from Multiple Circular Holes in Pipes.* , November 2011, 2011 Available from: http://www.sciencedirect.com/science/article/pii/S0963869511000715 ISBN 0963-8695. DOI https://doi.org/10.1016/j.ndteint.2011.05.010.

28. LEINOV, E., LOWE, M.J.S. and CAWLEY, P. *Investigation of Guided Wave Propagation and Attenuation in Pipe Buried in Sand*. , 7 July 2015, 2015 Available from: http://www.sciencedirect.com/science/article/pii/S0022460X1500190X ISBN 0022-460X. DOI https://doi.org/10.1016/j.jsv.2015.02.036.

29. MUSTAPHA, S. and YE, L. *Propagation Behaviour of Guided Waves in Tapered Sandwich Structures and Debonding Identification using Time Reversal.* , September 2015, 2015 Available from: http://www.sciencedirect.com/science/article/pii/S0165212515000529 ISBN 0165-2125. DOI https://doi.org/10.1016/j.wavemoti.2015.03.010.

30. PUTKIS, O., DALTON, R.P. and CROXFORD, A.J. The Anisotropic Propagation of Ultrasonic Guided Waves in Composite Materials and Implications for Practical Applications. *Ultrasonics*, February 2016, 2016, vol. 65. pp. 390-399. Available from: http://www.sciencedirect.com/science/article/pii/S0041624X14003436 ISSN 0041-624X. DOI https://doi.org/10.1016/j.ultras.2014.11.013.

31. CASTAINGS, M., SINGH, D. and VIOT, P. *Sizing of Impact Damages in Composite Materials using Ultrasonic Guided Waves.* , March 2012, 2012 Available from: http://www.sciencedirect.com/science/article/pii/S0963869511001460 ISBN 0963-8695. DOI https://doi.org/10.1016/j.ndteint.2011.10.002.

32. RAIŠUTIS, R., KAŽYS, R., ŽUKAUSKAS, E. and MAŽEIKA, L. *Ultrasonic Air-Coupled Testing of Square-Shape CFRP Composite Rods by Means of Guided Waves.* , November 2011, 2011 Available from: http://www.sciencedirect.com/science/article/pii/S0963869511000909 ISBN 0963-8695. DOI https://doi.org/10.1016/j.ndteint.2011.07.001.

33. DENG, Q. and YANG, Z. *Propagation of Guided Waves in Bonded Composite Structures with Tapered Adhesive Layer.* , November 2011, 2011 Available from: http://www.sciencedirect.com/science/article/pii/S0307904X11002897 ISBN 0307-904X. DOI https://doi.org/10.1016/j.apm.2011.04.042.

34. MASSEREY, B., RAEMY, C. and FROMME, P. *High-Frequency Guided Ultrasonic Waves for Hidden Defect Detection in Multi-Layered Aircraft Structures.* , September 2014, 2014 Available from: http://www.sciencedirect.com/science/article/pii/S0041624X14001140 ISBN 0041-624X. DOI https://doi.org/10.1016/j.ultras.2014.04.023.

35. PUTHILLATH, P. and ROSE, J.L. *Ultrasonic Guided Wave Inspection of a Titanium Repair Patch Bonded to an Aluminum Aircraft Skin.* , October 2010, 2010 Available from: http://www.sciencedirect.com/science/article/pii/S0143749610000667 ISBN 0143-7496. DOI https://doi.org/10.1016/j.ijadhadh.2010.05.008.

36. GHOLIZADEH, S. *A Review of Non-Destructive Testing Methods of Composite Materials.* , 2016, 2016 Available from: http://www.sciencedirect.com/science/article/pii/S2452321616000093 ISBN 2452-3216. DOI https://doi.org/10.1016/j.prostr.2016.02.008.

37. LIU, G.R., LAM, K.Y. and SHANG, H.M. Scattering of Waves by Flaws in Anisotropic Laminated Plates. *Composites Part B: Engineering*, 1996, 1996, vol. 27, no. 5. pp. 431-437. Available from: http://www.sciencedirect.com/science/article/pii/1359836896000091 ISSN 1359-8368. DOI https://doi.org/10.1016/1359-8368(96)00009-1.

38. CASTAINGS, M. and HOSTEN, B. Guided Waves Propagating in Sandwich Structures made of Anisotropic, Viscoelastic, Composite Materials. *The Journal of the Acoustical Society of America*, May, 2003, vol. 113, no. 5. pp. 2622-2634 ISSN 0001-4966; 0001-4966.

39. JU, T.H. and DATTA, S.K. Review of Progress in Quantitative Nondestructive Evaluation: Volume 10B D.O. THOMPSON and D.E. CHIMENTI eds., Boston, MA: Springer US, 1991 *Scattering of Impact Wave by a Crack in Composite Plate*, pp. 1515-1522 ISBN 978-1-4615-3742-7.

40. WORDEN, K., FARRAR, C.R., MANSON, G. and PARK, G. The Fundamental Axioms of Structural Health Monitoring. *Proceedings of the Royal Society A: Mathematical, Physical and Engineering Science*, The Royal Society, 2007, vol. 463, no. 2082. pp. 1639-1664. Available from: http://rspa.royalsocietypublishing.org/content/463/2082/1639.abstract DOI 10.1098/rspa.2007.1834.

41. KONSTANTINIDIS, G., DRINKWATER, B.W., WILCOX, P.D. The Temperature Stability of Guided Wave Structural Health Monitoring Systems. *Smart Materials and Structures*, 2006, vol. 15, no. 4. pp. 967-976 ISSN 0964-1726.

42. CROXFORD, A.J., MOLL, J., WILCOX, P.D. and MICHAELS, J.E. *Efficient Temperature Compensation Strategies for Guided Wave Structural Health Monitoring.* , April 2010, 2010 Available from: http://www.sciencedirect.com/science/article/pii/S0041624X09001826 ISBN 0041-624X. DOI https://doi.org/10.1016/j.ultras.2009.11.002.

43. KONSTANTINIDIS, G., WILCOX, P. D., DRINKWATER, B.W. An Investigation into the Temperature Stability of a Guided Wave Structural Health Monitoring System using Permanently Attached Sensors. *IEEE Sensors Journal*, 2007, vol. 7, no. 5. pp. 905-912 ISSN 1530-437X.

44. JUNGERT, A. *Damage Detection in Wind Turbine Blades using Two Different Acoustic Techniques*. Stuttgart, Germany ed. NDT.net - The e-Journal of Nondestructive Testing, Sep 11-13, 2008, 2008.

45. *Application-Specific, Low-Frequency Phased Array Probes and Holders for the Inspection of GFRM and CFRM Wind Turbine Blades*. OLYMPUS CORPORATION. Available from:https://www.olympus-ims.com/en/applications/shear-web-bonding-inspection/.

46. JASIŪNIENĖ, E., et al. Ultrasonic NDT of Wind Turbine Blades using Contact Pulse-Echo Immersion Testing with Moving Water Container. *Ultragarsas (Ultrasound)*, 2008, vol. 63, no. 3. pp. 28-32 ISSN 1392-2114.

47. AMENABAR, I., et al. *Comparison and Analysis of Non-Destructive Testing Techniques Suitable for Delamination Inspection in Wind Turbine Blades.* , July 2011, 2011 Available from: http://www.sciencedirect.com/science/article/pii/S1359836811000539 ISBN 1359-8368. DOI https://doi.org/10.1016/j.compositesb.2011.01.025.

48. TIWARI, K.A. and RAISUTIS, R. Investigation of the 3D Displacement Characteristics for a Macro-Fiber Composite Transducer (MFC-P1). *Materiali in Tehnologije*, 03/25, 2018, vol. 52, no. 2. pp. 235-239 ISSN 1580-2949; 1580-3414.

49. TIWARI, K.A., RAISUTIS, R., MAZEIKA, L. and SAMAITIS, V. *Development of a 2D Analytical Model for the Prediction of Directivity Pattern of Transducers in the Generation of Guided Wave Modes.* , 2017, 2017 Available from:

http://www.sciencedirect.com/science/article/pii/S2452321617302512 ISBN 2452-3216. DOI https://doi.org/10.1016/j.prostr.2017.07.139.

50. TIWARI, .K.A., RAISUTIS, R., MAZEIKA, L. and SAMAITIS, V. 2D Analytical Model for the Directivity Prediction of Ultrasonic Contact Type Transducers in the Generation of Guided Waves. *Sensors*, March 26, 2018, 2018, vol. 18, no. 4. pp. 987 ISSN 1424-8220.

51. WU, H.C., GUPTA, N. and MYLAVARAPU, P.S. Blind Multiridge Detection for Automatic Nondestructive Testing using Ultrasonic Signals. *IEEE Transactions on Ultrasonics, Ferroelectrics, and Frequency Control*, Oct, 2006, vol. 53, no. 10. pp. 1902-1911 ISSN 0885-3010; 0885-3010.

52. SATYANARAYAN, L., BHARATH KUMARAN, K., KRISHNAMURTHY, C.V. and BALASUBRAMANIAM, K. *Inverse Method for Detection and Sizing of Cracks in Thin Sections using a Hybrid Genetic Algorithm Based Signal Parametrisation.* , April 2008, 2008 Available from: http://www.sciencedirect.com/science/article/pii/S016784420700105X ISBN 0167-8442. DOI https://doi.org/10.1016/j.tafmec.2007.11.004.

53. TIWARI, K.A., RAISUTIS, R. and SAMAITIS, V. Hybrid Signal Processing Technique to Improve the Defect Estimation in Ultrasonic Non-Destructive Testing of Composite Structures. *Sensors*, 2017, vol. 17, no. 12; BER = {2858. pp. 2858 ISSN 1424-8220.

54. TIWARI, K.A. and RAISUTIS, R. Post-Processing of Ultrasonic Signals for the Analysis of Defects in Wind Turbine Blade using Guided Waves. *The Journal of Strain Analysis for Engineering Design*, 05/08; 2018/05, 2018. pp. 0309324718772668 ISSN 0309-3247.

55. TIWARI, K.A. and RAISUTIS, R. Identification and Characterization of Defects in Glass Fiber Reinforced Plastic by Refining the Guided Lamb Waves. *Materials*, 09.07.2018, 2018, vol. 11, no. 7. pp. 1173 ISSN 1996-1944.

56. SAGAR, S.P. *Modern Ultrasonic Technique for Defect Detection in Cast Materials.* SAHU, A. K. ed., Jamshedpur, India ed. Jamshedpur: National Metallurgical Laboratory, Jamshedpur, Feb. 25-26, 2008, 2008.

57. WRIGHT, W.M.D. *Air-Coupled Ultrasonic Testing of Materials.* Ph.D. ed. Warwick, U.K.: University of Warwick, 1996.

58. ROSE, J.L. A Baseline and Vision of Ultrasonic Guided Wave Inspection Potential. *Journal of Pressure Vessel Technology*, 2002, vol. 124, no. 3. pp. 273-282 ISSN 1528-8978.

59. ROSE, J.L. *Ultrasonic Guided Waves in Solid Media*. Cambridge University Press, 2014 ISBN 9781107273610.

60. DRAUDVILIENĖ, L., RAIŠUTIS, R., ŽUKAUSKAS, E. and JANKAUSKAS, A. Validation of Dispersion Curve Reconstruction Techniques for the A0 and S0 Modes of Lamb

Waves. *International Journal of Structural Stability and Dynamics*, 2014, vol. 14, no. 07. pp. 1450024 ISSN 1793-6764.

61. TOYAMA, N. and TAKATSUBO, J. Lamb Wave Method for Quick Inspection of Impact-Induced Delamination in Composite Laminates. *Composites Science and Technology*, July 2004, 2004, vol. 64, no. 9. pp. 1293-1300. Available from: http://www.sciencedirect.com/science/article/pii/S0266353803003968 ISSN 0266-3538. DOI https://doi.org/10.1016/j.compscitech.2003.10.011.

62. EDALATI, K., KERMANI, A., SEIEDI, M. and MOVAFEGHI, A. Defect Detection in Thin Plates by Ultrasonic Lamb Wave Techniques. *International Journal of Materials and Product Technology*, 2006, vol. 27, no. 3-4. pp. 156-172 ISSN 1741-5209.

63. SU, Z., YE, L. and LU, Y. *Guided Lamb Waves for Identification of Damage in Composite Structures: A Review.* , 22 August 2006, 2006 Available from: http://www.sciencedirect.com/science/article/pii/S0022460X0600109X ISBN 0022-460X. DOI https://doi.org/10.1016/j.jsv.2006.01.020.

64. KUSANO, M., et al. Simultaneous Sound Velocity and Thickness Measurement by the Ultrasonic Pitch-Catch Method for Corrosion-Layer-Forming Polymeric Materials. *Ultrasonics*, January 2018, 2018, vol. 82. pp. 178-187. Available from: http://www.sciencedirect.com/science/article/pii/S0041624X17301853 ISSN 0041-624X. DOI https://doi.org/10.1016/j.ultras.2017.08.001.

65. YUE, N., SHARIF KHODAEI, Z. and ALIABADI, F.M. Damage Detectability Model of Pitch-Catch Configuration in Composite Plates. *Key Engineering Materials*, September 2017, 2017, vol. 754. pp. 387-390 ISSN 1662-9795.

66. MIZOTA, H., NAGASHIMA, Y. and NAKAHATA, K. An Ultrasonic Testing Method for Homogeneous Anisotropic Materials. *Insight-Non-Destructive Testing and Condition Monitoring*, 2017, vol. 59, no. 7. pp. 351-357 ISSN ISSN 1354-2575.

67. PARK, J., et al. Pitch-Catch Ultrasonic Study on Unidirectional CFRP Composite Laminates using Rayleigh Wave Transducers. *Journal of Mechanical Science and Technology*, 07/01, 2012, vol. 26, no. 7. pp. 2147-2150 ISSN 1976-3824.

68. YANG, I., et al. Feasibility on Fiber Orientation Detection of Unidirectional CFRP Composite Laminates using One-Sided Pitch–catch Ultrasonic Technique. *Composites Science and Technology*, October 2009, 2009, vol. 69, no. 13. pp. 2042-2047. Available from: http://www.sciencedirect.com/science/article/pii/S0266353809000104 ISSN 0266-3538. DOI https://doi.org/10.1016/j.compscitech.2009.01.007.

69. KOZLOV, V.N., SAMOKRUTOV, A.A. and SHEVALDYKIN, V.G. Thickness Measurements and Flaw Detection in Concrete using Ultrasonic Echo Method. *Nondestructive Testing and Evaluation*, 01/01, 1997, vol. 13, no. 2. pp. 73-84 ISSN 1058-9759.

70. ABARKANE, C., et al. Ultrasonic Pulse-Echo Signal Analysis for Damage Evaluation of Metallic Slit-Plate Hysteretic Dampers. *Metals*, 2017, vol. 7, no. 12. pp. 526 ISSN 2075-4701.

71. FOUDZI, F.M. and IHARA, I. Development of Polygonal Buffer Rods for Ultrasonic Pulse-Echo Measurements. *Journal of Physics: Conference Series*, 2014, vol. 520, no. 1. pp. 012025 ISSN 1742-6596.

72. BAI, Z., CHEN, S., JIA, L. and ZENG, Z. Phased Array Ultrasonic Signal Compressive Detection in Low-Pressure Turbine Disc. *NDT & E International*, July 2017, 2017, vol. 89. pp. 1-13. Available from: http://www.sciencedirect.com/science/article/pii/S0963869517301445 ISSN 0963-8695. DOI https://doi.org/10.1016/j.ndteint.2017.03.002.

73. CHI, S.C., CHO, B.J., NAM, M.H., LIM, S. Delamination Detection in Composite Wind Blade by Phased Array Ultrasonic Technology. *Journal of the Korean Society for Nondestructive Testing*, 2017/6, 2017, vol. 37, no. 3. pp. 183-191. Available from: http://www.dbpia.co.kr/Article/NODE07196955 ISSN 1225-7842. DOI 10.7779/JKSNT.2017.37.3.183.

74. TAHERI, H., DELFANIAN, F. and DU, J. Ultrasonic Phased Array Techniques for Composite Material Evaluation. *The Journal of the Acoustical Society of America*, 2013, vol. 134, no. 5. pp. 4013-4013 ISSN 1520-8524.

75. GIURGIUTIU, V. *Structural Health Monitoring: With Piezoelectric Wafer Active Sensors*. Elsevier, 2007.

76. VIKTOROV, I.A. *Rayleigh and Lamb Waves: Physical Theory and Applications*. Springer US, 2013 ISBN 9781489956835.

77. OSTACHOWICZ, W., KUDELA, P., KRAWCZUK, M. and ZAK, A. Guided Waves in Structures for SHMWiley-Blackwell, 2012 *Introduction to the Theory of Elastic Waves*, pp. 1-46 ISBN 9781119965855.

78. FRANK PAI, P., DENG, H. and SUNDARESAN, M.J. Time-Frequency Characterization of Lamb Waves for Material Evaluation and Damage Inspection of Plates. *Mechanical Systems and Signal Processing*, October 2015, 2015, vol. 62-63. pp. 183-206. Available from: http://www.sciencedirect.com/science/article/pii/S0888327015001077 ISSN 0888-3270. DOI https://doi.org/10.1016/j.ymssp.2015.03.011.

79. BEN, B.S., BEN, B.A., VIKRAM, K.A. and YANG, S.H. Damage Identification in Composite Materials using Ultrasonic Based Lamb Wave Method. *Measurement*, February 2013, 2013, vol. 46, no. 2. pp. 904-912. Available from: http://www.sciencedirect.com/science/article/pii/S0263224112003831 ISSN 0263-2241. DOI https://doi.org/10.1016/j.measurement.2012.10.011.

80. WORDEN, K. Rayleigh and Lamb Waves - Basic Principles. *Strain*, 11/01; 2018/05, 2001, vol. 37, no. 4. pp. 167-172 ISSN 0039-2103.

81. NOGUEIRA, V.P.P., REBELLO, J.M.A. and NETTO, T.A. *Ultrasonic Guided Wave Inspection in Rigid Riser,Proceedings of COBEM, 18th International Congress of Mechanical Engineering*. TRABASSO, Luís Gonzaga ed., Ouro Preto, Minas Gerias, Brazil ed. Ouro Preto, Minas Gerias, Brazil: ABCM, November 6-11, 2005, 2005 ISBN 858797808X.

82. PAVLAKOVIC, B., LOWE, M., ALLEYNE, D. and CAWLEY, P. Review of Progress in Quantitative Nondestructive Evaluation: Volume 16A D.O. THOMPSON and D.E. CHIMENTI eds., Boston, MA: Springer US, 1997 *Disperse: A General Purpose Program for Creating Dispersion Curves*, pp. 185-192 ISBN 978-1-4615-5947-4.

83. AULD, B.A. *Acoustic Fields and Waves in Solids*. 2nd ed. Stanford: Krieger Publishing, 1990 ISBN 978-0894644900.

84. PAVLAKOVIC, B.N. *Leaky Guided Ultrasonic Waves in NDT*. P.h.D ed. London: University of London London, UK, 1998.

85. LIU, Y., MOHANTY, S. and CHATTOPADHYAY, A. Condition Based Structural Health Monitoring and Prognosis ofÂ Composite Structures Under Uniaxial and Biaxial Loading. *Journal of Nondestructive Evaluation*, 09/01, 2010, vol. 29, no. 3. pp. 181-188 ISSN 1573-4862.

86. NEERUKATTI, R.K., HENSBERRY, K., KOVVALI, N. and CHATTOPADHYAY, A. A Novel Probabilistic Approach for Damage Localization and Prognosis Including Temperature Compensation. *Journal of Intelligent Material Systems and Structures*, 03/01; 2018/06, 2016, vol. 27, no. 5. pp. 592-607 ISSN 1045-389X.

87. RHEE, S., LEE, J. and LEE, J. The Group Velocity Variation of Lamb Wave in Fiber Reinforced Composite Plate. *Ultrasonics*, December 2007, 2007, vol. 47, no. 1. pp. 55-63. Available from: http://www.sciencedirect.com/science/article/pii/S0041624X07000662 ISSN 0041-624X. DOI https://doi.org/10.1016/j.ultras.2007.07.005.

88. GREEN, R.E. Non-Contact Ultrasonic Techniques. *Ultrasonics*, April 2004, 2004, vol. 42, no. 1. pp. 9-16. Available from: http://www.sciencedirect.com/science/article/pii/S0041624X04000873 ISSN 0041-624X. DOI https://doi.org/10.1016/j.ultras.2004.01.101.

89. AMZIANE, A., et al. Laser Ultrasonics Detection of an Embedded Crack in a Composite Spherical Particle. *Ultrasonics*, January 2012, 2012, vol. 52, no. 1. pp. 39-46. Available from: http://www.sciencedirect.com/science/article/pii/S0041624X11001132 ISSN 0041-624X. DOI https://doi.org/10.1016/j.ultras.2011.06.008.

90. DJORDJEVIC, B.B. Laser Ultrasonic Guided Wave Methods for Defect Detection and Materials Characterisation. *International Journal of Microstructure and Materials Properties*, 2014, vol. 9, no. 3/4/5. pp. 338.

91. HE, C. A New Surface Wave EMAT with High SNR and the Application for Defect Detection in Thick-Walled Pipes. *Journal of Mechanical Engineering*, 2017, vol. 53, no. 04. pp. 59.

92. PADIYAR, M.J. and BALASUBRAMANIAM, K. Lamb Wave-Based Air-Coupled Ultrasonic Inspection Technique for Filament-Wound Composite Pipes. *Insight - Non-Destructive Testing and Condition Monitoring Feedback: Support@crossref.Org*, apr, 2014, vol. 56, no. 4. pp. 195-202.

93. KIM, J.-., et al. Imaging Defects in Laminate Composite Plates using Focused Shear Waves Generated by Air-Coupled Transducer. *Composite Structures*, sep, 2016, vol. 152. pp. 891-899.

94. KAZYS, R., SLITERIS, R. and SESTOKE, J. Air-Coupled Low Frequency Ultrasonic Transducers and Arrays with PMN-32\%PT Piezoelectric Crystals. *Sensors*, jan, 2017, vol. 17, no. 1. pp. 95.

95. OURSLER, D.A. and WAGNER, J.W. Review of Progress in Quantitative Nondestructive Evaluation: Volume 14 D.O. THOMPSON and D.E. CHIMENTI eds., Boston, MA: Springer US, 1995 *Narrow-Band Hybrid Pulsed Laser/EMAT System for Non-Contact Ultrasonic Inspection using Angled Shear Waves*, pp. 553-560 ISBN 978-1-4615-1987-4.

96. PEI, C., et al. A Study of Internal Defect Testing with the Laser-EMAT Ultrasonic Method. *IEEE} Transactions on Ultrasonics, Ferroelectrics and Frequency Control*, dec, 2012, vol. 59, no. 12. pp. 2702-2708.

97. HUTCHINS, D.A., WRIGHT, W.D., HAYWARD, G. and GACHAGAN, A. Air-Coupled Piezoelectric Detection of Laser-Generated Ultrasound. *IEEE Transactions on Ultrasonics, Ferroelectrics, and Frequency Control*, 1994, vol. 41, no. 6. pp. 796-805 ISSN 0885-3010; 0885-3010.

98. MAEDA, A. and HAYASHI, T. Defect Imaging of a Thin Plate by Laser Generation and Air-Coupled Ultrasonic Detection. *The Proceedings of Mechanical Engineering Congress, Japan*, 2017, vol. 2017, no. 0. pp. J0420403.

99. BALDWIN, K.C., BERNDT, T.P. and EHRLICH, M.J. Narrowband Laser Generation/Air-Coupled Detection: Ultrasonic System for on-Line Process Control of Composites. *Ultrasonics*, jun, 1999, vol. 37, no. 5. pp. 329-334.

100. LIU, T., KITIPORNCHAI, S. and VEIDT, M. Analysis of Acousto-Ultrasonic Characteristics for Contact-Type Transducers Coupled to Composite Laminated Plates. *International Journal of Mechanical Sciences*, jun, 2001, vol. 43, no. 6. pp. 1441-1456.

101. VLADIŠAUSKAS, A., ŠLITERIS, R., RAIŠUTIS, R. and SENIŪNAS, G. Contact Ultrasonic Transducers for Mechanical Scanning Systems. *Ultragarsas" Ultrasound"*, 2010, vol. 65, no. 2. pp. 30-35.

102. LEE, J.R., PARK, C.Y. and KONG, C.W. Simultaneous Active Strain and Ultrasonic Measurement using Fiber Acoustic Wave Piezoelectric Transducers. *Smart Structures and Systems*, feb, 2013, vol. 11, no. 2. pp. 185-197.

103. *MFC P1 Type.* Available from:https://www.smart-material.com/MFC-product-P1.html.

104. WILLIAM, K.W., et al. *Low-Cost Piezocomposite Actuator for Structural Control Applications.* CA, United States ed. SPIE, 12 June, 2000, 2000.

105. REN, G. and JHANG, K. Application of Macrofiber Composite for Smart Transducer of Lamb Wave Inspection. *Advances in Materials Science and Engineering*, 2013, vol. 2013. pp. 264-269.

106. WONG, B.S. Non-Destructive Evaluation ({NDE}) of Polymer Matrix Composites V.M. KARBHARI ed., 1st ed. Elsevier, 2013 *Non-Destructive Evaluation (NDE) of Composites: Detecting Delamination Defects using Mechanical Impedance, Ultrasonic and Infrared Thermographic Techniques*, pp. 279-308 ISBN 9780857093554.

107. KRAUTKRAMER, J. and KRAUTKRAMER, H. *Ultrasonic Testing of Materials: Third — Revised Edition, Springer-Verlag, Berlin, 1983 667 Pp, Price DM 188, US S81.10 Approx. ISBN: 3 540 11733-4.* , June–July 1983, 1983 Available from: http://www.sciencedirect.com/science/article/pii/0261306983902091 ISBN 0261-3069. DOI https://doi.org/10.1016/0261-3069(83)90209-1 ".

108. KRAUTKRAMER, H. Presentation and Computing of Ultrasonic Data. *Ultrasonics*, January 1966, 1966, vol. 4, no. 1. pp. iii. Available from: http://www.sciencedirect.com/science/article/pii/0041624X66900370 ISSN 0041-624X. DOI https://doi.org/10.1016/0041-624X(66)90037-0 ".

109. FAHR, A. *Aeronautical Applications of Non-Destructive Testing.* Lancaster, Pennsylvania: Destech Publications, Inc, 2013.

110. UMCHID, S. Directivity Pattern Measurement of Ultrasound Transducers. *The International Journal on Applied Biomedical Engineering (IJABME)*, 2009, vol. 2. pp. 39-43.

111. QI, W. and CAO, W. Finite Element Study on 1-D Array Transducer Design. *IEEE Transactions on Ultrasonics, Ferroelectrics, and Frequency Control*, July, 2000, vol. 47, no. 4. pp. 949-955 ISSN 0885-3010.

112. VOELZ, U. *Four-Dimensional Directivity Pattern for Fast Calculation of the Sound Field of a Phased Array Transducer.* Dresden, Germany ed. IEEE}, 7-10 Oct, 2012 DOI 10.1109/ultsym.2012.0259.

113. DAOJIANG LI, H.C. Directivity Calculation for Acoustic Transducer Arrays with Considering Mutual Radiation Impedance. *Proc.SPIE*, 2013, vol. 8768. pp. 8768.

114. HAIG, A.G., SANDERSON, R.M., MUDGE, P.J. and BALACHANDRAN, W. Macro-Fibre Composite Actuators for the Transduction of Lamb and Horizontal Shear Ultrasonic Guided Waves. *Insight - Non-Destructive Testing and Condition Monitoring Feedback: Support@crossref.Org*, feb, 2013, vol. 55, no. 2. pp. 72-77.

115. CONJUSTEAU, A., et al. Measurement of the Spectral Directivity of Optoacoustic and Ultrasonic Transducers with a Laser Ultrasonic Source. *The Review of Scientific Instruments*, Sep, 2009, vol. 80, no. 9. pp. 093708 ISSN 1089-7623; 0034-6748.

116. BOND, L.J. Laser Ultrasonics: Techniques and Applications. *Ultrasonics*, sep, 1991, vol. 29, no. 5. pp. 418-419.

117. MAHMUD, K.M., BABA, N. and OHBA, R. Using of a Diverse Field Algorithm in Ultrasonic Signal Processing for Nondestructive Testing. *The European Physical Journal - Applied Physics*, 2001/07/15, 2001, vol. 15, no. 1 [viewed 2018/06/12]. pp. 3-6. Available from: https://www.cambridge.org/core/article/using-of-a-diverse-field-algorithm-in-ultrasonic-signal-processing-for-nondestructive-testing/B633B2EB2D8D0990BB8582EDF644399C Cambridge Core. ISSN 1286-0042. DOI 10.1051/epjap:2001161.

118. ABBATE, A., et al. Signal Detection and Noise Suppression using a Wavelet Transform Signal Processor: Application to Ultrasonic Flaw Detection. *IEEE Transactions on Ultrasonics, Ferroelectrics, and Frequency Control*, 1997, vol. 44, no. 1. pp. 14-26.

119. MALLETT, R., MUDGE, P., GAN, T. and BALACHANDRA, W. Analysis of Cross-Correlation and Wavelet De-Noising for the Reduction of the Effects of Dispersion in Long-Range Ultrasonic Testing. *Insight-Non-Destructive Testing and Condition Monitoring*, 2007, vol. 49, no. 6. pp. 350-355.

120. PRIYA, K.D., RAO, G.S. and RAO, P.S.V.S. *Comparative Analysis of Wavelet Thresholding Techniques with Wavelet-Wiener Filter on ECG Signal.* , 2016, 2016 Available from: http://www.sciencedirect.com/science/article/pii/S1877050916304847 ISBN 1877-0509. DOI https://doi.org/10.1016/j.procs.2016.05.145.

121. SINGH, B.N. and TIWARI, A.K. Optimal Selection of Wavelet Basis Function Applied to ECG Signal Denoising. *Digital Signal Processing*, May 2006, 2006, vol. 16, no. 3. pp. 275-287. Available from: http://www.sciencedirect.com/science/article/pii/S1051200405001703 ISSN 1051-2004. DOI https://doi.org/10.1016/j.dsp.2005.12.003.

122. TIWARI, K.A., RAISUTIS, R. and SAMAITIS, V. *Signal Processing Methods to Improve the Signal-to-Noise Ratio (SNR) in Ultrasonic Non-Destructive Testing of Wind Turbine Blade.* , 2017, 2017 Available from:

http://www.sciencedirect.com/science/article/pii/S2452321617301221 ISBN 2452-3216. DOI https://doi.org/10.1016/j.prostr.2017.07.036.

123. PRINCE, A.A., VERMA, P.K., JAYAKUMAR, C. and RAJU, D. *Efficient Architecture for Real Time Implementation of Hilbert Transform in FPGA.* Coimbatore, India ed. IEEE, 5-7 March, 2015 DOI 10.1109/ICECCT.2015.7226158.

124. MICHAEL, F. Encyclopedia of Structural Health Monitoring C. BOLLER, F. CHANG and Y. FUJINO eds., N.J., USA: John Wiley & Sons, Ltd., 2009 *Hilbert Transform, Envelope, Instantaneous Phase, and Frequency*, pp. 1-16 ISBN 9780470061626.

125. HUANG, N.E., et al. The Empirical Mode Decomposition and the Hilbert Spectrum for Nonlinear and Non-Stationary Time Series Analysis. *Proceedings of the Royal Society of London.Series A: Mathematical, Physical and Engineering Sciences*, The Royal Society, 1998, vol. 454, no. 1971. pp. 903-995. Available from: http://rspa.royalsocietypublishing.org/content/454/1971/903.abstract DOI 10.1098/rspa.1998.0193.

126. WU, Z. and HUANG, N.E. Ensemble Empirical Mode Decomposition: A Noise-Assisted Data Analysis Method. *Advances in Adaptive Data Analysis*, 01/01; 2018/04, 2009, vol. 01, no. 01. pp. 1-41 ISSN 1793-5369.

127. KAŽYS, R., TUMŠYS, O. and PAGODINAS, D. Ultrasonic Detection of Defects in Strongly Attenuating Structures using the Hilbert–Huang Transform. *NDT & E International*, September 2008, 2008, vol. 41, no. 6. pp. 457-466. Available from: http://www.sciencedirect.com/science/article/pii/S0963869508000236 ISSN 0963-8695. DOI https://doi.org/10.1016/j.ndteint.2008.03.006.

128. SANIIE, J., ORUKLU, E. and YOON, S. System-on-Chip Design for Ultrasonic Target Detection using Split-Spectrum Processing and Neural Networks. *IEEE Transactions on Ultrasonics, Ferroelectrics, and Frequency Control*, July, 2012, vol. 59, no. 7. pp. 1354-1368 ISSN 0885-3010.

129. SHANKAR, P.M., KARPUR, P., NEWHOUSE, V.L. and ROSE, J.L. Split-Spectrum Processing: Analysis of Polarity Threshold Algorithm for Improvement of Signal-to-Noise Ratio and Detectability in Ultrasonic Signals. *IEEE Transactions on Ultrasonics, Ferroelectrics, and Frequency Control*, 1989, vol. 36, no. 1. pp. 101-108 ISSN 0885-3010; 0885-3010.

130. ZHANG, Z. and REN, Y. *Time–frequency Analysis of Echoes Signal in Ultrasonic Testing of Adhesion Based on Short-Time Fourier Transformation.* IEEE, 2010.

131. NIETHAMMER, M., et al. Application of the Short Time Fourier Transform to Interpret Ultrasonic Signals. *AIP Conference Proceedings*, 2000, vol. 509, no. 1. pp. 703-708.

132. ALLEYNE, D. and CAWLEY, P. A Two-Dimensional Fourier Transform Method for the Measurement of Propagating Multimode Signals. *The Journal of the Acoustical Society of America*, 1991, vol. 89, no. 3. pp. 1159-1168.

133. FATERI, S., BOULGOURIS, N.V. and WILKINSON, A. A Two-Dimensional Fast Fourier Transform using Incremented Frequency Measurement for Guided Wave Analysis. *Insight - Non-Destructive Testing and Condition Monitoring*, sep, 2014, vol. 56, no. 9. pp. 499-504.

134. QIU, L. *Wigner-Ville Distribution and Windowed Wigner-Ville Distribution of Noisy Signals.* , Sept, 1993 DOI 10.1109/SICON.1993.515792.

135. CLAASEN, T. and MECKLENBRAUKER, W. The Wigner distribution—A Tool for Time-Frequency Signal Analysis. *Philips J.Res*, 1980, vol. 35, no. 3. pp. 217-250.

136. DRAGOMIRETSKIY, K. and ZOSSO, D. Variational Mode Decomposition. *IEEE Transactions on Signal Processing*, 2014, vol. 62, no. 3. pp. 531-544.

137. RODRIGUEZ, M.A., SAN EMETERIO, J.L., LAZARO, J.C. and RAMOS, A. Ultrasonic Flaw Detection in NDE of Highly Scattering Materials using Wavelet and Wigner-Ville Transform Processing. *Ultrasonics*, Apr, 2004, vol. 42, no. 1-9. pp. 847-851 ISSN 0041-624X; 0041-624X.

138. YU, G. and WANG, X. *Ultrasonic Signal Processing using Wavelet Transform for Automatic Rail Defect Detection.* KIM, Y. H. ed., Guangdong, China ed. Atlantis Press, January 30-31, 2016, 2016.

139. Elfouly, F., Mahmoud, M., Dessouky, M., Deyab,S. Comparison between Haar and Daubechies Wavelet Transformions on Fpga Technology. *International Journal of Computing*, 2014, vol. 6, no. 3. pp. 417-422.

140. GRAPS, A. An Introduction to Wavelets. *IEEE Computational Science and Engineering*, Summer, 1995, vol. 2, no. 2. pp. 50-61 ISSN 1070-9924.

141. JAFFERY, Z. and AHMAD, K. *Performance Comparision of Wavelet Threshold Estimators for ECG Signal Denoising.* Kottayam, India ed. IEEE, 16-17 Oct. 2010, 2010.

142. MALLAT, S.G. A Theory for Multiresolution Signal Decomposition: The Wavelet Representation. *IEEE Transactions on Pattern Analysis and Machine Intelligence*, Jul, 1989, vol. 11, no. 7. pp. 674-693 ISSN 0162-8828.

143. LÁZARO, J.C., SAN EMETERIO, J.L., RAMOS, A. and FERNÁNDEZ-MARRÓN, J.L. *Influence of Thresholding Procedures in Ultrasonic Grain Noise Reduction using Wavelets.* , May 2002, 2002 Available from: http://www.sciencedirect.com/science/article/pii/S0041624X0200149X ISBN 0041-624X. DOI https://doi.org/10.1016/S0041-624X(02)00149-X.

144. JOHNSTONE, I.M. and SILVERMAN, B.W. Wavelet Threshold Estimators for Data with Correlated Noise. *Journal of the Royal Statistical Society: Series B (Statistical Methodology)*, 01/06; 2018/04, 2002, vol. 59, no. 2. pp. 319-351 ISSN 1369-7412.

145. R. POLIKAR. *The Wavelet Tutorial:The Engineer's Ultimate Guide to Wavelet Analysis-the Wavelet Tutorial.* N.J., U.S.A.: Rowan University. , 2003 Available from:http://users.rowan.edu/%7Epolikar/WAVELETS/WTtutorial.html.

146. SUTER, B.W. Multirate and Wavelet Signal Processing B.W. SUTER ed., Academic Press, 1998, 1998 *Chapter 5 - Wavelet Signal Processing*, pp. 167-190. Available from: http://www.sciencedirect.com/science/article/pii/S1874608X98800502 ISBN 1874-608X. DOI https://doi.org/10.1016/S1874-608X(98)80050-2 ".

147. DONOHO, D.L. and JOHNSTONE, I.M. Ideal Spatial Adaptation by Wavelet Shrinkage. *Biometrika*, aug, 1994, vol. 81, no. 3. pp. 425.

148. VARGHESE, T., BILGEN, M. and OPHIR, J. Multiresolution Imaging in Elastography. *IEEE} Transactions on Ultrasonics, Ferroelectrics and Frequency Control*, jan, 1998, vol. 45, no. 1. pp. 65-75 ISSN 0885-3010.

149. CHEN, H.G., YAN, Y.J. and JIANG, J.S. Fracture and Damage Mechanics V5th ed. Zürich, Switzerland: Trans Tech Publications Ltd, nov, 2006 *Vibration-Based Damage Detection of Composite Wingbox Structures using Improved Hilbert-Huang Transform*, pp. 539-542.

150. TORRES, M.E., COLOMINAS, M.A., SCHLOTTHAUER, G. and FLANDRIN, P. *A Complete Ensemble Empirical Mode Decomposition with Adaptive Noise.* , May, 2011 ISBN 1520-6149. DOI 10.1109/ICASSP.2011.5947265.

151. BERTSEKAS, D.P. Multiplier Methods: A Survey. *Automatica*, mar, 1976, vol. 12, no. 2. pp. 133-145.

152. NOCEDAL, J. and WRIGHT, S.J. *Numerical Optimization.* 2nd ed. Germany: Springer Berlin Heidelberg, 2006.

153. BOASHASH, B. Estimating and Interpreting the Instantaneous Frequency of a Signal. I. Fundamentals. *Proceedings of the IEEE*, April, 1992, vol. 80, no. 4. pp. 520-538 ISSN 0018-9219.

154. SALIU, S. *Definition of Instantaneous Frequency on Real Signals.* Tampere, Finland ed. , 2000.

155. PAVLOPOULOU, S., STASZEWSKI, W.J., SOUTIS, C. Evaluation of Instantaneous Characteristics of Guided Ultrasonic Waves for Structural Quality and Health Monitoring. *Structural Control and Health Monitoring*, 06/01; 2018/07, 2013, vol. 20, no. 6. pp. 937-955 ISSN 1545-2255.

156. WANG, T., ZHANG, M., YU, Q. and ZHANG, H. *Comparing the Applications of EMD and EEMD on Time–frequency Analysis of Seismic Signal.* , August 2012, 2012 Available from: http://www.sciencedirect.com/science/article/pii/S0926985112000791 ISBN 0926-9851. DOI https://doi.org/10.1016/j.jappgeo.2012.05.002.

157. BEASLEY, E.W. and WARD, H.R. A Quantitative Analysis of Sea Clutter Decorrelation with Frequency Agility. *IEEE} Transactions on Aerospace and Electronic Systems*, may, 1968, vol. AES}-4, no. 3. pp. 468-473.

158. NEWHOUSE, V.L., BILGUTAY, N.M., SANIIE, J. and FURGASON, E.S. *Flaw-to-Grain Echo Enhancement by Split-Spectrum Processing.* , March 1982, 1982 Available from: http://www.sciencedirect.com/science/article/pii/0041624X82900038 ISBN 0041-624X. DOI https://doi.org/10.1016/0041-624X(82)90003-8.

159. PEDRAM, S.K., et al. *Split-Spectrum Processing Technique for SNR Enhancement of Ultrasonic Guided Wave.* , February 2018, 2018 Available from: http://www.sciencedirect.com/science/article/pii/S0041624X17301622 ISBN 0041-624X. DOI https://doi.org/10.1016/j.ultras.2017.08.002.

160. RUBBERS, P. and PRITCHARD, C.J. An Overview of Split Spectrum Processing. *Journal of Nondestructive Testing*, 2003, vol. 8, no. 8. pp. 1-11.

161. RAISUTIS, R., TUMSYS, O., KAZYS, R. and MAZEIKA, L. A Comparative Study of Time-Frequency Analysis Techniques in the Case of Signal Processing for Ultrasonic NDT. *Insight - Non-Destructive Testing and Condition Monitoring Feedback: Support@crossref.Org*, nov, 2008, vol. 50, no. 11. pp. 628-633.

162. ALLEN, J. Short Term Spectral Analysis, Synthesis, and Modification by Discrete Fourier Transform. *IEEE} Transactions on Acoustics, Speech, and Signal Processing*, jun, 1977, vol. 25, no. 3. pp. 235-238.

163. JIANG, X., et al. Detecting the Flaws in Prestressing Strands using Guided Waves Based on the Magnetostrictive Effect. *Insight - Non-Destructive Testing and Condition Monitoring*, nov, 2007, vol. 49, no. 11. pp. 647-650.

164. COHEN, L. Time-Frequency Distributions-a Review. *Proceedings of the {IEEE}*, jul, 1989, vol. 77, no. 7. pp. 941-981.

165. LATIF, R., et al. Determination of the Group and Phase Velocities from Time–frequency Representation of Wigner–Ville. *NDT & E International*, October 1999, 1999, vol. 32, no. 7. pp. 415-422. Available from: http://www.sciencedirect.com/science/article/pii/S0963869599000134 ISSN 0963-8695. DOI https://doi.org/10.1016/S0963-8695(99)00013-4.

166. WU, J., CHEN, X. and MA, Z. A Signal Decomposition Method for Ultrasonic Guided Wave Generated from Debonding Combining Smoothed Pseudo Wigner-Ville Distribution

and Vold\textendashKalman Filter Order Tracking. *Shock and Vibration*, 2017, vol. 2017. pp. 1-13.

167. MEDINA, L. and RUBIO, E. *Wigner-Ville Distribution Enhancement for 2D-Flaws Location.* , Oct, 2003 DOI 10.1109/ULTSYM.2003.1293160.

168. ASHWILL, T.D. *Cost Study for Large Wind Turbine Blades*. {OSTI}: Office of Scientific and Technical Information. may, 2003.

169. DREWRY, M.A. and GEORGIOU, G.A. A Review of NDT Techniques for Wind Turbines. *Insight - Non-Destructive Testing and Condition Monitoring*, mar, 2007, vol. 49, no. 3. pp. 137-141.

170. JUENGERT, A. and GROSSE, C.U. *Inspection Techniques for Wind Turbine Blades using Ultrasound and Sound Waves*. Nantes, France ed. NDTCE'09, Non-Destructive Testing in Civil Engineering, 30 June-3 July, 2009.

171. SCHMIDT, F., et al. *Monitoring of Multiaxial Fatigue Damage Evolution in Impacted Composite Tubes using Non-Destructive Evaluation.* , March 2012, 2012 Available from: http://www.sciencedirect.com/science/article/pii/S1359835X11003964 ISBN 1359-835X. DOI https://doi.org/10.1016/j.compositesa.2011.12.002.

172. Jeffery D. Tippmann,Arun Manohar,Francesco Lanza di Scalea. Wind Turbine Inspection Tests at UCSD. *Proc.SPIE*, 2012, vol. 8345. pp. 8345.

173. LAMBERT, J., CHAMBERS, A.R., SINCLAIR, I. and SPEARING, S.M. *3D Damage Characterisation and the Role of Voids in the Fatigue of Wind Turbine Blade Materials.* , 18 January 2012, 2012 Available from: http://www.sciencedirect.com/science/article/pii/S0266353811004155 ISBN 0266-3538. DOI https://doi.org/10.1016/j.compscitech.2011.11.023.

174. DIAMANTI, K., SOUTIS, C. and HODGKINSON, J.M. *Non-Destructive Inspection of Sandwich and Repaired Composite Laminated Structures.* , October 2005, 2005 Available from: http://www.sciencedirect.com/science/article/pii/S0266353805001004 ISBN 0266-3538. DOI https://doi.org/10.1016/j.compscitech.2005.04.010.

175. RAIŠUTIS, R., JASIŪNIENĖ, E. and ŽUKAUSKAS, E. Ultrasonic NDT of Wind Turbine Blades using Guided Waves. *Ultragarsas*, 2008, vol. 63, no. 1. pp. 7-11.

176. LEE, J.R., et al. Ultrasonic Propagation Imaging for Wind Turbine Blade Quality Evaluation. *Advanced Materials Research*, aug, 2010, vol. 123-125. pp. 847-850.

177. NAM, M. Application of Phased Array Ultrasonic Testing to Detect Delamination for Wind Turbine Blade. *Journal of Wind Energy*, sep, 2018, vol. 9, no. 3. pp. 33-42.

178. STEIGMANN, R., IFTIMIE, N., SAVIN, A. and STURM, R. Wind Turbine Blade Composites Assessment using Non-Contact Ultrasound Method. *Journal of Clean Energy Technologies*, 2016, vol. 4, no. 6. pp. 440-443.

179. CHADY, T. Wind Turbine Blades Inspection Techniques. *PRZEGL}{\k{A}}D {ELEKTROTECHNICZNY}*, may, 2016, vol. 1, no. 5. pp. 3-6.

180. HAFEZI, M.H., ALEBRAHIM, R. and KUNDU, T. *Peri-Ultrasound for Modeling Linear and Nonlinear Ultrasonic Response.* , September 2017, 2017 Available from: http://www.sciencedirect.com/science/article/pii/S0041624X16303900 ISBN 0041-624X. DOI https://doi.org/10.1016/j.ultras.2017.04.015.

181. HAFEZI, M.H. and KUNDU, T. Peri-Ultrasound Modeling of Dynamic Response of an Interface Crack Showing Wave Scattering and Crack Propagation. *Journal of Nondestructive Evaluation, Diagnostics and Prognostics of Engineering Systems*, sep, 2017, vol. 1, no. 1. pp. 011003.

182. JHANG, K. Applications of Nonlinear Ultrasonics to the NDE of Material Degradation. *IEEE Transactions on Ultrasonics, Ferroelectrics, and Frequency Control*, May, 2000, vol. 47, no. 3. pp. 540-548 ISSN 0885-3010.

183. PULLIN, R., et al. On the Development of a Damage Detection System using Macro-Fibre Composite Sensors. *Journal of Physics: Conference Series*, 2012, vol. 382, no. 1. pp. 1-7.

184. WANG, X., ZHOU, W., XUN, G. and WU, Z. Dynamic Shape Control of Piezocomposite-Actuated Morphing Wings with Vibration Suppression. *Journal of Intelligent Material Systems and Structures*, 02/01; 2018/07, 2018, vol. 29, no. 3. pp. 358-370 ISSN 1045-389X.

185. DEBIASI, M., LEONG, C.W., BOUREMEL, Y. and YAP, C. *Application of Macro-Fiber-Composite Materials on UAV Wings.* Singapore ed. Singapore: , 2013.

186. RIZZO, P., et al. *Guided Ultrasonic Waves for the Inspection of Structural Components.* Ubertini, Viola, De Miranda and Castellazzi eds., Bologna, Italy ed. University of Bologna, 2006.

187. DOYUM, A. and DUERER, M. Defect Characterization of Composite Honeycomb Panels by Non-Destructive Inspection Methods. *NDT.Net*, 2002. pp. 1-4 ISSN 3-931381-39-0.

188. RAIŠUTIS, R., et al. Analysis of Ultrasonic Guided Waves Propagation in Complex Composite Structures. *International Journal of Structural Stability and Dynamics*, 12/01; 2018/07, 2014, vol. 14, no. 08. pp. 1440024 ISSN 0219-4554.

189. CHEONG, T.W. and ZHENG, L.W. Vibroacoustic Performance of Composite Honecomb Structures. *Noise Control Engineering Journal*, 2006, vol. 54, no. 4. pp. 251-262 ISSN 0736-2501.

190. MATT, H.M. and SCALEA, F.L.d. Macro-Fiber Composite Piezoelectric Rosettes for Acoustic Source Location in Complex Structures. *Smart Materials and Structures*, 2007, vol. 16, no. 4. pp. 1489-1499 ISSN 0964-1726.

191. BILGEN, O., KOCHERSBERGER, K.B., INMAN, D.J. and OHANIAN, O.J. Novel, Bidirectional, Variable-Camber Airfoil Via Macro-Fiber Composite Actuators. *Journal of Aircraft*, 2010, vol. 17, no. 1. pp. 303-314 ISSN 0021-8669.

192. DIKSHIT, A.K., PAL, M., BISWAS, P. and BHADRA, S.K. Efficient Lasing Wavelength Tuning in Distributed Bragg Reflector Fiber Laser using PZT Macrofiber Composite Actuator. *Journal of Lightwave Technology*, June, 2010, vol. 28, no. 12. pp. 1783-1788 ISSN 0733-8724.

193. Worden K. Rayleigh and Lamb Waves - Basic Principles. *Strain*, 11/01; 2018/07, 2001, vol. 37, no. 4. pp. 167-172 ISSN 0039-2103.

194. MAŃKA, M. et al. Lamb Wave Transducers made of Piezoelectric Macro-Fiber Composite. *Structural Control and Health Monitoring*, 08/01; 2018/07, 2013, vol. 20, no. 8. pp. 1138-1158 ISSN 1545-2255.

195. COLEMAN, C.J. Huygen's Principle Applied to Radio Wave Propagation. *Radio Science*, 12/01; 2018/07, 2002, vol. 37, no. 6. pp. 17-11; 17-8 ISSN 0048-6604.

196. SAMAITIS, V. and MAZEIKA, L. Influence of the Spatial Dimensions of Ultrasonic Transducers on the Frequency Spectrum of Guided Waves. *Sensors*, 2017, vol. 17, no. 8; ISSN 1424-8220.

197. MU, J. and ROSE, J.L. Guided Wave Propagation and Mode Differentiation in Hollow Cylinders with Viscoelastic Coatings. *The Journal of the Acoustical Society of America*, Aug, 2008, vol. 124, no. 2. pp. 866-874 ISSN 1520-8524; 0001-4966.

198. HAYASHI, T. and KAWASHIMA, K. *Multiple Reflections of Lamb Waves at a Delamination.* , May 2002, 2002 Available from: http://www.sciencedirect.com/science/article/pii/S0041624X02001361 ISBN 0041-624X. DOI https://doi.org/10.1016/S0041-624X(02)00136-1.

199. BARSKI, M. and PAJÄ…K, P. Determination of Dispersion Curves for Composite Materials with the use of Stiffness Matrix Method. *Acta Mechanica Et Automatica*, 2017, vol. 11, no. 2, pages: 121 - 128.

200. AHMAD, Z.A.B., VIVAR-PEREZ, J.M. and GABBERT, U. Semi-Analytical Finite Element Method for Modeling of Lamb Wave Propagation. *CEAS Aeronautical Journal*, Apr, 2013, vol. 4, no. 1. pp. 21-33 ISSN 1869-5590.

201. RAIŠUTIS, R., et al. *Application of Ultrasonic Guided Waves for Non-Destructive Testing of Defective CFRP Rods with Multiple Delaminations.* , July 2010, 2010 Available from: http://www.sciencedirect.com/science/article/pii/S0963869510000393 ISBN 0963-8695. DOI https://doi.org/10.1016/j.ndteint.2010.04.001.

202. MICHAELS, T.E., RUZZENE, M. and MICHAELS, J.E. *Frequency-Wavenumber Domain Methods for Analysis of Incident and Scattered Guided Wave Fields.* Tribikram Kundu ed., SPIE}, mar, 2009 DOI 10.1117/12.816046.

203. MICHAELS, T.E., MICHAELS, J.E. and RUZZENE, M. *Frequency–wavenumber Domain Analysis of Guided Wavefields.* , May 2011, 2011 Available from: http://www.sciencedirect.com/science/article/pii/S0041624X10001812 ISBN 0041-624X. DOI https://doi.org/10.1016/j.ultras.2010.11.011.

204. TAYLOR, B.N. *Guidelines for Evaluating and Expressing the Uncertainty of NIST Measurement Results.* National Bureau of Standards. , 1994.

205. HENZLER, S. Time-to-Digital ConvertersSpringer Netherlands, 2010 *Applications for Time-to-Digital Converters*, pp. 103-113.

206. KALISZ, J. Review of Methods for Time Interval Measurements with Picosecond Resolution. *Metrologia*, dec, 2003, vol. 41, no. 1. pp. 17-32.

207. RAISUTIS, R., KAZYS, R. and MAZEIKA, L. Ultrasonic Thickness Measurement of Multilayered Aluminum Foam Precursor Material. *IEEE Transactions on Instrumentation and Measurement*, Dec, 2008, vol. 57, no. 12. pp. 2846-2855 ISSN 0018-9456.

LIST OF PUBLICATIONS

Publications indexed in the master list of Thomson Reuters/ Web of Science (with impact factor)

1. **Tiwari, Kumar Anubhav;** Raisutis, Renaldas; Tumsys, Olgirdas; Ostreika, Armantas; Jankauskas, Kestutis; Jakutavicius, Julijus. Defect estimation in non-destructive testing of composites by guided waves and image processing. *Electronics* 2019, Vol.8, Article No. 315, p. 1-16. ISSN:2079-9292 [I.F.=2.11 (2017), **Q2**]
2. **Tiwari, Kumar Anubhav;** Raisutis, Renaldas. Identification and Characterization of Defects in Glass Fiber Reinforced Plastic by Refining the Guided Lamb Waves. *Materials* 2018, Vol.11, Article No. 1173, p. 1-23. ISSN:1996-1944 [I.F.=2.467 (2017), **Q2**]
3. **Tiwari, Kumar Anubhav;** Raisutis, Renaldas; Mazeika, Liudas; Samaitis, Vykintas. 2D analylical model for the directivity prediction of contact type ultrasonic transducers in the generation of guided waves. *Sensors* 2018, Vol. 18, Article No. 987, p. 1-17. ISSN:1424-8220 [I.F.=2.475 (2017), **Q1**]
4. **Tiwari, Kumar Anubhav;** Raisutis, Renaldas. Post-processing of ultrasonic signals for the analysis of defects in wind turbine blade using guided waves. *Journal of Strain Analysis for Engineering Design* 2018, Article No. 030932471877266, p. 1-10. ISSN:0309-3247 [I.F.=1.320 (2017), **Q3**]
5. **Tiwari, Kumar Anubhav;** Raisutis, Renaldas. Investigation of 3D displacement characteristics of Macro Fiber Composite transducer (MFC-P1). *Materiali in Tehnologije* (Materials and technology) 2018, Vol. 52, Iss. 2, p. 235-239. ISSN:1580-2949 [I.F.=0.59 (2017), **Q4**]
6. **Tiwari, Kumar Anubhav;** Raisutis, Renaldas; Samaitis, Vykintas. Hybrid Signal Processing Technique to Improve the Defect Estimation in Ultrasonic Non-Destructive Testing of Composite Structures. *Sensors* 2017, Vol. 17, Article No. 2858, p. 1-21. ISSN:1424-8220 [I.F.=2.475 (2017), **Q1**]
7. **Tiwari, Kumar Anubhav;** Ostreika, Armantas; Platuziene Jurate. Efficient FPGA-based FIR architecture and its significance in ultrasonic signal processing. *Journal of Vibroengineering* 2017, Vol. 19, Iss. 8, p. 6423-6432. ISSN:2538-8460 [I.F.=0.398 (2016), **Q3**]

Publications in the Conference proceeding journals indexed in the master list of Thomson Reuters/ Web of Science (without impact factor)

1. **Tiwari, Kumar Anubhav;** Raisutis, Renaldas. Refinement in the defect detection in the contact and non-contact ultrasonic non-destructive testing of wind turbine blade using guided waves. *Procedia Structural Integrity*

(proceedings of 22nd European Conference on Fracture - ECF22, 26-31 August 2018, Belgrade, Serbia) 2018, Elsevier, Vol. 13. p. 1566-1570. ISSN: 2452-3216

2. **Tiwari, Kumar Anubhav;** Raisutis, Renaldas; Samaitis, Vykintas. Signal processing methods to improve the Signal-to-noise ratio (SNR) in ultrasonic non-destructive testing of wind turbine blade. *Procedia Structural* Integrity (proceedings of 2nd International Conference on Structural Integrity, ICSI 2017, 4-7 September 2017, Funchal, Madeira, Portugal) 2017, Elsevier, Vol. 5, p. 1184–1191. ISSN:2452-3216
3. **Tiwari, Kumar Anubhav;** Raisutis, Renaldas; Mazeika, Liudas; Samaitis, Vykintas. Development of a 2D analytical model for the prediction of directivity pattern of transducers in the generation of guided wave modes. *Procedia Structural Integrity* (proceedings of 2nd International Conference on Structural Integrity, ICSI 2017, 4-7 September 2017, Funchal, Madeira, Portugal) 2017, Elsevier, Vol. 5, p. 973–980. ISSN: 2452-3216
4. **Tiwari, Kumar Anubhav;** Raisutis, Renaldas. Comparative analysis of non-contact ultrasonic methods for defect estimation of composites in remote areas. *CBU International conference proceedings* (proceedings of CBU international conference on innovations in science and education 23-25 March 2016, Prague, Czech Republic) 2016, Vol. 4, p. 846-851. ISSN:1805-997X

Abstracts published in the Conference proceedings

1. **Tiwari, Kumar Anubhav;** Tumsys, Olgirdas**;** Raisutis, Renaldas. Applicability of wavelet transform for the defect estimations in glass fiber based composite structures by ultrasonic non-destructive. Open Reading-2019-62nd International conference for students of physics and natural sciences, 19-22 March 2019, Vilnius, Lithuania. 2019. p. 65. ISBN: 9786090701379

2. **Tiwari, Kumar Anubhav;** Raisutis, Renaldas. Refinement in the defect detection in the contact and non-contact ultrasonic non-destructive testing of wind turbine blade using guided waves. 22nd European Conference on Fracture - ECF22, 26-31 August 2018, Belgrade, Serbia. 2018. p. 431. ISBN: 9788690068609

3. **Tiwari, Kumar Anubhav;** Raisutis, Renaldas; Samaitis, Vykintas. Signal processing methods to improve the Signal-to-noise ratio (SNR) in ultrasonic non-destructive testing of wind turbine blade. 2nd International Conference on Structural Integrity, ICSI 2017, 4-7 September 2017, Funchal, Madeira,

Portugal: Book of abstracts. Porto: INEGI, 2017. p. 182. ISBN: 9789728826338

4. **Tiwari, Kumar Anubhav;** Raisutis, Renaldas; Mazeika, Liudas; Samaitis, Vykintas. Development of a 2D analytical model for the prediction of directivity pattern of transducers in the generation of guided wave modes. 2nd International Conference on Structural Integrity, ICSI 2017, 4-7 September 2017, Funchal, Madeira, Portugal: Book of abstracts. Porto: INEGI, 2017. p. 170. ISBN: 9789728826338
5. **Tiwari, Kumar Anubhav;** Raisutis, Renaldas. Comparative analysis of non-contact ultrasonic methods for defect estimation of composites in remote areas. CBU international conference on innovations in science and education 23-25 March 2016, Central Bohemia University, Prague, Czech Republic: Book of Abstracts. 2016, p. 146. ISBN: 9788088042037
6. **Tiwari, Kumar Anubhav;** Raisutis, Renaldas. Signalo apdorojimo metodai siekiant pagerinti signalo ir triukšmo santykį (STS) vėjo turbinos menčių (VTM) ultragarsiniuose neardomuosiuose matavimuose. Fizinių ir technologijos mokslų tarpdalykiniai tyrimai [elektroninis išteklius]: 7-oji jaunųjų mokslininkų konferencija (Interdisciplinary Studies in Physical and Technological Sciences [Electronic Resources]:7th Young Scientists' Conference), 9 February 2017, Lithuanian academy of sciences, Vilnius, Lithuania: Summary of reports.2017, p. 58.
7. **Tiwari, Kumar Anubhav;** Raisutis, Renaldas. Comparision of non-contact ultrasonic methods for the defects estmation of composites in remote area. Fizinių ir technologijos mokslų tarpdalykiniai tyrimai [elektroninis išteklius]: 6-oji jaunųjų mokslininkų konferencija (Interdisciplinary Studies in Physical and Technological Sciences [Electronic Resources]:6th Young Scientists' Conference), 10 February 2016, Lithuanian Academy of sciences, Vilnius, Lithuania: Summary of reports.2016, p. 50.

ACKNOWLEDGMENTS

First and foremost, I thank my supervisor Prof. Renaldas Raisutis. It has been an honor to be his first international Ph.D. student. I appreciate all his contributions of time, ideas, and cooperation to make my Ph.D. experience productive and stimulating. The joy and enthusiasm he has for his research is contagious and motivational for me. I cannot forget his quick responses via e-mails even at late nights which is why I have been able to publish 7 articles with impact factors in 2017–2018. I am also grateful to all reviewers for their valuable comments and suggestions for the improvement in my dissertation.

The members of the Ultrasound Research Institute have contributed immensely to my personal and professional time in Kaunas. I am truly grateful to Chairman of Doctoral Studies Committee of science field Prof. Rymantas Jonas Kazys for his valuable suggestions and leadership. I would like to acknowledge honorary director of Ultrasound Research Institute of the Kaunas University of Technology (KTU), Prof. Liudas Mazeika for his immense guidance and support in the signal processing of ultrasonic signals. I would like to thank my colleague Vykintas Samaitis who helped beyond his limits in the experiments and simulations during the initial phase of my Ph.D.

I want to thank the head of the department of multimedia engineering, Armantas Ostreika and Professor Vascius Jusas for their cooperation, guidance and motivation during my work as a lecturer. I am also grateful to the administrator of Ultrasound Research Institute Gitana Svediene and administrator of Multimedia Engineering Ligita Zailskaite for their help and support in documentation and departmental works. My time at KTU was also enriched by the help and support provided by the KTU doctoral office, international office and HR office. I want to especially acknowledge Reda Zilenaite, Jolita Steponkeviciute, Vita Daudaraviciene, Simona Devenyte, Kristina Pudzinskaite and Audrone Rackauskiene. I am also grateful to former director of international office Neringa who helped me and my wife in all legal issues. I do not want to forget Vice-Rector for Research and Innovations, Leonas Balasevicius for his administrative and leadership efforts to create a positive research environment at University for the researchers and scientists.

I gratefully acknowledge the funding received towards my PhD study from the Research Council of Lithuania. I am also grateful to the funding received through the Lithuanian Academy of sciences Scholarship for academic achievement in 2017. I am thankful to KTU for providing me the scholarship for academic achievements in 2017. I greatly appreciate the support received through the Lithuanian academy of sciences and KTU to participate in various international conferences to present the research works. My thanks also go out to the scholarship I received from the INFOBALT ICT company, Vilnius in 2016. I am also grateful to the European Structural Integrity Society (ESIS) for providing the ESIS support for researchers in 2018.

My time in Kaunas was made enjoyable in large part due to the family friends Linas and Ieva that became a part of my life. I am also grateful for the time spent with friends Marius, Jaishree, Bengisu, Monika, Yatin, Neelesh and Paulius as I finished

up my degree, and for many other people and memories. My special thanks to my colleagues Vykintas, Olgirdas, Audrius and my friends Marius, Tautvydas, Martynas and Milda for their contribution in translating the summary of dissertation into Lithuanian. Lastly, I would like to thank my family for all their love and encouragement. For my mother Lalit and brothers Siddhartha and Sambhav who supported me in all my pursuits. And most of all for my loving, supportive, encouraging, and patient wife Sonam Chopra whose faithful support during the final stages of this Ph.D. is so appreciated. Thank you.

SL344. 2019-05-02 17, 75 leidyb. apsk. l. Tiražas 12 egz. Užsakymas 107.
Išleido Kauno technologijos universitetas, K. Donelaičio g. 73, 44249 Kaunas
Spausdino leidyklos „Technologija“ spaustuvė, Studentų g. 54, 51424 Kaunas